UNIVERSITY OF CALIFORNIA, SAN DIEGO

Seismic Structure of Shallow Lithosphere at Locations of Distinctive Seafloor Spreading

A dissertation submitted in partial satisfaction of the
requirements for the degree
Doctor of Philosophy

in

Earth Sciences

by

Ashlee Shae Henig

Committee in charge:

Professor Donna Blackman, Chair
Professor Anne Conn
Professor Alistair Harding
Professor Peter Lonsdale
Professor Peter Shearer
Professor David Stegman

2013

The dissertation of Ashlee Shae Henig is approved, and it is acceptable in quality and form for publication on microfilm and electronically:

_____

_____

_____

_____

_____

_____
Chair

University of California, San Diego

2013

DEDICATION

To the years 22-27.

EPIGRAPH

The Farther We Go
The More We Can See.
—Unknown

TABLE OF CONTENTS

LIST OF FIGURES

LIST OF TABLES

ACKNOWLEDGEMENTS

I thank first and foremost Donna Blackman, an inspirational woman and scientist - I could not have asked for a better adviser. There really aren't words to describe the gifts you've given me. Through both academic and personal struggles, you've supported me and helped me succeed. I appreciate that you always had an open door and made so much of your time available to me. You are an excellent co-author, mentor, and friend, and I will always look up to you. You have my sincerest thanks.

I'd like to follow with a very special thanks to my committee for your time and thoughtful comments and contributions to my research. Thank you Alistair, for your boundless patience, generous help, and for stepping in to fill the gap when Donna moved away. A sincere thanks to Anne, for making the trips from upper campus, and for your excellent questions that were always spot-on to the crux of my research. Dave, thank you for being both a helpful committee member and an even better friend. Peter L., I've enjoyed learning your alternate perspectives on my research and thank you for providing a check to my geological intuition. Peter S., thank you for being a wonderful teacher and committee member, and always being on my side. This body of work has really benefited from the insight of the committee and I am appreciative for your votes of confidence, which greatly improved my academic self-esteem.

Also deserving of my thanks are Graham Kent, Lisa Tauxe, and Helen Fricker for starting me out on my journey through graduate research. Peter Shearer, Gabi Laske, and Cheryl Peach provided me with excellent teaching experience during my quarters as TA for various classes, while the SIO department trusted me as Senior TA for four years. I am grateful to the National Science Foundation, which sponsored my research in the form of grants and fellowships, and more importantly to the authors of the grants and fellowships from which I benefitted. I thank Cheryl Peach and Hubert Staudigel for the wonderful opportunity to teach in a high school marine science classroom through the NSF GK12 Scripps Classroom Connection Program. I know this experience will continue to be valuable to me as I move forward with teaching and outreach throughout my

career. Thank you to the SIO Graduate Department, past and present, for your assistance with navigating graduate deadlines and paperwork.

Thank you to Janine Buehler and Xiaowei Chen for your generous help in the formatting of this thesis (and your generosity in general). Many thanks to Jillian Maloney for listening to more practice talks than I can count (I think you know my research as well as I do!). Also, thank you to Adrien Arnulf for sharing your wisdom and for helping with the advancement of the science at Atlantis Massif and the Lau Basin in the form of Full Waveform Inversions.

Last but certainly not least, a million thanks to the family and friends who supported me, laughed with me, pushed me, and believed in me. My most memorable moments are all with you.

To

Kim - for your love, support, and generosity, for pulling me through some of the toughest years of my life.

Mom - for being my number 1 fan and loving me more than the Sun, the Moon, and the Stars.

Dad and Julie - for your encouragement and the pride you always show in me.

Jillian - for encouraging me, pushing me, calming me, and sharing in all the milestones.

Janine and Xiaowei - for being two of the most generous classmates and friends, and some of the most inspirational women I know. I'm thankful that we will always have a special bond.

Valerie - for being a lifelong friend, the kind who will always make her way back into your life.

Leah - for showing me unconditional and unyielding friendship - even from far away.

Rachel - for challenging me and pushing me to do things I didn't think were possible.

Erica - for being so dang fun to be around.

Soli - for your friendship and for being a voice of reason during the final

years.

Robert - for your wisdom and your ability to keep me laughing in any circumstance.

Nicole - for more fun times and laughs than I can count.

Patty - for coming back into my life at just the right time, and being there through the thick of it.

The Stegmans - for your friendship, time spent with your cute baby, and relaxing evenings in your cedar-plank hot tub.

To my six geophysics classmates, thanks for a fun year in the Keller and many more after that. And to my Barnyard officemates: it was so fun getting to know you and commiserating together about the woes of the Barnyard.

I can't possibly list all of the people who have touched me during my time at Scripps, but please know that each one of you with whom I interacted has a special place in my heart, and I have many great memories of you all.

With love and awe,

Ashlee

Chapter 2, in full, is a reprint of the material as it appears in Henig, A. S., D. K. Blackman, A. J. Harding, J.-P. Canales, and G. M. Kent (2012), Downward continued multichannel seismic refraction analysis of Atlantis Massif oceanic core complex, 30°N, Mid-Atlantic Ridge, *Geochemistry Geophysics Geosystems, 13*, Q0AG07, doi:10.1029/2012GC004059. The dissertation author was the primary investigator and author of this paper.

Chapter 4, in part, is currently being prepared for submission of the material. Henig, A. S., A. J. Harding. The dissertation author was the primary investigator and author of this paper.

VITA

2007	B. A. in Physics *magna cum laude*, University of California, Santa Barbara
2010	M. S. in Earth Sciences, Scripps Institution of Oceanography, University of California, San Diego
2013	Ph. D. in Earth Sciences, Scripps Institution of Oceanography, University of California, San Diego

PUBLICATIONS

Henig, A. S., D. K. Blackman, A. J. Harding, J.-P. Canales, and G. M. Kent (2012), Downward continued multichannel seismic refraction analysis of Atlantis Massif oceanic core complex, 30°N, Mid-Atlantic Ridge, *Geochemistry Geophysics Geosystems, 13*, Q0AG07, doi:10.1029/2012GC004059.

ABSTRACT OF THE DISSERTATION

Seismic Structure of Shallow Lithosphere at Locations of Distinctive Seafloor Spreading

by

Ashlee Shae Henig

Doctor of Philosophy in Earth Sciences

University of California, San Diego, 2013

Professor Donna Blackman, Chair

Multichannel Seismic (MCS) Refraction and Reflection analyses are used to determine the structure of the upper 1-2 km of lithosphere at two distinct seafloor spreading regions at 1) the Atlantis Massif Oceanic Core Complex (OCC) at 30N on the Mid-Atlantic Ridge (MAR), and 2) the southward propagating tip and pseudofault regions of the Central Lau Spreading Center (CLSC) in the Lau Backarc Basin. The Synthetic Ocean Bottom Experiment (SOBE) downward continuation technique is employed to increase the number of usable near-offset first arrival picks within the data allowing the creation of a continuous 2-D upper crustal tomographic model while also improving resolution in the shallow crust. Seismic velocity structure from the resultant tomography models is analyzed in

context of the local surroundings and additional available data, and interpreted for formation history and accretionary mechanism of the lithosphere. Summaries of findings at the two study locations are as follows.

Atlantis Massif Oceanic Core Complex

At Atlantis Massif, axis-parallel and perpendicular seismic tomography models indicate that lithospheric structure deviates significantly from the typical oceanic layer cake model. Surface velocities change as much as 3 km/s over several hundred meters lateral distance and local vertical velocity gradients are as high as 6 s^{-1}. Velocities as high as 5 km/s, characteristic of gabbro and confirmed by a 1.4 km drill hole, outcrop directly at the seafloor on the Central Dome and the eastern Southern Ridge and compose the main internal structure of the core complex. These high velocities are surrounded by sheaths of lower velocity structure interpreted as sepentinized peridotite. This gabbroic core with surrounding altered mantle rock implies a history of detachment faulting and the exhumation of originally deep-seated crustal rock. The geometry of Atlantis Massif and the location and orientation of the gabbroic core are consistent with a southeast dipping detachment fault that nucleated at the boundary of a pluton(s) injected into the predominantly ultramafic lithosphere by a southward propagating magmatic source.

Central Lau Spreading Center Propagating Tip

New along-axis tomographic models show a dramatic change in the thickness of layer 2 as the tip of the CLSC propagator is approached. Based on shot gather analysis and tomography, crustal layer 2A ($<$ 3 km/s) maintains a relatively constant thickness of $\sim$150-250 m along the $\sim$140 km of the CLSC immediately north of the propagating rift. Layer 2A transitions to a thickness of 500-600 m (including uppermost velocities $<$ 2 km/s) starting about 15 km north of the bathymetrically defined ridge tip. Likewise, as the propagating tip is approached, the layer 2A/2B transition zone changes, in conjunction with the change in layer 2A, from a sharp to low velocity gradient. These structural changes are correlated with results that show both the AMC reflector and the layer 2A reflector disappearing about 18 and 11 km, respectively, from the bathymetric signature of the propa-

gating tip. These observations reflect a change in accretionary mechanism toward the propagating tip, one interpretation being the transition from narrow, focused dike injection to diffuse, random diking with an intermixing of the extrusive and dike layers. Across-axis profiles also support these findings, but do not exhibit the expected aging properties or a structural signature associated with the pseudofault regions.

Chapter 1

Introduction

The most widely popularized version of seafloor structure is that defined by participants of the Penrose conference (Penrose, 1972) on ophiolites and oceanic crustal structure. Based on studies of ophiolites, this model takes the form of a basic layer-cake structure with three main components: the upper extrusive basalt layer, the middle sheeted dikes layer, and the basal gabbroic layer. These layers are represented as horizontal layers, one stacked vertically above the next.

Studies over the past forty years have supplied overwhelming evidence that the oceanic crustal structure is actually very complex and diverse when compared to this original Penrose model. While studies agree on the general rock and seismic velocity structure of the seafloor, there are no two areas of seafloor found to be identical. Comparisons can be made between oceanic crust at different locations, but care must be taken to compare on a general basis without expectation of a single ubiquitous structure.

Extensive research shows a fundamental difference between crust formed at slow (10-50 km/Myr) and fast (90+ km/Myr) spreading centers. Differences based on spreading rate extend to most properties of the spreading systems including ridge/rise morphology, crustal thicknesses and lithology, faulting regimes, and magma chamber volume and duration. Subsequently, each of these will be briefly considered in turn. Even more subtle, however, is the variability of properties observed among spreading centers of similar rates, which will be the main topic of this introduction.

The chapters contained within this thesis explore the heterogeneity of crustal structure, caused by interplay of the above factors. The study locations are in regions of distinct forms of seafloor spreading, at the inside corner of a ridge-transform-fault-intersection and at a propagating spreading center, further contributing to deviations in structure from the original layer-cake model. At each location, the results from seismic tomography are presented and a suggestion is made for a mechanism and/or history for crustal formation. Thus, I present a review of possible crustal architectures and features along with a brief discussion of some of the factors leading to crustal heterogeneity. The following sections serve as a reminder that care must be taken when assuming or teaching an overly-simplified model of the oceanic crust.

1.1 Rate Dependency of Spreading System Properties

The most notable directly observable difference between spreading centers formed at fast and slow rates is the morphology of the ridge or rise itself. Fast spreaders are characterized by an inflated axial high that is approximately 1-2 km wide and contains low relief fault scarps on the order of 10s of meters (Lonsdale, 1977; Macdonald *et al.*, 1988). Slow spreaders on the other hand, consist of a wide axial rift valley 35-40 km wide and 1-2 km deep. The median valley, bounded by a series of individual fault scarps up to 100s of meters high, is typically between 5-12 km wide (Macdonald, 1986).

As the expression of extensional plate boundaries, spreading centers and their flanks display abundant normal faulting. The most common feature on the Earths surface are normal-fault-bounded crustal blocks called abyssal hills that back-tilt and rotate as they form the flanks of the spreading centers (Macdonald, 2001). These high-angle, inward-dipping (toward the axis) normal faults are prevalent at all spreading rates. At slow spreading ridges, these faults cause the formation of the steep axial valley walls and typically cut across the axial volcanoes to incorporate those features into the flank walls (Smith and Cann, 1993). Recently,

however, another type of normal fault, the long-lived (and sometimes low-angle) detachment fault, has proven to be quite ubiquitous (Smith *et al.*, 2006, 2008), mostly at slow spreading rates. Simply as a result of the geometry and duration of faults at the axis, which can differ based on spreading rate, crustal and axial structure can vary greatly.

At fast spreading centers, it is common that a nearly continuous axial magma chamber exists beneath the rise and isolated sills may extend somewhat off axis (Detrick *et al.*, 1987; Sinton and Detrick, 1992). This provides a robust reservoir of magma from which new crustal material accretes to the seafloor, forming a relatively homogenous structure. In contrast, at slow spreading systems, it is more common that discrete magma bodies form episodically beneath the ridge crest (Nisbet and Fowler, 1978). Thus, crustal construction at slow spreading centers, without the continuous supply of magma, is dominated by tectonic extension and is comparatively heterogeneous. One similarity of magmatic properties at all spreading rates, however, is the along axis variation of magma supply. It is a widespread phenomenon that melt supply is most robust at segment centers and wanes toward the segment ends (Purdy and Detrick, 1986; Solomon and Toomey, 1992). This factor leads to analogous traits on segment scales between fast and slower spreading centers.

Since faulting and the presence of magma are different at slow and fast spreading centers, it is expected that the crustal structure would be different as well. At faster rates with continuous linear axial volcanic ridges, more robust magmatism provides the material necessary to feed a coherent sheeted dike complex, and the extrusive layer above, in turn. With this configuration, the sides of a crystal mush zone slowly solidify to create a thick intrusive layer component of the oceanic crust. At slow spreading rates, magmatism is fundamentally different, feeding more discrete volcanic edifices in the axial valley. This leads to a crustal composition consisting of intermixed feeder tubes (in place of a sheeted dike complex) and extrusives, underlain by small plutons that form from the crystallization of discrete, transient magma bodies at the base of the crust.

1.2 Obvious Differences in Structure at Slow Spreading Systems

Slow spreading systems exhibit the widest array of crustal structures. Formed from ephemerally magmatic or amagmatic conditions, it is difficult to predict just what the constituents of the crust will be. Components of slow-spread crust can run the gamut from extrusive lavas and dikes (Hooft *et al.*, 2000) to less-abundant volcanic feeder tubes (Smith and Cann, 1993), from bodies of crystal mush to small dike- or sill-like plutons, and may contain small or large amounts of altered or unaltered mantle rock (e.g. Cannat, 1993).

Cannat *et al.* (2006) recognize three distinct topographic classifications at the very slow spreading Southwest Indian Ridge (SWIR): volcanic seafloor, corrugated seafloor, and smooth seafloor. These variations in topography and corresponding residual mantle Bouguer anomalies (RMBAs) suggest different internal structures for each type. This is further supported by dredges of the latter two types of seafloor, which returned serpentinized mantle rock with or without the inclusion of gabbros and basalts at the smooth seafloor (Seyler *et al.*, 2003), and fault rocks in the case of the corrugated surfaces (Escartín *et al.*, 2003). The three crustal forms are likely associated with different levels and depths of magmatism and modes of faulting, some of which can introduce mantle rocks as a main component of the structure (Cannat, 1993). If mantle rocks are exhumed to crustal levels, plutons of gabbro may then be injected into this exhumed mantle rock to form a plum-pudding-style architecture (Cannat, 1996; Escartín *et al.*, 2003).

The volcanic and corrugated seafloor structures also develop at the slightly faster, but still slow-spreading, Mid-Atlantic Ridge (MAR) (e.g. Cann *et al.*, 1997). Unlike at the SWIR, detachment faults forming corrugated seafloor characteristic of oceanic core complexes (Chapter 2, this thesis) are now known to be a prominent faulting mechanism at the MAR (Cann *et al.*, 1997; Smith *et al.*, 2006, 2008). Various studies have shown that these detachment faults create a crustal structure where gabbros and serpentinized peridotites are exhumed directly at the seafloor and upper crustal layers are not present (Blackman *et al.*, 2006; Canales *et al.*,

2008; Xu *et al.*, 2009; Henig *et al.*, 2012). Other studies show that the extrusives and sheeted dikes do exist in some locations (Arnulf *et al.*, 2011; Hooft *et al.*, 2000), thus allowing for the possibility of Penrose-like crust to also exist at slow spreading centers. It is clear that there are many factors affecting the architecture of crust at slow spreading ridges, and that slow-spread oceanic crust can take on very diverse forms.

1.3 Subtle Differences in Structure at Fast Spreading Systems

Crust formed at Fast spreading centers, while still exemplifying moderate differences, is overall much more homogeneous than its slow-spread counterpart. Overall, the layered crustal structure holds true, but changes in thickness, seismic velocity, definition of layer contacts, and dips of layers all add variation to the crust. Differences are based upon aging, magma supply and chamber depth, fracturing, chemical alteration, and location along a spreading segment. Although the following characteristics are discussed in context of fast spreaders, they are not necessarily limited to fast-spread crust and may also contribute to variability in slow spreading areas.

Upper and lower basaltic lavas, defined based on amount of pore space within the rock, each vary as much as 600 m in thickness between the study areas examined by Karson *et al.* (2002). Although these areas are no longer at active spreading centers, the upper crustal thicknesses probably were controlled by the depth of the magma chamber at the rise where they formed (Buck *et al.*, 1997). Variations determined by seismic studies are more modest than this (Detrick *et al.*, 1993; Harding *et al.*, 1993; Hooft *et al.*, 1996). The upper crustal layer 2A can increase 2-3 times in thickness, while seismic velocities increase rapidly, within 1-2 km from the ridge (Detrick *et al.*, 1993; Harding *et al.*, 1993) or by ages $<$ 5 Ma (Carlson, 2004). The changes in thickness are due to off-axis building of the volcanic crust and lava flows that overflow the boundaries of the axis, while the increase in seismic velocities are probably due to the infilling of fractures and

pore space by precipitation from hydrothermal circulation (Harding *et al.*, 1989; Vera *et al.*, 1990). Therefore, on- and off-axis crust originally formed in the same location at faster spreading centers will have a variety of crustal forms.

Crustal structure at fast spreading centers is also found to vary along segment strike, particularly with regard to, proximity to fracture zones, overlapping spreading centers (OSCs), and other non-transform offsets (NTOs) (Macdonald *et al.*, 1988). Both crustal velocities and thicknesses are affected by these spreading ridge features (Canales *et al.*, 2003). Segment centers tend to have higher upper crustal velocities, possibly due to increased and higher-reaching diking, while fracture zones comparatively have lower velocities, probably due to fracturing (Canales *et al.*, 2003). Crust associated with OSCs tends to be thicker due to pooling of extrusives within the basin, and tends to have lower velocities due to fracturing during OSC propagation (Bazin *et al.*, 1998, 2001; Canales *et al.*, 2003). At 9°N on the East Pacific Rise, crustal thicknesses vary as much as 2.5 km along the segment (Barth and Mutter, 1996), proving that crust constructed at fast spreading centers is not necessarily of uniform thickness. While the characteristics of fast-spread crust are more homogenous than crust formed at slow spreading centers, they still have subtle variations that should be considered when discussing crustal structure.

1.4 A Note on Intermediate Spreading

Intermediate spreading centers, as the name suggests, have features that are intermediate between fast and slow spreading systems. Topography of the axis can take a variety of forms (e.g. Canales *et al.*, 2003), but a common expression is a rise like that of fast spreading centers with a cyclical axial summit graben more characteristic of slow spreaders (Small, 1994). Studies suggest that the off-axis thickening of seismic layer 2A is controlled by the morphology of the intermediate rate ridge (Blacic *et al.*, 2004), the slope of which either promotes or impedes off-axis flows. The cyclical axial summit graben implies an episodicity to the robustness and/or depth of the underlying magma chamber, which in turn may control the crustal thickness (Buck *et al.*, 1997) produced at intermediate spreading

areas. These spreading systems are just as likely to produce crust with variations in thickness, seismic velocity, fracturing, and composition as either the slow or fast end-members.

1.5 Emphasis of this Dissertation within the Broader Theme

This thesis examines upper crustal seismic structure at locations of distinct seafloor spreading mechanisms and at areas of different spreading rates. The studies add detail to our understanding of how the seafloor is hugely diverse in structure and suggests that the structural variation is largely controlled by varied accretionary mechanisms active at the global seafloor spreading system. Accretionary mechanism is controlled, at least in part, by the local magma budget of a spreading center and is thus discussed within in this context. From these studies, I hope the reader will come to understand that, in terms of oceanic crustal structure, variations and complex interplay between faulting and magmatism are the norm.

References

Arnulf, A., Singh, S., Harding, A., Kent, G., and Crawford, W., 2011: Strong seismic heterogeneity in layer 2a near hydrothermal vents at the mid-atlantic ridge. *Geophysical Research Letters*, **38**(13), L13320. doi:10.1029/2011GL047753.

Barth, G., and Mutter, J., 1996: Variability in oceanic crustal thickness and structure: Multichannel seismic reflection results from the northern east pacific rise. *Journal of geophysical research*, **101**(B8), 17951–17.

Bazin, S., Harding, A., Kent, G., Orcutt, J., Tong, C., Pye, J., Singh, S., Barton, P., Sinha, M., White, R., *et al.*, 2001: Three-dimensional shallow crustal emplacement at the 9 03? n overlapping spreading center on the east pacific rise: Correlations between magnetization and tomographic images. *Journal of geophysical research*, **106**(B8), 16–101.

Bazin, S., Van Avendonk, H., Harding, A., Orcutt, J., Canales, J., Detrick, R., Group, M., *et al.*, 1998: Crustal structure of the flanks of the east pacific rise: Implications for overlapping spreading centers. *Geophysical research letters*, **25**(12), 2213–2216.

Blacic, T., Ito, G., Canales, J., Detrick, R., and Sinton, J., 2004: Constructing the crust along the galapagos spreading center 91.3–95.5 w: Correlation of seismic layer 2a with axial magma lens and topographic characteristics.

Blackman, D., Ildefonse, B., John, B., Ohara, Y., Miller, D., and MacLeod, C., 2006: Expedition 304/305 scientists. In *Proceedings of the Integrated Ocean Drilling Program*, volume 304/305. doi:10.2204/iodp.sp.304305.2005.

Buck, W., Carbotte, S., and Mutter, C., 1997: Controls on extrusion at mid-ocean ridges. *Geology*, **25**(10), 935–938. doi:10.1130/?0091-7613(1997)?025¡0935:COEAMO¿?2.3.CO;2.

Canales, J., Tucholke, B., Xu, M., Collins, J., and DuBois, D., 2008: Seismic evidence for large-scale compositional heterogeneity of oceanic core complexes. *Geochemistry Geophysics Geosystems*, **9**(8), Q08002. doi:10.1029/2008GC002009.

Canales, J. P., Detrick, R., Toomey, D., and Wilcock, W., 2003: Segment-scale variations in the crustal structure of 150–300 kyr old fast spreading oceanic crust (east pacific rise, 8 15? n–10 5? n) from wide-angle seismic refraction profiles. *Geophysical Journal International*, **152**(3), 766–794.

Cann, J., Blackman, D., Smith, D., McAllister, E., Janssen, B., Mello, S., Avgerinos, E., Pascoe, A., and Escartin, J., 1997: Corrugated slip surfaces formed at ridge-transform intersections on the mid-atlantic ridge. *Nature*, **385**(6614), 329–332. doi:10.1038/385329a0.

Cannat, M., 1993: Emplacement of mantle rocks in the seafloor at mid-ocean ridges. *Journal of Geophysical Research*, **98**(B3), 4163–4172. doi: 10.1029/92JB02221.

Cannat, M., 1996: How thick is the magmatic crust at slow spreading oceanic ridges? *Journal of Geophysical Research*, **101**(B2), 2847–2857.

Cannat, M., Sauter, D., Mendel, V., Ruellan, E., Okino, K., Escartin, J., Combier, V., and Baala, M., 2006: Modes of seafloor generation at a melt-poor ultraslow-spreading ridge. *Geology*, **34**(7), 605–608. doi:10.1130/G22486.1.

Carlson, R., 2004: Seismic properties of layer 2a at 11 ma: Results of a vertical seismic profile at ocean drilling program site 1243. *Geophysical research letters*, **31**(17), L17601. doi:10.1029/2004GL020598.

Detrick, R., Buhl, P., Vera, E., Mutter, J., Orcutt, J., Madsen, J., and Brocher, T., 1987: Multi-channel seismic imaging of a crustal magma chamber along the east pacific rise. *Nature*, **326**(6108), 35–41.

Detrick, R., Harding, A., Kent, G., Orcutt, J., Mutter, J., and Buhl, P., 1993: Seismic structure of the southern east pacific rise. *Science*, **259**, 499–503. doi: 10.1126/science.259.5094.499.

Escartín, J., Mével, C., MacLeod, C., and McCaig, A., 2003: Constraints on deformation conditions and the origin of oceanic detachments: The mid-atlantic ridge core complex at 15 450n. *Geochem. Geophys. Geosyst*, **4**(8), 1067. doi: 10.1029/2002GC000472.

Harding, A., Kent, G., and Orcutt, J., 1993: A multichannel seismic investigation of upper crustal structure at 9 n on the east pacific rise: Implications for crustal accretion. *Journal of geophysical research*, **98**(B8), 13925–13944. doi: 10.1029/93JB00886.

Harding, A., Orcutt, J., Kappus, M., Vera, E., Mutter, J., Buhl, P., Detrick, R., and Brocher, T., 1989: Structure of young oceanic crust at 13 n on the east pacific rise from expanding spread profiles. *Journal of Geophysical Research*, **94**(B9), 12163–12.

Henig, A., Blackman, D., Harding, A., Canales, J., and Kent, G., 2012: Downward continued multichannel seismic refraction analysis of atlantis massif oceanic core complex, 30 n, mid-atlantic ridge. *Geochemistry Geophysics Geosystems*, **13**(null), Q0AG07. doi:10.1029/2012GC004059.

Hooft, E., Detrick, R., Toomey, D., Collins, J., and Lin, J., 2000: Crustal thickness and structure along three contrasting spreading segments of the mid-atlantic ridge, 33.5–35 n. *Journal of geophysical research*, **105**(B4), 8205–8226. doi: 10.1029/95JB02502.

Hooft, E., Schouten, H., and Detrick, R., 1996: Constraining crustal emplacement processes from the variation in seismic layer 2a thickness at the east pacific rise. *Earth and planetary science letters*, **142**(3), 289–309.

Karson, J., Klein, E., Hurst, S., Lee, C., Rivizzigno, P., Curewitz, D., Morris, A., Miller, D., Varga, R., Christeson, G., *et al.*, 2002: Structure of uppermost fast-spread oceanic crust exposed at the hess deep rift: Implications for subaxial processes at the east pacific rise. *Geochemistry Geophysics Geosystems*, **3**(1), 1002. doi:10.1029/2001GC000155.

Lonsdale, P., 1977: Structural geomorphology of a fast-spreading rise crest: the east pacific rise near 3 25? s. *Marine Geophysical Research*, **3**(3), 251–293.

Macdonald, K., 1986: The crest of the mid-atlantic ridge: Models for crustal generation processes and tectonics. *The Geology of North America*, **1000**, 51–68.

Macdonald, K., Fox, P., Perram, L., Eisen, M., Haymon, R., Miller, S., Carbotte, S., Cormier, M., and Shor, A., 1988: A new view of the mid-ocean ridge from the behaviour of ridge-axis discontinuities. *Nature*, **335**(6187), 217–225.

Macdonald, K. C., 2001: Mid-ocean ridge tectonics, volcanism and geomorphology. *Geology*, **26**(455), 458.

Nisbet, E., and Fowler, C., 1978: The mid-atlantic ridge at 37 and 45 n: some geophysical and petrological constraints. *Geophysical Journal of the Royal Astronomical Society*, **54**(3), 631–660.

Penrose, C., 1972: Penrose field conference on ophiolites. *Geotimes*, **17**, 24–25.

Purdy, G., and Detrick, R., 1986: Crustal structure of the mid-atlantic ridge at 23 n from seismic refraction studies. *Journal of Geophysical Research*, **91**(B3), 3739–3762. doi:10.1029/JB091iB03p03739.

Seyler, M., Cannat, M., and Mével, C., 2003: Evidence for major-element heterogeneity in the mantle source of abyssal peridotites from the southwest indian ridge (52 to 68 e). *Geochemistry Geophysics Geosystems*, **4**(2), 9101. doi:10.1029/2002GC000305.

Sinton, J., and Detrick, R., 1992: Mid-ocean ridge magma chambers. *Journal of Geophysical Research*, **97**(B1), 197–216. doi:10.1029/91JB02508.

Small, C., 1994: A global analysis of mid-ocean ridge axial topography. *Geophysical Journal International*, **116**(1), 64–84.

Smith, D., and Cann, J., 1993: Building the crust at the mid-atlantic ridge. *Nature*, **365**(6448), 707–715. doi:10.1038/365707a0.

Smith, D., Cann, J., and Escartín, J., 2006: Widespread active detachment faulting and core complex formation near 13°n on the mid-atlantic ridge. *Nature Letters*, **442**, 440–443. doi:10.1038/nature04950.

Smith, D., Escartín, J., Schouten, H., and Cann, J., 2008: Fault rotation and core complex formation: Significant processes in seafloor formation at slow-spreading mid-ocean ridges (mid-atlantic ridge, 13-15°n). *Geochemistry, Geophysics, Geosystems*, **9**(3), Q03003. doi:10.1029/2007GC001699.

Solomon, S., and Toomey, D., 1992: The structure of mid-ocean ridges. *Annual Review of Earth and Planetary Sciences*, **20**, 329–364.

Vera, E., Mutter, J., Buhl, P., Orcutt, J., Harding, A., Kappus, M., Detrick, R., and Brocher, T., 1990: The structure of 0-to 0.2-my-old oceanic crust at 9 n on the east pacific rise from expanded spread profiles. *Journal of Geophysical Research*, **95**(B10), 15529–15. doi:10.1029/JB095iB10p15529.

Xu, M., Canales, J., Tucholke, B., and DuBois, D., 2009: Heterogeneous seismic velocity structure of the upper lithosphere at kane oceanic core complex, mid-atlantic ridge. *Geochemistry, Geophysics, Geosystems*, **10**(10), Q10001. doi: 10.1029/2009GC002586.

Chapter 2

Downward Continued Multi-Channel Seismic Refraction Analysis of Atlantis Massif Oceanic Core Complex, 30°N Mid-Atlantic Ridge

Detailed seismic refraction results show striking lateral and vertical variability of velocity structure within the Atlantis Massif oceanic core complex (OCC), contrasting notably with its conjugate ridge flank. Multi-channel seismic (MCS) data are downward continued using the Synthetic On Bottom Experiment (SOBE) method, providing unprecedented detail in tomographic models of the P-wave velocity structure to subseafloor depths of up to 1.5 km. Velocities can vary up to 3 km/s over several hundred meters and unusually high velocities (∼5 km/s) are found immediately beneath the seafloor in key regions. Correlation with *in situ* and dredged rock samples, video and records from submersible dives, and a 1.415 km drill core, allow us to infer dominant lithologies. A high velocity body(ies) found to shoal near to the seafloor in multiple locations is interpreted as gabbro and is displaced along isochrons within the OCC, indicating a propagating magmatic source

as the origin for this pluton(s). The western two-thirds of the Southern Ridge is capped in serpentinite that may extend nearly to the base of our ray coverage. The distribution of inferred serpentinite indicates that the gabbroic pluton(s) was emplaced into a dominantly peridotitic host rock. Presumably the mantle host rock was later altered via seawater penetration along the detachment zone, which controlled development of the OCC. The asymmetric distribution of seismic velocities and morphology of Atlantis Massif are consistent with a detachment fault with a component of dip to the southeast. The lowest velocities observed atop the eastern Central Dome and conjugate crust are most likely volcanics. Here, an updated model of the magmatic and extensional faulting processes at Atlantis Massif is deduced from the seismic results, contributing more generally to understanding the processes controlling the formation of heterogeneous lithosphere at slow-rate spreading centers.

2.1 Introduction

Lithospheric heterogeneity is the result of ridge processes that vary in time and space, and to first order, structural differences in slow-spread lithosphere produce anomalous seafloor morphology (e.g. *Cannat et al.*, 2006) interrupting the more common abyssal hill pattern. Early studies of gravity structure at the Mid-Atlantic Ridge (MAR) suggest crustal thickness variations of several kilometers along the ridge axis over length scales of several hundred kilometers (*Kuo and Forsyth*, 1988; *Lin et al.*, 1990; *Morris and Detrick*, 1991; *Michael et al.*, 1994; *Detrick et al.*, 1995) and across transform faults, while across-axis, smaller-scale gravity studies suggest crustal thickness differences can also occur on conjugate sides of the ridge (*Blackman et al.*, 1998, 2008).

Regional seismic investigations also indicate a heterogeneous slow-spread lithospheric structure at the segment scale. Seismic imaging of the crust along the axis of various spreading segments shows several kilometers of thinning between segment center and segment end that is dominantly controlled by thickness variations in the lower crustal layer (e.g. *Tolstoy et al.*, 1993; *Hooft et al.*, 2000;

Planert et al., 2009). These crustal thickness variations are often accompanied by lateral changes in seismic velocity (e.g. *Canales et al.*, 2000a; *Hooft et al.*, 2000). Seismically determined changes in thickness and structure of igneous crust are also documented across axis (*Canales et al.*, 2000b). Denser local seismic studies show dramatic changes in seismic structure at lateral scales of a few kilometers (*Canales et al.*, 2008; *Xu et al.*, 2009; *Arnulf et al.*, 2011).

Geologic studies also show that the classic homogeneous layered model of oceanic crust (*Penrose*, 1973), where erupted basalts overlie sheeted dikes and gabbro at depth, is only one of many crustal structures possible. Outcrops of serpentinized peridotite and gabbro (*Cannat*, 1993; *Dick et al.*, 2008), in contrast to the expected erupted basalt, have been identified at the seafloor on ridge flanks of slow spreading centers by submersible (*Karson*, 1999; *Blackman et al.*, 2002; *Boschi et al.*, 2006; *Tucholke and Lin*, 1994) and drilling studies (*Dick et al.*, 2000; *MacLeod et al.*, 2002; *Kelemen et al.*, 2004; *Blackman et al.*, 2006). All of these observations illustrate the spatially- and temporally-irregular magmatic processes and faulting styles that typify slow-spreading ridges and control the formation of heterogeneous crust and lithosphere.

Oceanic core complexes (OCCs), lower crustal and mantle sections exhumed by detachment faulting, are formed at slow and intermediate spreading centers (*Cann et al.*, 1997; *Tucholke et al.*, 1998, 2001; *Ohara et al.*, 2001; *Reston et al.*, 2002; *Searle et al.*, 2003; *Smith et al.*, 2006, 2008), probably in association with long lived detachment faulting that persists for up to over 1 Myr (*Tucholke et al.*, 1998; *Grimes et al.*, 2008). The OCCs are domal and characterized by their high relief, often kilometers above surrounding seafloor, and by the presence of spreading-parallel corrugations on the capping surface that have 10s m amplitude and km-scale wavelengths (*Cann et al.*, 1997; *Tucholke et al.*, 1998). The corrugations document sustained relative motion between the exposed footwall and previously overlying hanging wall. Recent studies show that detachment faulting is a prominent process along portions of all slow spreading oceanic ridges (*Cannat et al.*, 2006; *Smith et al.*, 2006; *Escartín et al.*, 2008) and is likely controlled by temporally changing magmatic conditions (*Ildefonse et al.*, 2007; *Tucholke et al.*,

2008; *MacLeod et al.*, 2009; *Olive et al.*, 2010). Numerical models estimate that during lithospheric creation, the formation of detachment faults near the ridge occurs when magmatic accretion is active between 30-50% of the time, while the remainder of plate separation is due to tectonic extension (*Buck et al.*, 2005; *Tucholke et al.*, 2008; *Olive et al.*, 2010). At these rates of magmatism, plutons can be emplaced in the ultramafic host-rock forming a plum-pudding style lithosphere (*Cannat*, 1993; *Escartín et al.*, 2003; *Ildefonse et al.*, 2007) and can be denuded to the seafloor due to motion on one of these detachment faults. Determination of the internal structure of OCCs can provide insight into the magmatic conditions during their formation and perhaps constrain the extent of alteration.

In this paper, we present a detailed seismic refraction study of the Atlantis Massif OCC (Figure 1), a young and well-mapped OCC on the Mid-Atlantic Ridge, and its conjugate crust, with the main objective of characterizing structural variability and magmatic history in this location. Three OCCs occur along the Atlantis transform fault (ATF) within lithosphere formed in the last 10 Myr (*Cann et al.*, 1997), suggesting continued episodicity in magma supply. Seismic imaging of the OCC allows us to constrain vertical and lateral variations in seismic velocity and we can employ these velocity structure observations in a lithologic and evolutionary analysis of Atlantis Massif.

Our study expands on the multi-channel seismic (MCS) refraction study of *Canales et al.* (2008), where only two MCS lines were analyzed with sea surface data, to include the full dataset covering the massif. We use an innovative downward continuation technique (*Harding et al.*, 2007; *Arnulf et al.*, 2011) to process the seismic data. The downward continuation technique has not previously been applied to a study of an OCC, therefore this study provides insights into how this method performs in high relief areas with high subsurface velocities and velocity gradients (*Canales et al.*, 2008).

We present tomographic models for 5 seismic lines covering the dome of the massif, which show heterogeneity of seismic structure and a decent correlation with in situ rock samples from seafloor outcrops. In addition, the model for one seismic line along the conjugate crust at the other side of the MAR axis serves to highlight

the anomalous character of the OCC. Based on our tomographic results, we develop a model for how faulting and magmatism evolved to produce the observed structure at Atlantis Massif.

2.2 Methods

2.2.1 Data Acquisition

Five intersecting MCS lines covering the dome of the Atlantis Massif and one line on the conjugate crust across the spreading axis from the OCC were collected aboard the R/V Maurice Ewing during the cruise EW-0102 in 2001 (*Canales et al.*, 2004). The seismic lines range in length from ∼21 to ∼27 km and comprise between 85 and 109 shots each in this study. Water depth varies greatly, from 785 m to nearly 3.25 km on the OCC, and the conjugate crust line is over seafloor depths of 2.5-3.15 km. The greatest relief on a single line is 1.67 km.

The survey source consisted of a 10-airgun array with total capacity of 3100 in^3 (51 l) towed at 8 m depth and fired approximately every 37.7 m. Receivers spaced 12.5 m along a 6 km long, 480-channel streamer recorded the returning energy at a depth of approximately 10 m. *In situ* source and receiver positions were determined from shipboard GPS, tail-buoy GPS recordings and compass-enhanced DigiCourse birds attached to the streamer (*Canales et al.*, 2008).

Seismic velocity models from lines A4 and A10 were previously published by *Canales et al.* (2008) using standard processing techniques. This study extends analysis to all six seismic lines surveying the OCC and the conjugate crust, including the previously studied lines A4 and A10, and makes use of a downward continuation processing method. Of the five OCC lines, two are parallel to the spreading direction (A9 and A10) and three are subparallel to the strike of the spreading axis (A4, A6, and A5), while the conjugate crust line A8 is subparallel to the MAR axis (Figure 1).

2.2.2 SOBE Downward Continuation and Additional Data Processing

We employ a method in which shots and receivers are downward continued to the seafloor using a Kirchhoff phase shift redatuming algorithm (*Shtivelman and Canning*, 1988). This process creates a Synthetic On-Bottom Experiment (SOBE) (*Harding et al.*, 2007; *Arnulf et al.*, 2011) that exposes the shallowest turning basement refractions as first arrivals by collapsing the water wave (the first seafloor reflection arrival) towards a point at zero-offset, and mostly unwrapping triplications produced by high gradient zones (Figure 2).

The SOBE technique is most useful in areas of large water depth and low subsurface velocities. In such survey conditions, the majority of the streamer channels record the seafloor reflection arriving ahead of the crustal refraction arrival, making it difficult to obtain useful travel-time picks for rays traveling through the shallow crust. In shallow water, or where the ratio of basement to water velocities is high, only the nearest offset streamer channels will record the reflection ahead of the refraction. In this case travel times of crustal refractions can be picked directly without use of downward continuation. In water depths of $\sim$3 km however, refracted data from at least the first 2 km of receivers are preceded by reflections.

This redatuming allows shallow, refracted energy that would generally be obscured by the seafloor reflection in deep water depths to be emergent (i.e., first arrivals), corresponding to raypaths in the upper few hundred meters of the subseafloor section. Travel-time picks of these near-offset crustal refractions thus provide excellent structural detail in the upper portion of our models. By improving the velocity detail in the upper region of the models, we also obtain better resolution of the deeper (400-1500 m) structure. Streamer tomography exploits the dense and even spatial distribution of MCS data, and is further improved upon by SOBE, which allows for the inclusion of shallower refractions that were only previously obtainable using either seafloor receivers and/or sources.

The first refracted arrival is clearly observed in SOBE shot gathers for most of this data set and the signal-to-noise ratio (SNR) is generally high. Besides downward continuation or redatuming, minimal processing of the data was

required. Prior to downward continuation, trace balancing was applied and consistently noisy traces were replaced by interpolation from the adjacent traces as continuity of seismic data across all streamer channels is required for downward continuation. The data were then downward continued in shot gather space, with a 5-20 Hz bandpass filter to exclude noise and unusable frequencies in the refraction data, followed by downward continuation in common receiver location space with a 20 Hz lowpass filter to minimize spatial aliasing. A fourth-order Butterworth filter was used in both steps and a water velocity of 1.5 km/s was assumed for the downward continuation.

2.2.3 Picking of Travel-times

Travel times of first arrival P-wave refractions were picked for every fifth shot gather along each MCS line. This corresponds to picking at a spacing of approximately 188.5 meters, which falls within the first Fresnel zone of $\sim$200 m at the seafloor. In areas where a fifth gather was of poor quality, two nearby gathers were substituted in that interval to maintain at least one sampling in each Fresnel Zone. Travel times from all receivers were picked if each recorded a clear and continuous arrival (Figure 2b, 3a). Despite SOBE processing, in some cases it was not possible to pick the arrival all the way in to nearest offset, and this near offset data may have been missing from the original surface recording. In some areas of rough topography and low subsurface velocities, the water wave does not collapse down to a single point, but continues to have some finite width that obstructs the first refracted arrival in a handful of the nearest offset traces (Figure 3).

Data quality is generally good for most shot-receiver pairs, with the exception of a few locations where the SNR is lower due to a variety of possible factors. Complicated subsurface structure (Figure 3b), side-swipe from nearby seafloor structure (Figure 3c), and rough seafloor topography (Figure 3d) may all lower the SNR. Although minimized where possible, migration artifacts from noise and amplitude variability can also interfere with actual arrivals reducing the clarity of the arrival. No picks were made for receivers with intersecting noise or at breaks in the refracted arrivals. Where possible, traces with low SNR were picked

by comparison with traces of the same offset in nearby shots.

Pick uncertainties for lines A4, A6, A9, and A10 were generally between 10-30 ms, with 40 ms being the highest uncertainty assigned (Table 1). Line A5 pick uncertainties were assigned larger values, between 24-80 ms, due to a lower signal-to-noise ratio caused by the rough topography associated with the hanging wall along this line (Figure 1). Travel times for the first refracted arrival were picked both by hand and cross-correlation. When the cross-correlation technique was employed, the generated picks were visually inspected and adjusted by hand if necessary. Pick coverage for the five OCC lines covering the massif is shown in Figure 4. The coverage is evenly distributed along lines and the near-offsets are well sampled.

2.2.4 Tomographic Inversion

We follow the method of *Van Avendonk et al.* (2004) to perform tomographic inversions of first crustal refraction travel times of the SOBE data. Our goal is to obtain the smoothest models that fit the data within the pick uncertainties with the fewest number of iterations. To measure the success of this travel-time fitting, the weighted misfit functional value χ^2 is used:

$$\chi^2 = \frac{1}{N} \sum_{i=1}^{N} \frac{(T_{obs,i} - T_{pred,i})^2}{\sigma_{unc,i}} \tag{2.1}$$

where T_{obs} is a picked travel-time, T_{pred} is a predicted travel-time of the ray through the current model, σ_{unc} is a pick uncertainty, and N is the total number of picks. Models are updated by minimizing the misfit between the predicted times and the picked times in a least squares sense. Iterations are performed to fit the data until smoothing constraints are satisfied and an overall misfit $\chi^2 \approx 1$ is achieved (Table 1), indicating the desired fit of the observed travel-times to within their uncertainties. Attention is paid to overall travel-time fit (represented by the χ^2 value), as well as to the distribution of misfit in individual shot gathers and regions (Figure 4).

Table 2.1: Select Inversion Parameters and Results for Preferred Models

Line	χ^2	$TTResids_{initial}$ mean, [abs(max)]	$TTResids_{final}$ mean, [abs(max)]	Uncert, σ	Horiz:Vert Aspect Ratio
A4	1.07	35.4, [189.6] ms	-1.9, [77.0] ms	10-20 ms	2
A5	0.94	-25.7, [440.2] ms	-3.9, [92.6] ms	24-80 ms	3
A6	1.03	10.4, [166.2] ms	-2.9, [83.5] ms	15-30 ms	2
A9	1.12	-45.1, [256.1] ms	-0.3, [106.8] ms	12-40 ms	2
A10	0.89	-4, [230.6] ms	-2.9, [82.5] ms	15-30 ms	2

The tomographic inversions of each line proceeded through a series of linearized 2D inversions, followed by model update, and ray tracing in the new model. At each inversion step, the target misfit reduction was chosen small enough to satisfy the linearity assumption and the smoothing trade-off parameter was adjusted by the program to hit the target misfit (*Van Avendonk et al.*, 2004). The models converged to their final misfits of 0.89 - 1.12 in 7 to 11 iterations (Table 1). The parameter controlling the relative strength of horizontal to vertical smoothing, a value chosen subjectively based on *a priori* expectations of the structure, is reduced as the inversion progresses to promote more rapid convergence of the model. Varying these parameters in this way allows the inversion first to fit large scale structure required by the data, and then to fine-tune smaller scale features. A low value of 2 or 3 (Table 1), depending on the model, for the final ratio of horizontal to vertical smoothing required to fit the data, indicates strongly laterally heterogeneous structure. The sequence of reductions in the aspect ratio parameters differs for each inversion for our preferred 2D models. This enables optimal fits for each line and allows different scales of structure to be resolved for each profile depending on what is required by the data. The grid spacing used in all inversions is 50 m in the x-direction and 25 m in the z-direction.

For all the inversions, the starting model was a 1-D velocity profile, previously used in early downward continued tomographic analysis of line A10 (*Harding et al.*, 2007), hung from the seafloor (1D profile shown as inset in Figure 5). High residual travel times of the picks traced through the starting model indicate that the initial model deviates significantly from the actual velocity structure at Atlantis

Massif (Table 1).

Figure 4 shows the travel-time residuals of the picked data with respect to the preferred models for each MCS line. The residuals are significantly lower in the preferred models than in the starting models indicating a marked improvement in structural fidelity of the preferred models (Table 1). The residuals are typically <50 ms (maximum of <100 ms) throughout the profiles indicating that all parts of the model are fit about equally well by the data.

Misfit problems arise in some areas of rough topography (scattering) due to difficulty in travel-time picking, in the vicinity of drastic slope changes, and where the bathymetry profile used in the inversion differs slightly from the actual bathymetry due to inadequate sonar centerbeam resolution. Mismatch of bathymetry results in high residuals that create diagonal streaks in shot-receiver space (Figure 4c) along a series of adjacent shots. Occasionally single or a few traces will have weak amplitude of the first arrival, probably due to out-of-plane side-echo caused by local 3D structure creating destructive interference or to rough, steep topography. These traces cannot be picked. In areas of very high velocity gradients just beneath the seafloor, as in the central portion of line A6 (Figure 6a), the inversion has some difficulty in resolving the very low velocity top layer ($\sim$100 m thick) above higher velocity material. This causes the nearest offset residuals for that region (Figure 4a) to remain high despite the use of decreased vertical smoothing and starting models with low velocity top layers.

2.2.5 Line A8

Modeling of Line A8 was slightly different from what has been described above. The data were processed to a datum using the SOBE technique as for the other lines, but traveltime picking and inversion were done following the procedures described in *Canales et al.* (2008). Traveltime picking was done by combining manual picking with a semi-automated first-break picking routine. The tomographic inversion was conducted using a regularized non-linear inversion with spatial smoothing constraints on the roughness of the model (*Zelt and Barton*, 1998). This inversion method employs models with continuous velocities. Unlike

the OCC line inversion technique (*Van Avendonk et al.*, 2004), it thus does not allow for an explicit velocity discontinuity at the seafloor. This flexibility is useful for the OCC profiles where basement velocities and gradients are higher and water depths are shallow enough that the shallowest turning energy is recorded within the streamer aperture.

2.3 Tomography Results

Our preferred tomographic models for P-wave velocity structure of the five MCS lines covering Atlantis Massif are shown in Figure 6 (a-e). On scales of less than a kilometer, the models exhibit an extreme degree of lateral heterogeneity when compared with the compilation of young Atlantic crustal velocity values published by *White et al.* (1992). Plots of deviations of the tomographic models with respect to the initial one-dimensional starting model for the OCC lines are particularly useful for identifying lateral variations in velocity structure across the Atlantis Massif (Figure 5). In our models, crustal velocity values vary between 2-7.5 km/s, with few locations exceeding 7 km/s. Because of the shallow high velocities, high velocity gradients, and the fixed 6 km streamer length, refraction ray coverage in this experiment is limited approximately to the upper 1.5 km of structure.

While we do notice patterns in absolute velocities, our results do not show a well-defined classification scheme for velocity gradients, in contrast to what *Canales et al.* (2008) and *Xu et al.* (2009) describe for several Atlantic OCCs. These two prior studies note that as absolute velocities at the seafloor increase, velocity gradients increase as well: where seafloor velocities are <3.4 km/s, gradients are <1 s^{-1}; areas with velocities between 3.4-4.2 km/s have gradients ranging from 1-3 s^{-1}; and where velocities are >4.2 km/s, gradients are >3 s^{-1} (*Canales et al.*, 2008; *Xu et al.*, 2009). In our results, velocity gradients range from ∼1-6 s^{-1} in the upper 500 mbsf where gradients vary the most, mainly independent of absolute velocity (Figure 7a). By 750 m below seafloor, nearly all velocities (except Line A5 in the region of extrusive volcanic material) reach values ranging from 4-6.5

km/s, well into velocities corresponding to intrusive, rather than extrusive, rock. We attribute the lack of correlation between gradients and absolute velocities to the improved vertical resolution of the SOBE tomography models, which confines high gradients to the shallowest parts of the structure.

We choose to divide vertical velocity profiles into three groups, similar in velocity but not gradient, to the aforementioned groupings of *Canales et al.* (2008) and *Xu et al.* (2009), to aid in interpretation of rock type from seismic velocity. These groupings are as follows: a group with slow surface velocities between 2-3 km/s and base-of-coverage velocities of 4-4.5 km/s; an intermediate velocity group with surface velocities between 3-4.5 km/s and base-of-coverage velocities of 4.75-5.5 km/s; and a group with the highest velocities, >4.5 km/s at the seafloor trending to 5.5-7 km/s at the base of coverage. Figure 7b shows velocity-depth profiles taken from various locations throughout the models to illustrate the three velocity groupings we have defined. The locations of the velocity-depth profiles are noted and were chosen because they represent the clearest examples of the distinct velocity structures associated with discrete portions of the massif.

To highlight deviations from the accepted norm, it is useful to compare our models to the seismic velocity structure (and later to the lithologic structure) of the classical, homogeneously layered, model of oceanic crustal structure. This Penrose model, based on ophiolite structure, consists of upper crust, divided into extrusive pillow basalts (layer 2A) atop sheeted dikes (layer 2B), overlying gabbro (layer 3), which in turn overlies the uppermost mantle (*Penrose*, 1973).

One difficulty we face when interpreting the different velocity groupings of Atlantis Massif is to characterize the structure of 'normal' oceanic crust at slow spreading ridges. This difficulty arises in part because of the heterogeneity of crustal structure and in part because of the difficulty in obtaining reliable results, particularly for the shallowest crust. One, often used, means of characterizing the range of normal crust is to use compilations of previous velocity models such as *White et al.* (1992). Unfortunately, the results in this compilation are almost certainly too high to represent the velocity of extrusive volcanics. The seafloor velocities in the *White et al.* (1992) compilation range upwards from 2.7 km/s (Figure

7c), while measurements of seafloor velocity at fast and intermediate spreading rate ridges are typically in the range 2.0-3.0 km/s (e.g. *Harding et al.*, 1993; *Christeson et al.*, 1994; *Canales et al.*, 2005). The latter range spans the detailed results for the MAR from *Hussenoeder et al.* (2002) for 35°N on the MAR and *Seher et al.* (2010) for the Lucky Strike segment. We use results from line A8 on the conjugate crust across the ridge and the hanging wall section of line A5, together with a more extensive analysis of the Lucky Strike velocity range for 3-D tomography (*Arnulf et al.*, 2011; *Arnulf*, 2011) as the representation of non-OCC young Atlantic crustal values used for comparison with the Atlantis Massif results (Figure 7c).

2.3.1 Strike-Parallel Lines (Lines A6, A4, A5)

The westernmost and central ridge-parallel lines (A6 and A4, respectively; Figure 6a, b) show a similar overall velocity pattern consisting of high velocities near the surface in the center of the lines grading into lower velocities on the south and north ends. Line A6, in older crust, however, exhibits a thicker section of lower velocities over the central part of the line when compared with line A4. The portion of line A6 between -3.5 km and -0.5 km in model space is also the location of highest velocity, with values >7.5 km/s at the base of the coverage (∼1500 mbsf). The Southern Ridge velocities of 3-5 km/s contrast with the Central Dome velocities of 3.5-6.5 km/s as pointed out by *Canales et al.* (2008).

Line A5, the easternmost ridge-parallel line crossing the remnant piece of hanging wall block, shows very low velocities similar to those obtained for young, volcanic Atlantic crust using the SOBE method at the Lucky Strike segment of the MAR (Figure 7c) (*Arnulf et al.*, 2011). These low velocities grade laterally very rapidly into high velocities in the 5-6 km/s range where the profile images the eastern flank of the Southern Ridge (Figure 6c). Neither here nor on line A10 do our inversions image a distinct velocity feature that might correspond to a detachment fault zone beneath the hanging wall. This could reflect a lack of distinct velocity structure or it could reflect the limited resolution of our models (∼100 m) compared to the expected thickness of the detachment zone (∼15-100 m), based on structural and metamorphic geology studies at Atlantis Massif (e.g.

Schroeder and John, 2004; *Karson et al.*, 2006; *Blackman et al.*, 2011; *McCaig et al.*, 2010).

2.3.2 Strike-Perpendicular Lines (Lines A9, A10)

The two spreading-parallel lines, A10 and A9 (Figures 6d and 6e, respectively), are the most heterogeneous in terms of velocity structure. Line A9, sampling the Southern Ridge, has velocities as high as 5 km/s directly at the seafloor on the eastern flank. The top portion of the massif in the central and western Southern Ridge and its western flank are significantly different than its eastern flank. A transition takes place across a few hundred meters lateral distance from high surface velocities in the east down to low values between 2.5-3 km/s in the center and western portions (Figure 6e). In the central and western Southern Ridge, velocity structure is similar to, but slightly faster than, young Atlantic crust (Figure 7b) (*Arnulf et al.*, 2011).

For line A10 crossing the Central Dome, the highest subseafloor velocities (>5.5 km/s) are near the shallowest part of the Central Dome, several kilometers to the west of the high velocity peak of line A9. To the west in profile A10, as in A9, velocity values rapidly transition to significantly reduced crustal values over a few hundred horizontal meters (Figure 6d). These lowest velocities are found on the westernmost part of the line nearest the breakaway. On the eastern flank, line A10 samples the low velocity hanging wall underlain within 500 meters subseafloor by velocities >5 km/s.

2.3.3 Conjugate Ridge Flank Line A8

Line A8 (Figure 6f) runs along crust that was accreted at the time of formation of the OCC but was transferred to the conjugate flank, therefore it was part of the hanging wall to the detachment fault. Seafloor morphology along the line is characteristic of volcanic terrain (e.g. *Smith and Cann*, 1993), suggesting that this profile represents primarily structure corresponding to extrusive volcanics. This profile shows overall less heterogeneity than the rest of the models, and its average

velocity is the lowest of all (Figure 6, 7c). It shows similar structure to the northern section of A5 over the hanging wall, with shallowmost velocities of 2 km/s increasing to 5 km/s at 1.5 km bsf.

2.3.4 Model Resolution

Very dense ray coverage exists in the portions of the models presented (down to ∼1.5 km; Figure 6) with the exception of small slivers <100 m wide at the trailing end of the lines. The models are truncated (in white) in areas where rays only provide nominal influence on the structure. Thus we can resolve nearly all structure greater than a couple hundred meters in size.

In areas where residuals are non-zero indicating an imperfect fit to the data (Figure 4), uncertaintly of the models is modest. On line A6 for example, the nearest offset residuals are consistently about 50 ms (Figure 4a); we attribute this to a possible thin low velocity layer that is difficult for the inversion to resolve. In order to reconcile this 50 ms discrepancy, the topmost layer of line A6 (∼150 m and 3.5 km/s in preferred model) would need to be ∼170 m thicker or ∼0.5 km/s slower.

2.4 Discussion

2.4.1 SOBE

This study provides the first application of the SOBE technique in a shallow, high-relief topographic area with subsurface structure consisting of very high velocities and gradients. The SOBE technique provides improvement over regular shot gathers in areas of shallow, smooth topography and high subsurface velocities. In these areas, such as over the eastern Southern Ridge and atop the Central Dome, SOBE gathers show clear, robust, and coherent arrivals that are easily tracked and picked (Figure 2b, 3a). During the downward continuation process, few processing artifacts obscure the data in these settings.

In areas of rougher topography, SOBE produces data of high enough quality

to obtain a reasonable model, which may not be the case for standard surface data. In these rough areas, such as the hanging wall of line A5, refractions are weaker and arrivals are shorter than in areas of smooth topography and high velocities (Figure 3), but nonetheless SOBE provides an improvement over standard shot gathers in these areas.

As evidenced by the residuals for line A5, great improvement in the fit of the model occurs over the high velocity, shallow Southern Ridge portion of the profile (Figure 4c, x=-14 to -9 km). Over the rough topography and very low velocity portion of this line (Figure 3c, x=-4 to 6 km), there is a broader range of residual values that have no coherent distribution. Roughness of topography causing side scatter together with slight misfit between centerbeam bathymetry and seismically-determined seafloor may also contribute to this problem.

2.4.2 Lithology/Velocity Correlation

Lithologic interpretations of our seismic results are guided by groundtruth data. As seismic velocities are non-unique and individual outcrops may be smaller than the dimensions we can resolve, we aim to interpret general, dominant lithologies only. Some rock types have characteristic velocity ranges that may overlap, so we use available independent constraints to distinguish between lithologies. With the exception of the drill site on the Central Dome, all samples from Atlantis Massif are from within ∼500 m of the pre-mass wasting surface of the OCC (*Schroeder and John*, 2004); headwall scarps at the top of the South Wall allow seafloor access beyond the typical few meters. In Figure 6, we project onto each profile the results of rock sampling within ∼2 km of a given profile so seismic structure can be readily compared with surface samples.

Relatively High Velocity Body (HVB)

At Atlantis Massif, our models show high seismic velocities, 5 km/s or greater, outcropping essentially at the seafloor or within a couple hundred meters of the seafloor in several regions. Such high values at shallow depths are atypical for young Atlantic crust based on previous seismic studies (*White et al.*, 1992;

Hussenoeder et al., 2002; *Arnulf et al.*, 2011; *Arnulf*, 2011), although with the recent recognition of the prevalence of detachment faulting and core complexes at slow spreading centers (*Smith et al.*, 2006, 2008; *Escartín et al.*, 2008) these high velocities may occur more commonly than previously understood. The high velocities are also clearly distinct from the structure on the conjugate flank, which indicates that lithospheric accretion during OCC formation is highly asymmetric. Our seismic results thus support the extensive evidence previously documenting asymmetric lithospheric accretion (e.g. *Kuo and Forsyth*, 1988; *Allerton et al.*, 2000; *Okino et al.*, 2004).

When addressing the lithologic ambiguity of seismic velocities in this case, we rule out the likelihood that these high velocities represent weakly fractured peridotite or minimally altered serpentinite because we expect degrees of alteration in both cases to exceed those that would produce *in situ* velocities significantly larger than 5 km/s (see subsequent discussion). Estimates for the amount and degree of serpentinization indicate moderate to major alteration of peridotite has occurred (*Blackman et al.*, 2002; *Früh-Green et al.*, 2003), making minimally serpentinized, or fractured yet unaltered, peridotite unlikely.

Instead, this zone of velocities is characterized by the following features previously associated with gabbro (*White et al.*, 1992): velocities >5.5 km/s close to the seafloor, and a relatively low velocity gradient. IODP Hole U1309D, which is situated within this high velocity zone, retrieved predominantly gabbro down to a depth of 1.415 km (*Blackman et al.*, 2006, 2011). The borehole sonic log velocities from U1309D (*Collins et al.*, 2009) are in good agreement with the vertical velocity profile taken from the nearest shot on the line nearest to the location of the drill site (Figure 8a). *Canales et al.* (2008) also interpret similar seismic velocity structure at the Kane and Dantes Domes OCCs as gabbro based on seafloor samples from Kane and drilling results from Atlantis Bank OCC on the Southwest Indian Ridge (*Dick et al.*, 2000). We therefore associate the highest velocities in our models, the high velocity body (HVB), with rock of predominantly gabbroic composition.

Lines A10 and A9 show that the high velocity body(ies) of the Central Dome occurs ∼3.5 km to the west of the velocity high in the Southern Ridge

(Figure 6d, e). Figure 8b shows the approximate extent of the HVB, projected onto the seafloor, based on our models. The peaks of the high velocity material are offset between the Central Dome and Southern Ridge in such a way that high velocity material in the south would have been emplaced ∼0.15-0.3 Myr later than high velocity material in the Central Dome, assuming that the OCC-bearing ridge flank accommodated 50-100% of the uniform full spreading rate of 24 km/Myr (*Sempéré et al.*, 1995; *Zervas et al.*, 1995). Although there is no age dating from the Southern Ridge gabbroic core, age dating performed on material from the IODP drill hole suggests that construction of the Central Dome gabbroic core took place in two magmatic events spanning a period of as much as 0.15 Myr (*Grimes et al.*, 2008). Therefore, it is possible that the gabbroic core in the Southern Ridge was constructed ∼3.5 km to the east as part of the second (and perhaps even subsequent) construction event(s).

From our seismic results alone however, we cannot definitively distinguish between a high velocity regime that is continuous or made up of discrete few-km scale bodies. In a subsequent section we describe possible scenarios for interplay between detachment faulting and intrusive magmatism that could produce the imaged structure.

Intermediate-Valued Velocity Layer (IVVL)

In contrast to the high velocity areas peaking near the surface of the massif, there are also sections of the models composed of comparatively lower velocity material that are nevertheless distinct from extrusive velocity values (Figure 7b). Characteristics of the Intermediate-Valued Velocity Layer (IVVL) fit within the bounds of typical young Atlantic crustal velocities and gradients (*White et al.*, 1992) but have surface velocities slightly higher than what we now know layer 2A velocities to be (Figure 8c) (*Hussenoeder et al.*, 2002; *Arnulf et al.*, 2011; *Arnulf*, 2011). The properties of these packages could indicate a crustal section composed of basalt atop either sheeted dikes (*Spudich and Orcutt*, 1980) or highly serpentinized harzburgite. This is based on groundtruth observations (Figure 9) and on surface velocities in the upper couple hundred meters. The projection of the

spatial extent of the IVVL, inferred from our seismic results, onto the seafloor of the massif is shown in Figure 8d.

The strike-parallel lines A4 and A6 show that the Southern Ridge and the northernmost 2-5 km of these two profiles are comprised of IVVL packages: 2.7-4 km/s at the seafloor increasing to >5.5 km/s at the base of the coverage (1.2-1.7 km; Figure 6a, b). Submersible dives on the South Wall (*Blackman et al.*, 2002; *Kelley et al.*, 2005; *Boschi et al.*, 2006) recovered many samples of mostly serpentinized harzburgite and lesser gabbros near regions of IVVL velocities. On the Southern Ridge, situated atop IVVL velocities, is the Lost City Hydrothermal Field with a known serpentinite host rock composition (*Kelley et al.*, 2001; *Früh-Green et al.*, 2003; *Kelley et al.*, 2005). In addition, velocities of the IVVL are significantly faster than those observed along line A5 in the hanging wall and line A8 in the volcanic conjugate crust (Figure 7b), which suggest that they represent lithologies different from extrusive volcanics. We thus equate this IVVL zone with the intermediate V2 velocities of *Canales et al.* (2008) and attribute them to lithology dominated by serpentinite on the South Wall and western and central Southern Ridge.

Seismic velocities of variably altered, hand-sample-size serpentinite from the Mid-Atlantic Ridge at Kane Fracture Zone (MARK), vicinity of the Kane OCC, are presented by *Miller and Christensen* (1997). For <90% alteration, measured velocities exceed those we equate with serpentinite. We note, though, that measurements on the MARK samples were made at confining pressures of 200 MPa, corresponding to conditions in the lower crust or upper mantle and ensuring the closure of microcracks within the samples. Confining pressures in the upper kilometer of the Southern Ridge are between ∼10-40 MPa. At these pressures, the presence of open microcracks can reduce velocities by up to ∼0.5 km/s, allowing our measurements to be consistent with smaller degrees of serpentinization. Moreover, *in situ* velocities measured by seismic waves may also be affected by large scale fracturing or by the mixture of rock compositions found at the Southern Ridge (Figure 9) (*Blackman et al.*, 2002). These factors cause a reduction in the seismic velocity of the IVVL compared to the serpentinite measurements of *Miller*

and Christensen (1997).

Deformed Sheath Hypothesis

The deformed, altered sheath hypothesis (*Ildefonse et al.*, 2007) of OCC formation can be analyzed in context of the seismic velocity models presented here. This hypothesis proposes a strong intrusive core surrounded by a sheath of weakened, serpentinized mantle rock where strain-localization and slip were concentrated during detachment fault initiation. Our models and the drilling results (*Blackman et al.*, 2011) show that mafic intrusions are present in the upper ∼1.5 km of Atlantis Massif. This requires that these high velocity body(ies) were somehow exhumed from their originally deeper intrusion level, consistent with the deformed sheath hypothesis. The *Ildefonse et al.* (2007) model requires mafic intrusions at the core of an OCC, but it is unclear whether it requires a centrally located pluton or one skewed toward the breakaway or terminus, as observed from our models. We also observe, at least in the Southern Ridge, surface serpentinites and a velocity profile that is consistent with a deformed altered sheath. Shear zones are observed within this serpentinized material (*Schroeder and John*, 2004; *Karson et al.*, 2006) where some slip occurred that is consistent with the prediction of *Ildefonse et al.* (2007). Our results do not provide enough information to definitively discern whether or not a serpentinized sheath of material encompassed the entire massif during its initial formation. If it existed, a sheath of such extent could have significantly thinned during fault displacement or been rafted away with the hanging wall. Our seismic velocity models are nevertheless consistent with the deformed, altered sheath mechanism for fault initiation and slip.

Outward-Facing Western Slope

Additional low velocities are observed on the western outward-facing slope of the massif located west of x = -10 km in profiles A9 and A10 (Figure 6d, e). These velocities are similar to the IVVL but notably have lower velocity gradients in the upper ∼500 meters (Figure 8c, line A9 at x = -10 km versus line A9 at x = -4.5 km and line A4 at x = -10 km). In contrast, the velocity-depth profile

from line A6 in IVVL velocities (Figure 8c) shows a similar velocity gradient to the outward-facing slope velocities, but the overall velocities are higher. This apparent similarity in gradient is attributed to the inability to resolve the shallowest low velocity layer on line A6 as discussed previously. Preliminary 3D inversions, however, are better able to image a low velocity cap over line A6 further distinguishing it from the outward-facing slope velocity gradients.

The outward-facing slope is interpreted as the location of transition into more normal upper crust and probably has an extrusive volcanic top layer. The velocities and gradients are similar to the young Atlantic crustal velocity structure of *Arnulf* (2011). This interpretation is consistent with the volcanic ridge described by *Smith et al.* (2006, 2008). Volcanic terrain was imaged in Argo-II video near this area (∼30°08.25N, ∼42°12.5W on Figure 9) (*Blackman et al.*, 2002) and a gravity deficit compared to the surrounding residual Bouguer anomaly points toward the presence of upper crustal rock (Figure 8b) (*Blackman et al.*, 2008). This interpretation of upper crustal composition requires that the breakaway of the OCC is near x = -10 km in model space on line A9 and is as far east as x = -7 km on line A10, which is near the location of the breakaway defined by *Tucholke et al.* (1998) and *Canales et al.* (2008), in 1.8-1.9 Ma crust (based on magnetic anomalies by *Sempéré et al.* (1995)); this is very close to the western edge of the Southern Ridge.

Volcanic Hanging Wall

The lowest velocity structure (observed only in line A5 hanging wall and line A8 conjugate crust) most likely composes basalts (Figure 6c, f). Rock samples obtained from near where profile A10 crosses these lowest velocities on line A5 consist entirely of basalt. Side-scan images, video, and submersible mapping record pillow basalts and hummocky volcanic structures at the surface in this area of the massif (*Blackman et al.*, 1998, 2002), in support of our interpretation of extrusive volcanic composition. Likewise, seafloor morphology and limited side-scan sonar tracks on the eastern flank of the ridge axis suggest an extrusive volcanic lithology (*Blackman et al.*, 1998).

Fresh Mantle

Nowhere in our coverage of Atlantis Massif are mantle velocities of 8 km/s or greater observed. An OBS refraction study analyzed deeper velocity structure, to 7 km in parts, and precludes fresh mantle velocities at depths shallower than 4.5 km bsf within the Central Dome of the massif (*Blackman and Collins*, 2010). The lack of evidence for fresh mantle rocks does not preclude the presence of ultramafic rocks within the massif with velocities lower than 8 km/s due either to cracks and fractures or to alteration. Indeed, as discussed previously, we believe significant portions of the Southern Ridge are composed of serpentinite.

2.4.3 Correlation of Corrugations and Velocity Structure

Our observations indicate that surface corrugations and striations, a defining morphologic feature of OCCs (*Cann et al.*, 1997), are present on the massif surface nearly everywhere that unusually high subsurface velocities are present (Figure 9). Corrugations and surface striations are also present in some areas of lower velocities not indicative of extrusive volcanic lithology. The central portion of line A9 and the southern portions of lines A4 and A6, all on the Southern Ridge, show corrugations capping a region where we determine subsurface IVVL velocities (Figure 9). Also shown by Figure 9, along line A10 west of the line A6 intersection, lithospheric velocities decrease steadily across a region where corrugations have been mapped (*Blackman et al.*, 2002). These observations reinforce the general correlation between corrugations and intrusive material with high seismic velocity structure as implied by *Tucholke et al.* (2008), but the correspondence is not exclusive. We also note that seafloor corrugations can cap material that we infer to be altered ultramafic rock.

2.4.4 Correlation with Gravity Structure

Our seismic models and our lithologic inferences qualitatively match the preferred residual Bouguer gravity anomaly (RBA) model of *Blackman et al.* (2008). In their preferred model, the density contrast at the water/crustal in-

terface is 1600 kg/m^3, and that of the upper crust/lower crust boundary is 300 kg/m^3. The lower crust, assumed to have a density of 2900 kg/m^3 based on the average density of material from Hole U1309D (*Blackman et al.*, 2006), shoals almost to the seafloor in the central portion of the massif in this model. Despite the removal of a lower crustal component, a positive RBA (∼15-20 mgal) exists over the eastern Central Dome and Southern Ridge (Figure 8b).

The skewness of the positive gravity anomaly correlates well with the distribution of the high velocity sections in our models that we have interpreted as a gabbroic body(ies). In the Southern Ridge, we confirm that the positive anomaly in the preferred gravity model most likely represents an additional mafic component in the east of the Southern Ridge suggesting that it is composed of material similar to the Central Dome based on the similar magnitude of anomaly in these areas. This argument is in agreement with the model of *Ildefonse et al.* (2007).

A relative mass deficit shown by the RBA (Figure 8b) over the central and western Southern Ridge is a positive anomaly of smaller magnitude (∼5 mgal) compared to the larger positive anomaly (∼15-20 mgal) modeled in the Central Dome and eastern Southern Ridge (*Blackman et al.*, 2008). This ∼5 mgal anomaly in the western and central Southern Ridge could occur due to remaining material of lower density, possibly of serpentinite or porous mafic composition. This is consistent with our interpretation of a transition to classical crustal composition on the outward-facing slope of Atlantis Massif.

2.4.5 Magmatism and Gabbroic Bodies at Atlantis Massif

The high velocity body(ies) with 4.5-5.5 km/s at the seafloor and extending throughout the MCS refraction depth coverage are interpreted as a gabbroic body or bodies consistent with IODP drilling at Atlantis Massif (*Blackman et al.*, 2006) and at other OCCs (*Dick et al.*, 2000; *MacLeod et al.*, 2002; *Kelemen et al.*, 2004). This lithology indicates that plutons were present or that magmatism was active at the ridge during the initiation of Atlantis Massif, and recent models (*Buck et al.*, 2005; *Tucholke et al.*, 2008; *Olive et al.*, 2010) would predict that intermediate levels of magmatism accounting for ∼30-50% of lithospheric accretion were

characteristic of the period between initiation and termination of this core complex. This body(ies) would have been emplaced into a mainly peridotitic host rock exhumed during the dominantly extensional phases of lithospheric accretion.

The shape of the high velocity anomaly at Atlantis Massif (Figure 8b) suggests a magmatic source that evolved through time and space, rather than remaining in a constant location over the formation period of the OCC. The body(ies) is centered beneath the Central Dome to the north but it comprises only the eastern flank of the Southern Ridge to the south; there is a ∼3.5 km difference in the position of high velocities in the spreading direction between the two spreading-parallel profiles (Figure 6d, e). Although we interpolate a single boundary for the HVB between seismic profiles (Figure 8b), we cannot definitively conclude that the Central Dome and Southern Ridge gabbroic bodies are continuous as our profiles are spaced too far apart to observe a boundary between gabbroic bodies, if one exists.

Based on the velocity models, a transition between the Central Dome and Southern Ridge may occur at about x=-7.5 km along line A4 and x=-6.5 km on A6 (Figure 9, dashed line), where the velocity difference from the starting model changes from positive to negative (Figure 5a, b). Following the interpretation of *Canales et al.* (2008), this may support the inference of *Karson et al.* (2006) that the Central Dome and Southern Ridge are made of two distinct crustal blocks. However, there is no clear surface-trace of a lateral fault in that region. We note that a slight difference in the starting model could change the location of a gradual transition from positive to negative velocity anomalies as seen in line A6 (Figure 5a), but would not affect the location of the high gradient transition like that in line A4 (Figure 5b).

Systematic analysis of the IODP drill core U1309D (*John et al.*, 2009) suggests that the HVB, at least in the Central Dome region, is composed of a series of sills injected individually and age dating confirms this (*Grimes et al.*, 2008). From our data, it is not possible to determine if the magmatic source remained constant, injecting material steadily for the duration of its evolution, or if it comprised discrete magmatic pulses forming a main body or section of bodies first in the north,

then subsequently in the south. Whether this is the case or not does not affect the main conclusions of our model.

We propose an evolutionary history of the magmatic source based on the simplest explanation constrained by the data: the magmatic source underwent continuous emplacement throughout OCC formation building up to two discrete ∼5-10 km-scale bodies, and the rates of along axis movement of the source and of seafloor spreading (rates based on length and age of Atlantis Massif, and based on dating by *Grimes et al.* (2008)) controlled the shape of the resultant pluton(s). Thus, as the magmatic source moved south along the ridge axis, the continuous spreading of the plates rafted portions of the body off-axis to greater distances in the north than in the south (Figure 10). This hypothesis predicts that a diagonal or curved gabbroic body(ies) underlies Atlantis Massif as inferred from the seismic models and residual gravity anomaly (*Blackman et al.*, 1998, 2008).

At time t1, magmatic emplacement takes place at the ridge in the along-axis position of the present-day Central Dome (Figure 10a). As the hot pluton contributes to the buoyancy forces experienced by the lithosphere, it begins to be spread off axis. Meanwhile, the magma source migrates southward where it injects a second pluton at time t2 in the along-axis location of the present day Southern Ridge (Figure 10b). The source could just as likely undergo continuous emplacement during southward migration, but for a simplified time series, we illustrate and describe the process with two discrete bodies. This second body emplaced at time t2 is uplifted and rafted off axis in the same way as the first pluton. At time t3, two plutons exist (or one continuous pluton) with the northern body farther from the spreading axis and the southern body closer (Figure 10c).

It is prudent to note that a magma source that dips from north to south in the lithosphere could create a similar geometry. This, however, would not be consistent with the sill injection mechanism proposed by *Grimes et al.* (2008) which requires more recent injections to occur higher in the lithosphere than the initial magmatic episode. Our model of a propagating source does not confine the depth of the magmatic injections, which may be inserted directly into the footwall (*Tucholke et al.*, 2008).

2.4.6 Implications of the Magmatic History for Detachment Fault Formation and Unroofing Mechanism

Many studies have argued that magmatism is an important factor in the formation of detachment faults (*Dick et al.*, 2002; *Buck et al.*, 2005; *Ildefonse et al.*, 2007; *Tucholke et al.*, 2008; *Olive et al.*, 2010). The existence of plutonic bodies at Atlantis Massif confirms the presence of magmatism. *Ildefonse et al.* (2007) propose a model where detachment faults form as strain nucleates in the weakened material at the edges of a magmatic body emplaced into ultramafic host rock. We favor this hypothesis for the nucleation of the detachment fault because it is consistent with the near surface exposure of gabbroic bodies and the observed morphology and rock types at Atlantis Massif (*Blackman et al.*, 2011) and draws support from alteration analysis indicating that alteration to weak minerals occurred around the boundaries of magmatic injections at this OCC (*Nozaka and Fryer*, 2011).

We propose a model of detachment fault formation and geometry in which a southeast dipping detachment fault formed at Atlantis Massif during, or soon after, the southward propagation of the magmatic source. The detachment nucleates at the interface between host rock and pluton (*Ildefonse et al.*, 2007), first in the north at the site of earliest emplacement. This requires a breakaway that is subparallel to the spreading ridge (Figure 11a), which is possible based on the morphology of the western flank of Atlantis Massif (*Cann et al.*, 1997; *Blackman et al.*, 1998). Simultaneously, plate spreading and slip on the newly forming detachment fault proceed. The fault continues to cut deeply southward into the crust at the plutonic boundary, which is deeper in the lithospheric section in the south than its concurrent position in the north where it has already undergone uplift. This process is the mechanism for formation of a southeast dipping fault that cuts deeper into the lithosphere in the south than in the north (Figure 10 and 11a). After the development of the detachment fault, plate spreading is accommodated dominantly on this fault for at least 0.2 Myr, the period of OCC formation determined by age dating conducted by *Grimes et al.* (2008) (Figure 11b). Corrugations form on the footwall marking the spreading-parallel relative motion of fault blocks

during detachment slip (Figure 9) (*Cann et al.*, 1997; *Tucholke et al.*, 1998, 2008).

Unroofing of the footwall to a southeast dipping detachment fault will form morphology similar to that of Atlantis Massif (Figure 1) based on an increasing north to south gradient in isostatic uplift as well as the exposure of originally deeper and more ultramafic rock in the south, where the fault cuts deeper. The amount of mass removed from above the south part of the footwall will exceed that removed from the north due to the orientation of the fault, which cuts a wedge-shaped hanging wall (Figures 10 and 11b). When an uneven mass of material is removed from the top of the fault, isostatic compensation will vary along strike (Figure 11b, c) causing the crust to be uplifted higher in the south than in the north (Figure 11d).

The hanging wall material displaced by motion on the detachment fault, at least in part, still exists atop the northern two-thirds of Atlantis Massif. The velocities in our models suggest however, that the part of the hanging wall that once covered the Southern Ridge must have been removed by some mechanism that cannot be determined from the seismic data. Both mass wasting of the material or transfer of the southern portion of hanging wall onto the outside corner conjugate crust are possible explanations for its absence atop the massif. Exactly how much material comprised the southern section of the hanging wall is unknown. If the core pluton(s) of Atlantis Massif were emplaced into ultramafic host rock, as suggested here and by *Ildefonse et al.* (2007), a relatively lesser amount of hanging wall of dense ultramafic composition would need to be removed to account for the uplift of the Southern Ridge. Alternatively, if the pluton(s) were emplaced into normal young Atlantic crust and the hanging wall was composed of extrusive, mafic material, removal of larger volumes would be required to spur uplift. We prefer the former explanation of host rock composition, where the upper crustal component tapers off and mafic/ultramafic material shoals as the segment end is approached (Figure 11a). This allows for the southern (missing) portion of hanging wall to have a denser composition than what is currently observed atop the northern two-thirds of the massif.

If the southern hanging wall material was mass wasted, perhaps during

uplift or flexure of the Southern Ridge, it may have disbursed throughout the local axial valley and the nodal basin. A lobe of material exists at the southeastern base of Atlantis Massif (Figure 1 at 30°05'N-30°10'N, 42°03'W) and the nodal basin, although deep, is smooth with several isolated large blocks of material at its northern edge. These features are consistent with a flow of mass wasted material. Alternatively, if the detachment fault rooted in the axial valley, it is possible that some of the hanging wall material was transferred to the conjugate flank of the spreading axis. Results from reflection analysis of MCS profile A8 on the outside corner suggest that the upper crustal section on the conjugate flank is thicker than normal (*Canales et al.*, 2004) by ∼250-500 m, supporting this conclusion.

Lithologic evidence also supports the hypothesis of a southeast dipping fault cutting into ultramafic host rock. A wedge shaped hanging wall cutting deeper into the lithospheric section at one end will expose deeper, more ultramafic material at that end when isostatically uplifted. This is a possible explanation for the higher volume of serpentinized mantle rocks found on the southern end and contributes to the overall lithospheric heterogeneity of Atlantis Massif.

Simple isostasy and alteration approximations are considered to test the credibility of the southeast dipping detachment fault hypothesis as it relates to the observed morphology and lithology of Atlantis Massif. *Lavier et al.* (1999), basing their model on the rolling hinge model of *Buck* (1988), predict 2600 m of footwall uplift for a detachment fault that has undergone ∼27 km of slip, similar to one estimate of slip proposed for Atlantis Massif (*Tucholke et al.*, 1998). We propose a combination of factors may all contribute to the >1 km of relative relief between the Southern Ridge and Central Dome: 1) greater isostatic forces acting where more overlying material has been removed from the Southern Ridge; 2) a possible spreading-parallel fault between Southern Ridge and Central Dome (e.g. *Karson et al.*, 2006) with some normal motion; and 3) expansion from increased degree of serpentinization of deeper, more olivine-rich material in the south. Gravity results show that the region of Atlantis Massif is not completely isostatically compensated (*Blackman et al.*, 1998, 2008), indicating that additional uplift may occur over time.

Spreading-parallel faulting was suggested by *Karson et al.* (2006) to have

occurred between a Southern Ridge of serpentinite composition and a gabbroic Central Dome. While our results indicate that the gabbroic lithology occurs in several portions of Atlantis Massif, it is possible that a spreading-parallel fault exists between these two morphologic components, perhaps between two discrete gabbroic bodies. Normal faulting of this orientation at the northern extreme of the Southern Ridge (e.g. 30°08.5'N) may provide a mechanism for increased uplift in the south. Assuming a fault of this orientation and location, and depending on the degree of coupling across the transform fault and the possible presence of transform-dipping faulting, an additional ∼650-1550 m of uplift may be achieved on the Southern Ridge (*Baines et al.*, 2003).

Likewise, a 20-30% volumetric expansion associated with the olivine to serpentinite reaction (per cent volumetric expansion determined for samples from Kane OCC) (*Karson and Lawrence*, 1997) may contribute to the increased uplift of the Southern Ridge. A fault cutting several kilometers deeper into the lithosphere on one side may bring seawater into contact with material of high olivine content. A rate of serpentinization of 1.4e-4 km^3/yr is determined for Atlantis Massif (*Früh-Green et al.*, 2003). Using this estimate for rate of serpentinization over the last 1.5 Ma, ∼210 km^3 of serpentinite would have been produced since Atlantis Massif initiated. This would contribute to a volumetric expansion of ∼42-63 km^3 during the history of Atlantis Massif, contributing to overall massif uplift, the majority of which would occur in the Southern Ridge where olivine content is highest due to the fault cutting deeper into the lithospheric section in this area. *O'Hanley* (1992) notes that a serpentinization-induced volumetric expansion of 25% leads to a linear expansion of 8%. This would contribute to ∼70 m increase in topography on the entire area of the Southern Ridge if we assume that all serpentinization occurs there. We conclude that the dipping detachment fault and isostatic uplift are the primary controls on the morphologic and lithologic structure of Atlantis Massif (Figure 11d).

2.5 Conclusion

Tomographic inversion of multichannel seismic data processed with the SOBE downward continuation technique allows for dense and detailed coverage of the upper ∼1.5 km of structure within the smooth, high-relief Atlantis Massif oceanic core complex and its conjugate crust. Independent constraints from rock samples and gravity modeling allow us to infer geologic structure from our tomographic models. The general consistency between rock sample type and the velocities obtained indicate that SOBE processed MCS data are an effective and valuable method for guiding geologic interpretation, by exposing shallow turning arrivals for picking and inclusion in the inversion process.

A broad range of velocity structure regimes is observed in our results and the lateral heterogeneity within the seismic structure is great. Values larger than 5.5 km/s occur just below the seafloor in some areas and are interpreted as gabbroic rock based on velocity, velocity gradient, gravity, and deep drilling results. This is consistent with inferences drawn by *Canales et al.* (2008). Much lower velocity packages, with velocity-depth profiles similar to those of young Atlantic crust (*Arnulf et al.*, 2011; *Arnulf*, 2011), are present in the models at lateral offsets as little as ∼1-2 km from the higher gabbroic velocities (line A9, 5.5 km/s to 2 km/s over 1.5 km). These lower velocities, termed here the IVVL, are interpreted as highly serpentinized periodite on the Southern Ridge based on groundtruth and the considerable difference in velocity structure between these velocities and the velocities of lines A5 and A8 (hanging wall and conjugate crust, respectively), which are of extrusive basaltic composition. The outward-facing slope on the west of the massif is interpreted to contain at least some crust of extrusive volcanics based on the correlation of 1D velocity structure with that of typical young Atlantic crust, the volcanic terrain imaged by Argo-II, and a gravity deficit. Vertical velocity gradients within the upper ∼1.5 km range from $<1\ s^{-1}$ to $>3\ s^{-1}$, contributing to the overall heterogeneity of the massif structure.

We infer that this oceanic core complex is composed of a dominantly gabbroic core, with a likely persisting sheath of serpentinized peridotite in some areas, and volcanic material on the eastern OCC flank and outward-facing slope. This

interpretation is most consistent with the model proposed by *Ildefonse et al.* (2007) of a pluton emplaced in a peridotite host rock, followed by sea water alteration and strain localization within the peridotite causing detachment fault formation and slip, leading to an OCC with a mafic core surrounded by serpentinite. The presence of low velocities representative of volcanics on the outward-facing slope near the breakaway is consistent with a tilted basaltic ridge that emerges at the onset of OCC formation (*Smith et al.*, 2006), while the low-velocity volcanic material on the eastern ridge flank is a remnant of the once overlying hanging wall.

The gabbroic composition of the core of Atlantis Massif indicates that magmatism was active to some extent during OCC formation. Based on the shape of the plutonic core inferred from our models, we hypothesize that a southward propagating magmatic source is responsible for emplacement and has created a curved gabbroic body(ies). Based on the 30-50% magmatic emplacement to tectonic extension ratio (*Buck et al.*, 2005; *Tucholke et al.*, 2008; *Olive et al.*, 2010) predicted for the initiation of a detachment fault and the strain localization model of *Ildefonse et al.* (2007), it follows that a southeast dipping detachment fault may have formed above the upper edge of the gabbroic pluton as the source traveled along axis. A fault with this orientation, cutting deeply into the ultramafic lithosphere in the south, is consistent with both the morphology and lithology of the present day Atlantis Massif.

Acknowledgments

The authors would like to offer sincere thanks to associate editor M. Cheadle, reviewer H. Van Avendonk, and an anonymous reviewer for comments and suggestions that greatly improved the paper. We also appreciate the use of the Generic Mapping Tools (GMT) program (*Wessel and Smith*, 1991). NSF support was provided via grant OCE-0927442.

Chapter 2, in full, is a reprint of the material as it appears in Henig, A. S., D. K. Blackman, A. J. Harding, J.-P. Canales, and G. M. Kent (2012), Downward continued multichannel seismic refraction analysis of Atlantis Massif oceanic core complex, 30°N, Mid-Atlantic Ridge, *Geochemistry Geophysics Geosystems, 13*, Q0AG07, doi:10.1029/2012GC004059. The dissertation author was the primary investigator and author of this paper.

References

Allerton, S., J. Escartín, and R. Searle (2000), Extremely asymmetric magmatic accretion of oceanic crust at the ends of slow-spreading ridge segments, *Geology*, *28*(2), 179, doi:10.1130/0091-7613(2000)?28¡179:EAMAOO¿?2.0.CO;2.

Arnulf, A., S. Singh, A. Harding, G. Kent, and W. Crawford (2011), Strong seismic heterogeneity in layer 2a near hydrothermal vents at the mid-atlantic ridge, *Geophysical Research Letters*, *38*(13), L13,320, doi:10.1029/2011GL047753.

Arnulf, A., (2011), Layer 2A structure beneath the Lucky Strike volcano, Mid-Atlantic Ridge, from high-resolution tomography and full waveform inversion, *Institut Physique du Globe de Paris, Paris, France*

Arnulf, A. F., A. J. Harding, S. C. Singh, G. M. Kent, and W. Crawford (2012, in prep.), Constraints on the shallow velocity structure of the lucky-strike volcano, mid-atlantic ridge, from downward continued multi-channel streamer data.

Baines, A., M. Cheadle, H. Dick, A. Scheirer, B. John, N. Kusznir, and T. Matsumoto (2003), Mechanism for generating the anomalous uplift of oceanic core complexes: Atlantis bank, southwest indian ridge, *Geology*, *31*(12), 1105–1108, doi:10.1130/G19829.1.

Blackman, D., and J. Collins (2010), Lower crustal variability and the crust/mantle transition at the atlantis massif oceanic core complex, *Geophysical Research Letters*, *37*, L24,303, doi:10.1029/2010GL045165.

Blackman, D., J. Cann, B. Janssen, and D. Smith (1998), Origin of extensional core complexes: evidence from the mid-atlantic ridge at atlantis fracture zone, *Journal of Geophysical Research*, *103*(B9), 21,315–21,333, doi:10.1029/98JB01756.

Blackman, D. K., J. A. Karson, D. S. Kelley, J. R. Cann, G. L. Früh-Green, J. S. Gee, S. D. Hurt, B. E. John, J. Morgan, S. L. Nooner, D. K. Ross, T. J. Schroeder, and E. A. Williams (2002), Geology of the atlantis massif (mid-atlantic ridge, 30 n): Implications for the evolution of an ultramafic oceanic core complex, *Marine Geophysical Researches*, *23*(5), 443–469, doi:10.1023/B:MARI.0000018232.14085.75.

Blackman, D., B. Ildefonse, B. John, Y. Ohara, D. Miller, and C. MacLeod (2006), Expedition 304/305 scientists, in *Proceedings of the Integrated Ocean Drilling Program*, vol. 304/305, doi:10.2204/iodp.sp.304305.2005.

Blackman, D., G. Karner, and R. Searle (2008), Three-dimensional structure of oceanic core complexes: Effects on gravity signature and ridge flank morphology, mid-atlantic ridge, 30°n, *Geochemistry Geophysics Geosystems*, *9*(6), Q06,007, doi:10.1029/2008GC001951.

Blackman, D., B. Ildefonse, B. E. John, Y. Ohara, D. J. Miller, N. Abe, M. Abratis, E. S. Andal, M. Andreani, S. Awaji, J. S. Beard, D. Brunelli, A. B. Charney, D. M. Christie, J. Collins, A. G. Delacour, H. Delius, M. Drouin, F. Einaudi, J. Escartn, B. R. Frost, G. Früh-Green, P. B. Fryer, J. S. Gee, M. Godard, C. B. Grimes, A. Halfpenny, H.-E. Hansen, A. C. Harris, A. Tamura, N. W. Hayman, E. Hellebrand, T. Hirose, J. G. Hirth, S. Ishimaru, K. T. M. Johnson, G. D. Karner, M. Linek, C. J. MacLeod, J. Maeda, O. U. Mason, A. M. McCaig, K. Michibayashi, A. Morris, T. Nakagawa, T. Nozaka, M. Rosner, R. C. Searle, G. Suhr, M. Tominaga, A. von der Handt, T. Yamasaki, X. Zhao (2011), Drilling constraints on lithospheric accretion and evolution at atlantis massif, mid-atlantic ridge 30°n, *Journal of Geophysical Research*, *116*(B7), B07,103.

Boschi, C., G. Früh-Green, A. Delacour, J. Karson, and D. Kelley (2006), Mass transfer and fluid flow during detachment faulting and development of an oceanic core complex, atlantis massif (mar 30°n), *Geochem. Geophys. Geosyst*, *7*(1), Q01,004, doi:10.1029/2005GC001074.

Buck, W. (1988), Flexural rotation of normal faults, *Tectonics*, *7*(5), 959–973, doi:10.1029/TC007i005p00959.

Buck, W., L. Lavier, and A. Poliakov (2005), Modes of faulting at mid-ocean ridges, *Nature*, *434*(7034), 719–723, doi:10.1038/nature03358.

Canales, J., R. Detrick, J. Lin, J. Collins, and D. Toomey (2000a), Crustal and upper mantle seismic structure beneath the rift mountains and across a non-transform offset at the mid-atlantic ridge (35°n), *Journal of geophysical research*, *105*(B2), 2699–2719, doi:10.1029/1999JB900379.

Canales, J., J. Collins, J. Escartín, and R. Detrick (2000b), Seismic structure across the rift valley of the mid-atlantic ridge at 23°20' n (mark area): Implications for crustal accretion processes at slow spreading ridges, *Journal of Geophysical Research*, *105*(B12), 28,411–28,425, doi:10.1029/2000JB900301.

Canales, J., B. Tucholke, and J. Collins (2004), Seismic reflection imaging of an oceanic detachment fault: Atlantis megamullion (mid-atlantic ridge, 30°10'n), *Earth and Planetary Science Letters*, *222*(2), 543–560, doi: 10.1016/j.epsl.2004.02.023.

Canales, J., R. Detrick, S. Carbotte, G. Kent, J. Diebold, A. Harding, J. Babcock, M. Nedimovic, and E. Van Ark (2005), Upper crustal structure and axial topography at intermediate spreading ridges: Seismic constraints from the southern juan de fuca ridge, *J. Geophys. Res*, *110*, B12,104, doi:10.1029/2005JB003630.

Canales, J., B. Tucholke, M. Xu, J. Collins, and D. DuBois (2008), Seismic evidence for large-scale compositional heterogeneity of oceanic core complexes, *Geochemistry Geophysics Geosystems*, *9*(8), Q08,002, doi:10.1029/2008GC002009.

Cann, J., D. Blackman, D. Smith, E. McAllister, B. Janssen, S. Mello, E. Avgerinos, A. Pascoe, and J. Escartin (1997), Corrugated slip surfaces formed at ridge-transform intersections on the mid-atlantic ridge, *Nature*, *385*(6614), 329–332, doi:10.1038/385329a0.

Cannat, M. (1993), Emplacement of mantle rocks in the seafloor at mid-ocean ridges, *Journal of Geophysical Research*, *98*(B3), 4163–4172, doi:10.1029/92JB02221.

Cannat, M., D. Sauter, V. Mendel, E. Ruellan, K. Okino, J. Escartin, V. Combier, and M. Baala (2006), Modes of seafloor generation at a melt-poor ultraslow-spreading ridge, *Geology*, *34*(7), 605–608, doi:10.1130/G22486.1.

Christeson, G., G. Purdy, and G. Fryer (1994), Seismic constraints on shallow crustal emplacement processes at the fast spreading east pacific rise, *Journal of geophysical research*, *99*(B9), 17,957–17,973, doi:10.1029/94JB01252.

Collins, J., D. Blackman, A. Harris, and R. Carlson (2009), Seismic and drilling constraints on velocity structure and reflectivity near IODP Hole U1309D on the central dome of Atlantis Massif, Mid-Atlantic Ridge 30 N, *Geochem. Geophys. Geosyst*, *10*(Q01010) doi:10.1029/2008GC002121.

Detrick, R., H. Needham, and V. Renard (1995), Gravity anomalies and crustal thickness variations along the mid-atlantic ridge between 33°n and 40°n, *Journal of geophysical research*, *100*(B3), 3767–3787, doi:10.1029/94JB02649.

Dick, H., J. H. Natland, J. C. Alt, W. Bach, D. Bideau, J. S. Gee, S. Haggas, J. G. H. Hertogen, G. Hirth, P. M. Holm, B. Ildefonse, G. J. Iturrino, B. E. John, D. S. Kelley, E. Kikawa, A. Kingdon, P. J. LeRoux, J. Maeda, P. S. Meyer, D. J. Miller, H. R. Naslund, Y.-L. Niu, P. T. Robinson, J. Snow, R. A. Stephen, P. W. Trimby, H.-U. Worm, and A. Yoshinobu (2000), A long in situ section of the lower ocean crust: results of odp leg 176 drilling at the southwest indian ridge, *Earth and planetary science letters*, *179*(1), 31–51, doi:10.1016/S0012-821X(00)00102-3.

Dick, H., et al. (2002), Primary silicate mineral chemistry of a 1.5-km section of very slow spreading lower ocean crust: Odp hole 735b, southwest indian ridge, in *Proc. ODP, Sci. Results*, vol. 176, pp. 1–61, doi:10.2973/odp.proc.sr.176.001.2002.

Dick, H., M. Tivey, and B. Tucholke (2008), Plutonic foundation of a slow-spreading ridge segment: Oceanic core complex at kane megamullion, 23°30' n, 45°20' w, *Geochemistry Geophysics Geosystems*, *9*(5), Q05,014, doi:10.1029/2007GC001645.

Escartín, J., C. Mével, C. MacLeod, and A. McCaig (2003), Constraints on deformation conditions and the origin of oceanic detachments: The mid-atlantic ridge core complex at 15 45°n, *Geochem. Geophys. Geosyst*, *4*(8), 1067, doi: 10.1029/2002GC000472.

Escartín, J., D. Smith, J. Cann, H. Schouten, C. Langmuir, and S. Escrig (2008), Central role of detachment faults in accretion of slow-spreading oceanic lithosphere, *Nature*, *455*, 790–794, doi:10.1038/nature07333.

Früh-Green, G., D. Kelley, S. Bernasconi, J. Karson, K. Ludwig, D. Butterfield, C. Boschi, and G. Proskurowski (2003), 30,000 years of hydrothermal activity at the lost city vent field, *Science*, *301*(5632), 495–498, doi: 10.1126/science.1085582.

Grimes, C., B. John, M. Cheadle, and J. Wooden (2008), Protracted construction of gabbroic crust at a slow spreading ridge: Constraints from 206pb/238u zircon ages from atlantis massif and iodp hole u1309d (30 n, mar), *Geochemistry Geophysics Geosystems*, *9*(8), Q08,012, doi:10.1029/2008GC002063.

Harding, A., G. Kent, and J. Orcutt (1993), A multichannel seismic investigation of upper crustal structure at 9°n on the east pacific rise: Implications for crustal accretion, *Journal of geophysical research*, *98*(B8), 13,925–13,944, doi: 10.1029/93JB00886.

Harding, A., G. Kent, D. Blackman, S. Singh, and J. Canales (2007), A new method for mcs refraction data analysis of the uppermost section at a mid-atlantic ridge core complex, in *Eos, Trans. Am. Geophys. Union*, vol. 88, pp. S12A–03 (Abstract).

Hooft, E., R. Detrick, D. Toomey, J. Collins, and J. Lin (2000), Crustal thickness and structure along three contrasting spreading segments of the mid-atlantic ridge, 33.5–35°n, *Journal of geophysical research*, *105*(B4), 8205–8226, doi: 10.1029/95JB02502.

Hussenoeder, S., G. Kent, and R. Detrick (2002), Upper crustal seismic structure of the slow spreading mid-atlantic ridge, 35°n: Constraints on volcanic emplacement processes, *J. geophys. Res*, *107*(B8), 2156, doi:10.1029/2001JB001691.

Ildefonse, B., D. Blackman, B. John, Y. Ohara, D. Miller, C. MacLeod, and Integrated Ocean Drilling Program Expeditions 304/305 Science Party. (2007), Oceanic core complexes and crustal accretion at slow-spreading ridges, *Geology*, *35*(7), 623–626, doi:10.1130/G23531A.1.

John, B., M. Cheadle, J. Gee, C. Grimes, A. Morris, and N. Pressling (2009), Data report: Spatial and temporal evolution of slow spread oceanic crustgraphic sections of core recovered from iodp hole u1309d, atlantis massif, 30°n, mar

(including pb/u zircon geochronology and magnetic remanence data), *304*, 305, doi:10.2204/iodp.proc.304305.205.2009.

Karson, J. (1999), Geological investigation of a lineated massif at the kane transform fault: implications for oceanic core complexes, *Phil. Trans. R. Soc. Lond. A*, *357*(1753), 713–740, doi:10.1098/rsta.1999.0350.

Karson, J., and R. Lawrence (1997), Tectonic setting of serpentinite exposures on the western median valley wall of the mark area in the vicinity of site 920, *Proceedings of the Ocean Drilling Program*, *153*, 5–22, doi: 10.2973/odp.proc.sr.153.001.1997.

Karson, J., G. Früh-Green, D. Kelley, E. Williams, D. Yoerger, and M. Jakuba (2006), Detachment shear zone of the atlantis massif core complex, mid-atlantic ridge, 30°n, *Geochemistry Geophysics Geosystems*, *7*(6), Q06,016, doi: 10.1029/2005GC001109.

Kelemen, P., E. Kikawa, D. Miller, and S. scientific party (2004), Leg 209 summary, in *Proceedings of the Ocean Drilling Program, Initial Reports*, vol. 209, doi: 10.2973/odp.proc.sr.153.001.1997.

Kelley, D.S., J.A. Karson, D.K. Blackman, G.L. Früh-Green, D.A. Butterfield, M.D. Lilley, E.J. Olson, M.O. Schrenk, K.K. Roe, G.T. Lebon (2001), An off-axis hydrothermal vent field near the Mid-Atlantic Ridge at 30 N, *Nature*, *412*(6843), 145–149, doi:10.1038/35084000.

Kelley, D., J. A. Karson, G. L. Früh-Green, D. R. Yoerger, T. M. Shank, D. A. Butterfield, J. M. Hayes, M. O. Schrenk, E. J. Olson, G. Proskurowski, M. Jakuba, A. Bradley, B. Larson, K. Ludwig, D. Glickson, K. Buckman, A. S. Bradley, W. J. Brazelton, K. Roe, M. J. Elend, A. Delacour, S. M. Bernasconi, M. D. Lilley, J. A. Baross, R. E. Summons, and S. P. Sylva (2005), A serpentinite-hosted ecosystem: the lost city hydrothermal field, *Science*, *307*(5714), 1428–1434, doi:10.1126/science.1102556.

Kuo, B., and D. Forsyth (1988), Gravity anomalies of the ridge-transform system in the south atlantic between 31 and 34.5°s: Upwelling centers and variations in crustal thickness, *Marine Geophysical Research*, *10*(3-4), 205–232, doi: 10.1007/BF00310065.

Lavier, L., W. Roger Buck, and A. Poliakov (1999), Self-consistent rolling-hinge model for the evolution of large-offset low-angle normal faults, *Geology*, *27*(12), 1127–1130, doi:10.1130/0091-7613(1999)?027¡1127:SCRHMF¿?2.3.CO;2.

Lin, J., G. Purdy, H. Schouten, J. Sempere, and C. Zervas (1990), Evidence from gravity data for focused magmatic accretion along the mid-atlantic ridge, *Nature*, *344*(6267), 627–632, doi:10.1038/344627a0.

MacLeod, C., J. Escartn, D. Banerji, G.J. Banks, M. Gleeson, D.H.B. Irving, R.M. Lilly, A.M. McCaig, Y. Niu, S. Allerton and D.K. Smith (2002), Direct geological evidence for oceanic detachment faulting: The mid-atlantic ridge, 15°45' n, *Geology*, *30*(10), 879–882, doi:10.1130/0091-7613(2002)?030¡0879:DGEFOD¿?2.0.CO;2.

MacLeod, C., R. Searle, B. Murton, J. Casey, C. Mallows, S. Unsworth, K. Achenbach, and M. Harris (2009), Life cycle of oceanic core complexes, *Earth and Planetary Science Letters*, *287*(3-4), 333–344, doi:10.1016/j.epsl.2009.08.016.

McCaig, A., A. Delacour, A. Fallick, T. Castelain, and G. Fruh-Green (2010), Detachment fault control on hydrothermal circulation systems: interpreting the subsurface beneath the tag hydrothermal field using the isotopic and geological evolution of oceanic core complexes in the atlantic, *Diversity of Hydrothermal Systems on Slow Spreading Ocean Ridges, Geophys. Monogr. Ser.*, *188*, 207–240.

Michael, P., D. W. Forsyth, D. K. Blackman, P. J. Fox, B. B. Hanan, A. J. Harding, K. C. Macdonald, G. A. Neumann, J. A. Orcutt, M. Tolstoy, and C. M. Weiland. (1994), Mantle control of a dynamically evolving spreading center: Mid-atlantic ridge 31-34 s, *Earth and planetary science letters*, *121*(3-4), 451–468, doi:10.1016/0012-821X(94)90083-3.

Miller, D., and N. Christensen (1997), Seismic velocities of lower crustal and upper mantle rocks from the slow-spreading mid-atlantic ridge, south of the kane transform zone (mark), *Proceedings of the Ocean Drilling Program*, *153*, 437–454, doi:10.2973/odp.proc.sr.153.043.1997.

Morris, E., and R. Detrick (1991), Three-dimensional analysis of gravity anomalies in the mark area, mid-atlantic ridge 23° n, *Journal of Geophysical Research*, *96*(B3), 4355–4366, doi:10.1029/90JB02173.

Nozaka, T., and P. Fryer (2011), Alteration of the oceanic lower crust at a slow-spreading axis: insight from vein-related zoned halos in olivine gabbro from atlantis massif, mid-atlantic ridge, *Journal of Petrology*, *52*(4), 643–664, doi:10.1093/petrology/egq098.

O'Hanley, D. (1992), Solution to the volume problem in serpentinization, *Geology*, *20*(8), 705–708, doi:10.1130/0091-7613(1992)020¡0705:STTVPI¿2.3.CO;2.

Ohara, Y., T. Yoshida, Y. Kato, and S. Kasuga (2001), Giant megamullion in the parece vela backarc basin, *Marine Geophysical Research*, *22*(1), 47–61, doi:10.1023/A:1004818225642.

Okino, K., K. Matsuda, D. Christie, Y. Nogi, and K. Koizumi (2004), Development of oceanic detachment and asymmetric spreading at the australian-antarctic discordance, *Geochemistry, Geophysics, Geosystems*, *5*, Q12,012, doi:10.1029/2004GC00079.

Olive, J., M. Behn, and B. Tucholke (2010), The structure of oceanic core complexes controlled by the depth distribution of magma emplacement, *Nature Geoscience*, *3*(7), 491–495, doi:10.1038/NGEO888.

Penrose, C. P. (1973), Penrose field conference: Ophiolites, in *Geotimes*, vol. 17, pp. 24–26.

Planert, L., E. Flueh, and T. Reston (2009), Along-and across-axis variations in crustal thickness and structure at the mid-atlantic ridge at 5 s obtained from wide-angle seismic tomography: Implications for ridge segmentation, *Journal of Geophysical Research-Solid Earth*, *114*, B09,102, doi:10.1029/2008JB006103.

Reston, T., W. Weinrebe, I. Grevemeyer, E. Flueh, N. Mitchell, L. Kirstein, C. Kopp, H. Kopp, et al. (2002), A rifted inside corner massif on the mid-atlantic ridge at 5°s, *Earth and Planetary Science Letters*, *200*(3-4), 255–269, doi:10.1016/S0012-821X(02)00636-2.

Schroeder, T., and B. John (2004), Strain localization on an oceanic detachment fault system, atlantis massif, 30°n, mid-atlantic ridge, *Geochemistry Geophysics Geosystems*, *5*(11), Q11,007, doi:10.1029/2004GC000728.

Searle, R., M. Cannat, K. Fujioka, C. Mével, H. Fujimoto, A. Bralee, and L. Parson (2003), Fuji dome: A large detachment fault near 64 e on the very slow-spreading southwest indian ridge, *Geochem. Geophys. Geosyst*, *4*(8), 9105, doi:10.1029/2003GC000519.

Seher, T., W. Crawford, S. Singh, M. Cannat, V. Combier, and D. Dusunur (2010), Crustal velocity structure of the lucky strike segment of the mid-atlantic ridge at 37°n from seismic refraction measurements, *J. Geophys. Res*, *115*, B03,103, doi:10.1029/2009JB006650.

Sempéré, J., P. Blondel, A. Briais, T. Fujiwara, L. Géli, N. Isezaki, J.E. Pariso, L. Parson, P. Patriat, and C. Rommevauxg. (1995), The mid-atlantic ridge between 29 n and 31 30' n in the last 10 ma, *Earth and Planetary Science Letters*, *130*(1), 45–55.

Shtivelman, V., and A. Canning (1988), Datum correction by wave-equation extrapolation, *Geophysics*, *53*(10), 1311–1322, doi:10.1190/?1.1442409.

Smith, D., and J. Cann (1993), Building the crust at the mid-atlantic ridge, *Nature*, *365*(6448), 707–715, doi:10.1038/365707a0.

Smith, D., J. Cann, and J. Escartín (2006), Widespread active detachment faulting and core complex formation near 13°n on the mid-atlantic ridge, *Nature Letters*, *442*, 440–443, doi:10.1038/nature04950.

Smith, D., J. Escartín, H. Schouten, and J. Cann (2008), Fault rotation and core complex formation: Significant processes in seafloor formation at slow-spreading mid-ocean ridges (mid-atlantic ridge, 13-15°n), *Geochemistry, Geophysics, Geosystems*, *9*(3), Q03,003, doi:10.1029/2007GC001699.

Spudich, P., and J. Orcutt (1980), A new look at the seismic velocity structure of the oceanic crust, *Reviews of Geophysics*, *18*(3), 627–645, doi:10.1029/RG018i003p00627.

Tolstoy, M., A. Harding, and J. Orcutt (1993), Crustal thickness on the mid-atlantic ridge: Bull's-eye gravity anomalies and focused accretion, *Science*, *262*(5134), 726–729.

Tucholke, B., and J. Lin (1994), A geological model for the structure of ridge segments in slow spreading ocean crust, *Journal of Geophysical Research*, *99*(B6), 11,937–11,958, doi:10.1029/94JB00338.

Tucholke, B., J. Lin, and M. Kleinrock (1998), Megamullions and mullion structure defining oceanic metamorphic core complexes on the mid-atlantic ridge, *Journal of Geophysical Research*, *103*(B5), 9857–9866, doi:10.1029/98JB00167.

Tucholke, B., K. Fujioka, T. Ishihara, G. Hirth, and M. Kinoshita (2001), Submersible study of an oceanic megamullion in the central north atlantic, *Journal of Geophysical Research*, *106*(B8), 16,145–16,161, doi:10.1029/2001JB000373.

Tucholke, B., M. Behn, W. Buck, and J. Lin (2008), Role of melt supply in oceanic detachment faulting and formation of megamullions, *Geology*, *36*(6), 455–458, doi:10.1130/G24639A.1.

Van Avendonk, H., D. Shillington, W. Holbrook, and M. Hornbach (2004), Inferring crustal structure in the aleutian island arc from a sparse wide-angle seismic data set, *Geochemistry, Geophysics, Geosystems*, *5*, Q08,008, doi:10.1029/2003GC000664.

Wessel, P., and W. Smith (1991), Free software helps map and display data, *Eos Trans. AGU*, *72*(441), 445–446.

White, R., D. McKenzie, and R. O'Nions (1992), Oceanic crustal thickness from seismic measurements and rare earth element inversions, *Journal of Geophysical Research*, *97*(B13), 19,683–19,715, doi:10.1029/92JB01749.

Xu, M., J. Canales, B. Tucholke, and D. DuBois (2009), Heterogeneous seismic velocity structure of the upper lithosphere at kane oceanic core complex, mid-atlantic ridge, *Geochemistry, Geophysics, Geosystems*, *10*(10), Q10,001, doi:10.1029/2009GC002586.

Zelt, C., and P. Barton (1998), Three-dimensional seismic refraction tomography: A comparison of two methods applied to data from the faeroe basin, *Journal of Geophysical Research*, *103*(84), 7187–7210, doi:10.1029/97JB03536.

Zervas, C., J. Sempéré, and J. Lin (1995), Morphology and crustal structure of a small transform fault along the mid-atlantic ridge: the atlantis fracture zone, *Marine Geophysical Research*, *17*(3), 275–300, doi:10.1007/BF01203466.

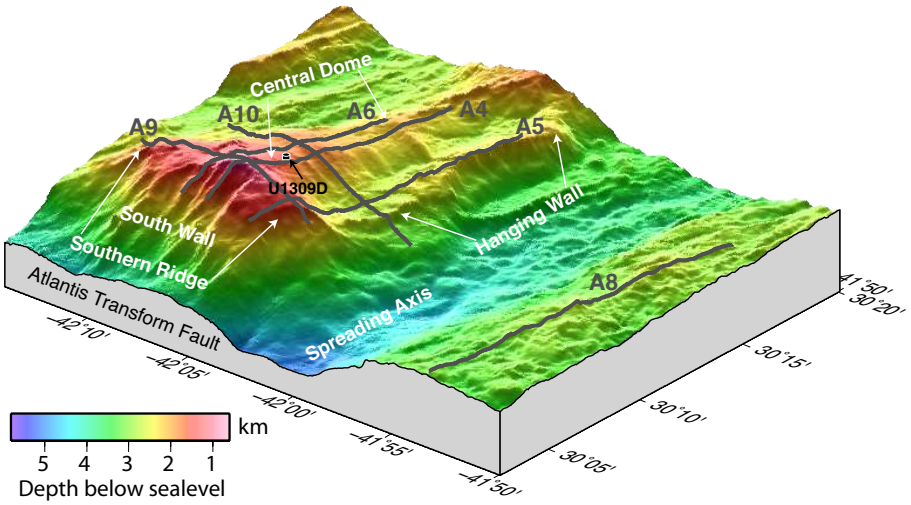

Figure 2.1: Perspective view of the Atlantis Massif looking to the northwest. Labels indicate the three main morphologic components and the South Wall. The Mid-Atlantic Ridge Axis and Atlantis Transform Fault are indicated. Gray lines and labels show location and extent of coverage for the six Multi-Channel Seismic lines in this study. The location of IODP Hole U1309D is shown by the black cylinder.

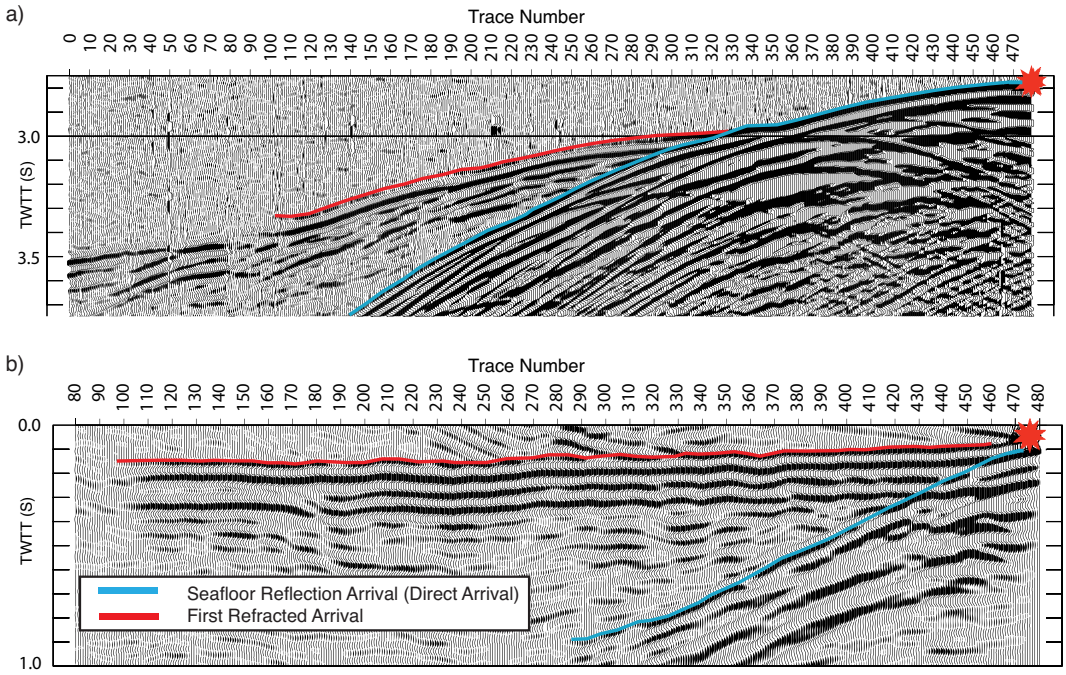

Figure 2.2: Representative shot gathers illustrating the result of the Synthetic On-Bottom Experiment downward continuation technique and plotted with a reduction velocity of 6.5 km/s. a) Initial shot gather before SOBE processing. b) SOBE processed shot gather showing collapse of seafloor reflection arrival and exposure of near-offset first refracted arrivals. Cyan marks seafloor reflection arrival; red marks first refracted arrival. Red stars indicate the end of the streamer closest to the source.

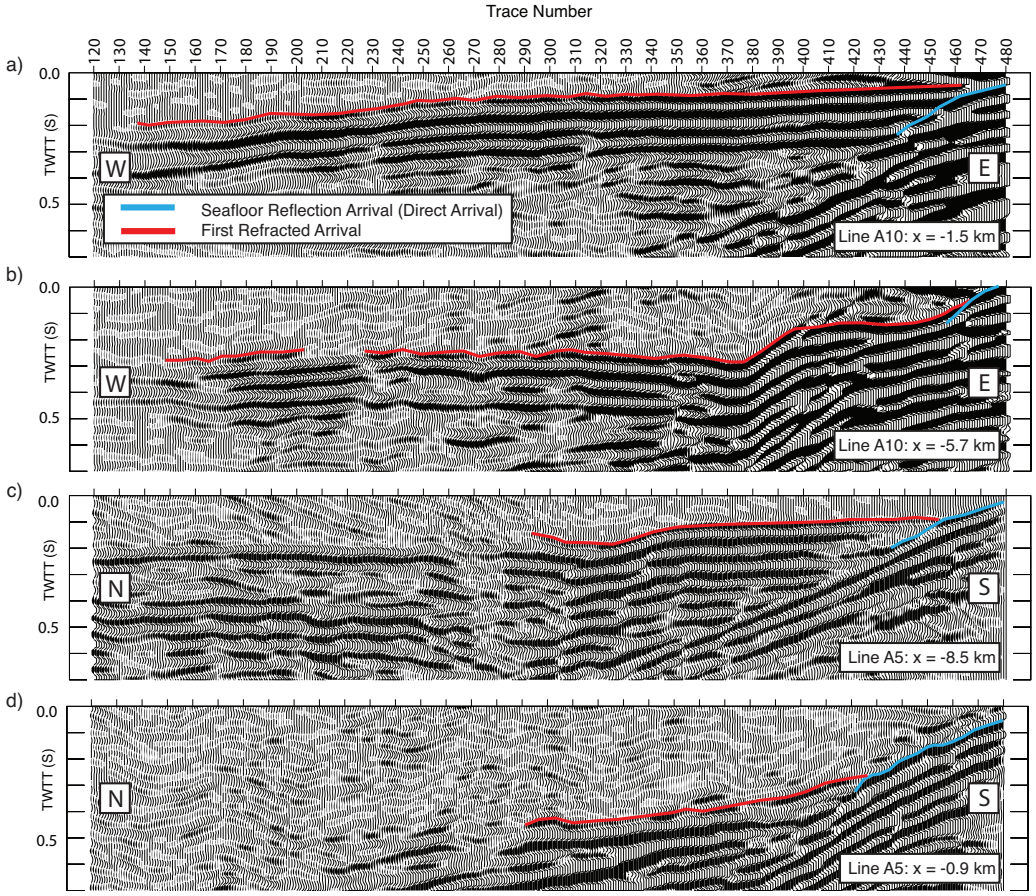

Figure 2.3: Representative shot gathers from the Atlantis Massif dataset showing a range of data quality. Trace number 480 is closest to the source. All shot gathers have been downward continued using SOBE. Shot gather locations are a) atop the Central Dome, b) on the Central Dome in an area of rapidly changing seismic structure, c) the transition from hanging wall to Southern Ridge where out of plane echoes may be causing destructive interference at long ranges, and d) atop the volcanic hanging wall in very rough topography. N, S, E, W indicate directions.

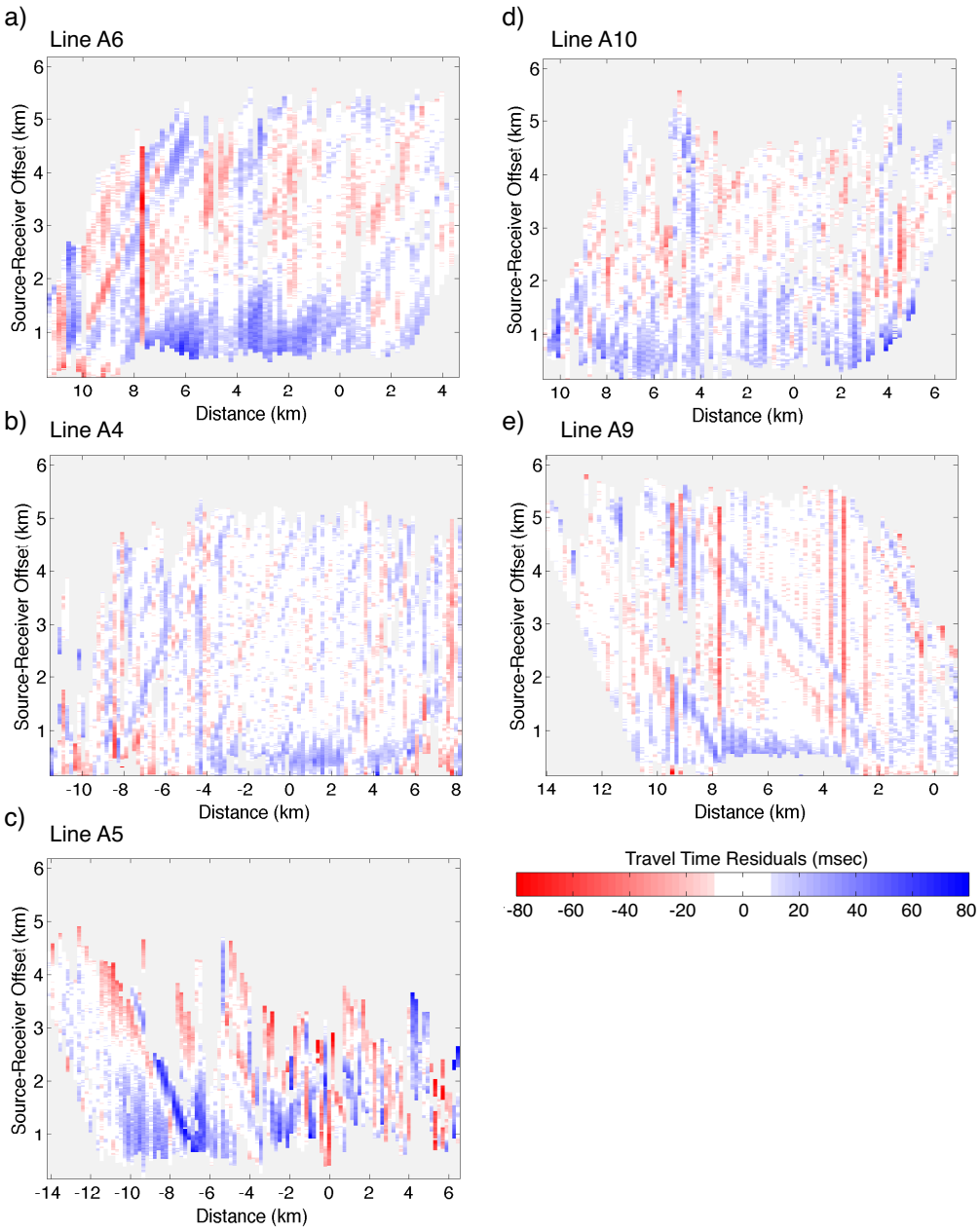

Figure 2.4: Travel Time residuals with respect to the preferred model (Figure 6) as a function of model distance and source-receiver range.

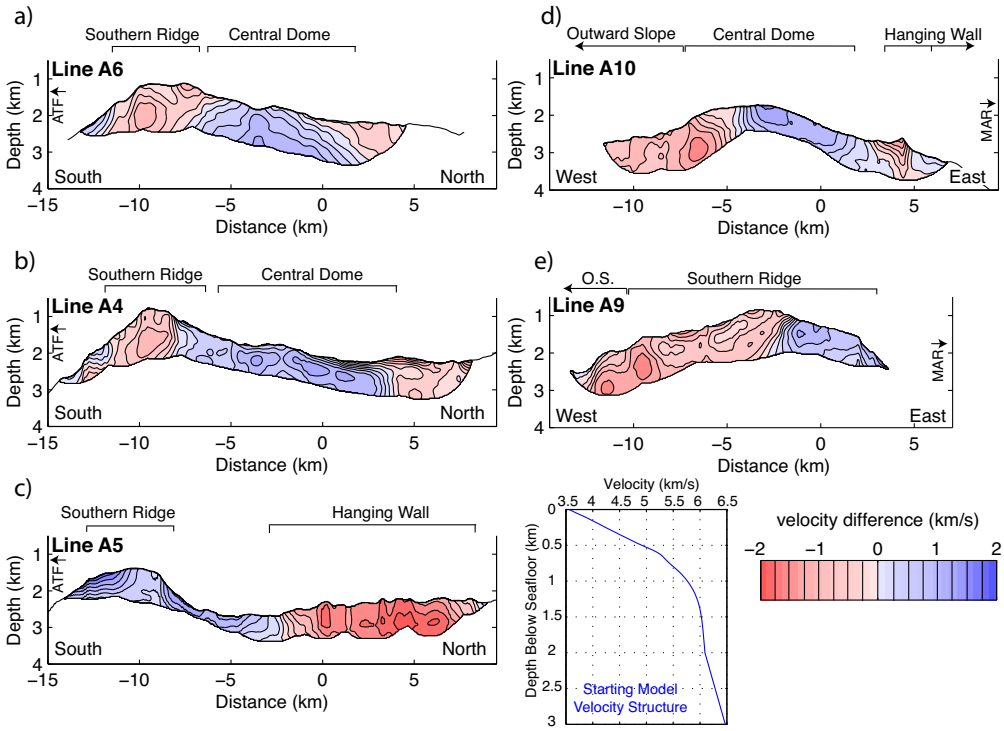

Figure 2.5: Difference between preferred and starting velocity models. Inset shows 1D starting model for all OCC lines. Contours are every 0.25 km/s.

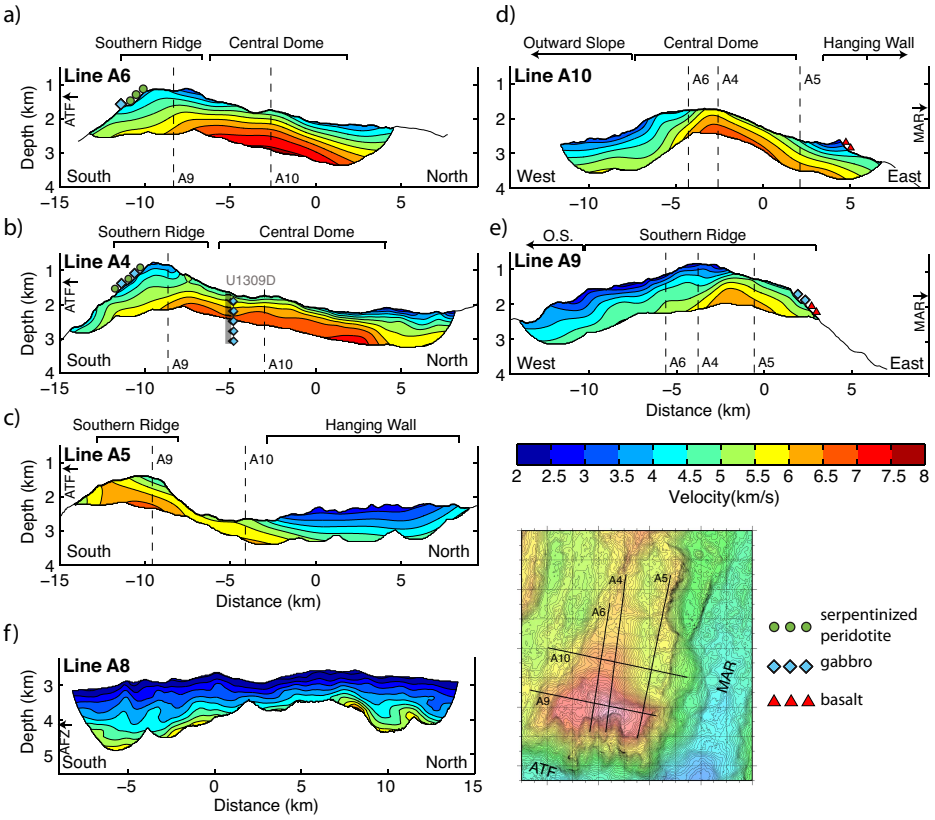

Figure 2.6: 2-D tomography models of P-wave velocity within Atlantis Massif (a-e) and its conjugate crust (f) depicted with 2:1 vertical exaggeration. Left panels show ridge-parallel lines and right panels show spreading-parallel lines. Line locations are shown in map view (inset) and major morphologic components are labeled at the top of each panel. Vertical dashed lines show locations of line crossings. Contour interval is 0.5 km/s. Green circles (Serpentinite), blue diamonds (Gabbro), and red triangles (Basalt) show the location of various rock types sampled from the massif surface or basement outcrops in submersible studies and drilling of IODP hole U1309D (vertical gray line projected onto line A4).

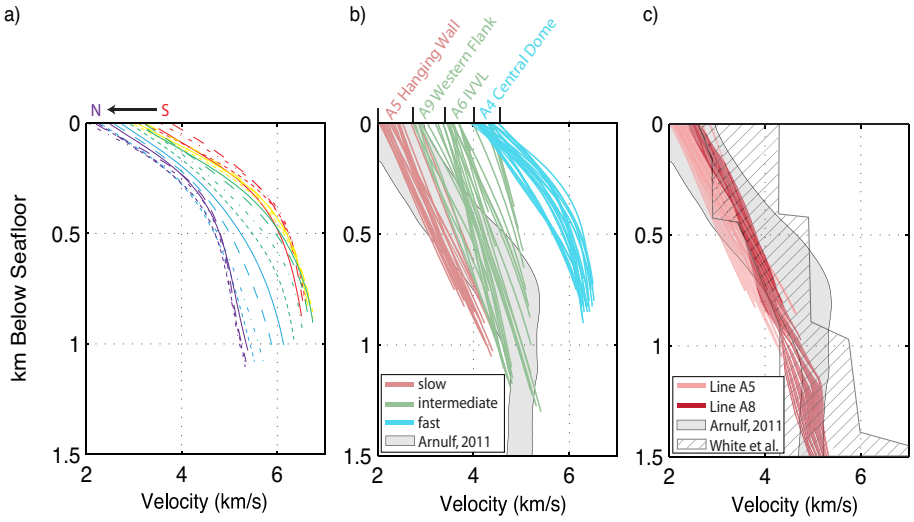

Figure 2.7: Velocity-depth profiles illustrating trends in velocities and velocity gradients within the models. a) 1D profiles from the central dome along line A4 (x=1-6 km) show that the highest velocity gradients occur within the upper ∼400 m. Velocity-depth profiles are shown every 250 m along line portion. b) Velocity-depth profiles showing the three velocity groupings determined from the models. Profiles come from various portions of the different lines and represent a sample every 250 m within the specified along-line range. The group of lowest seismic velocities (pink) range from 2-3 km/s to 4-4.5 km/s and were sampled between x=2-7 km on line A5 (hanging wall); the group of intermediate velocities range from 3-4.5 km/s to 4.75-5.5 km/s (green) and were sampled from x=-10 to -5 km on line A9 (western flank of massif) and from x=-13 to -9 km on line A6; and the group of highest velocities (blue) range from >4.5 km/s to 5.5-7 km/s at the top and base of the ray coverage, respectively, and were sampled between x=-4 to 1 km on line A4 (Central Dome). No clear pattern in velocity gradients can be distinguished among the groups. c) Comparison of velocity-depth profiles from line A5 hanging wall and line A8 on the low velocity, likely volcanic, conjugate crust with the velocity envelopes of the axial region of the Lucky Strike segment of the MAR (grey solid; *Arnulf et al.* (2011)) and young Atlantic crust aged 0-7 Ma (hatched; *White et al.* (1992)).

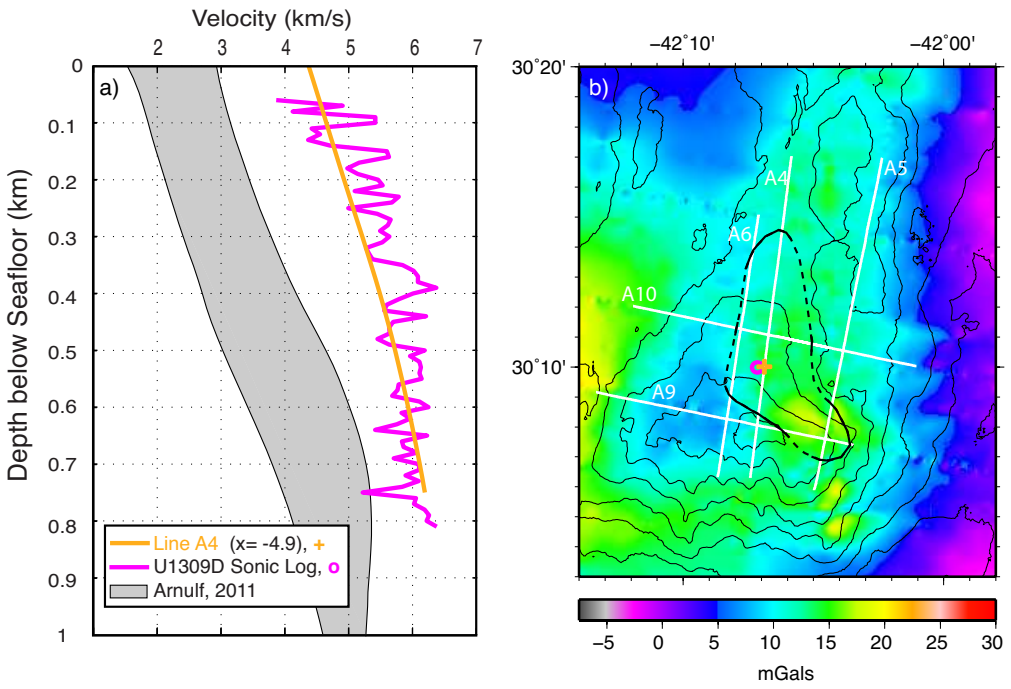

Figure 2.8: Representative vertical velocity profiles of a) High Velocity Body (HVB), and c) Intermediate-Valued Velocity Layer (IVVL). Gray shaded region is range of young Atlantic crustal velocities. Magenta curve is sonic log velocities at IODP Hole U1309D, 10 meter running average. b) Residual Bouguer gravity anomaly (topography, intracrustal interface, and lithospheric cooling corrections made) with surface projection of the lateral extent of the HVB. Solid outline indicates boundary of HVB based on the profiles, dashed outline indicates interpolation between profiles and is guided by gravity contours. Depth to HVB varies slightly within the region. Hole U1309D and location of A4 velocity profile in (a), are noted by magenta 'o' and orange '+' respectively. Thin black contours show seafloor depth at 500 m contour interval. d) Bathymetry with surface projection of the lateral extent of the IVVL. Grayshade increases with depth from shallowest contour (1000 m) with a 250 m contour interval. Colored '+'s show locations of profiles in (c). Projections in (b) and (d) are based on locations in models with 1D velocity structure characteristic of these regimes. Figure continued on following page.

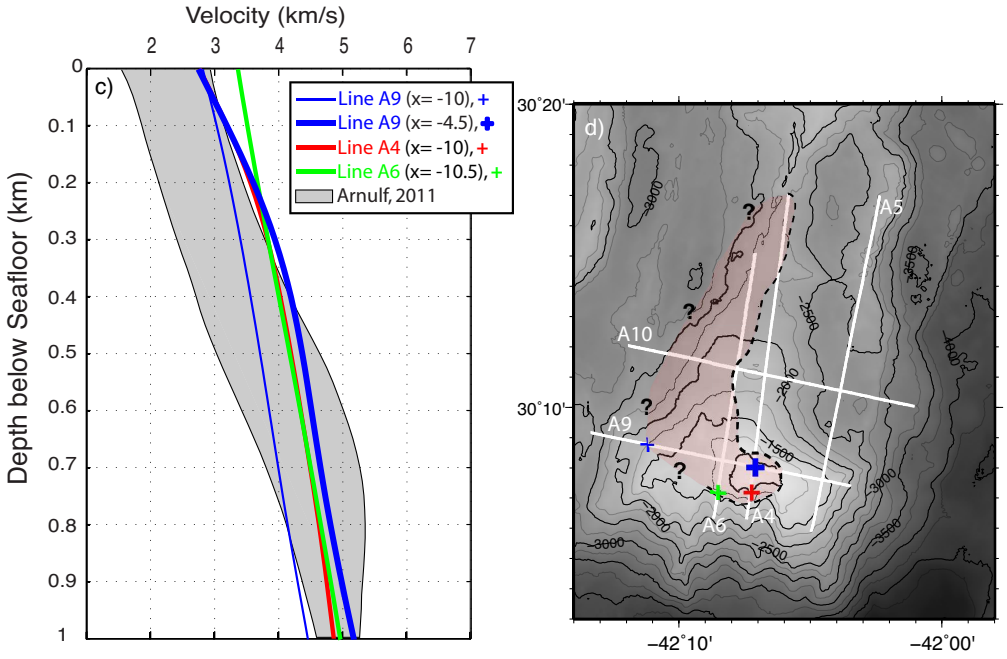

Figure 2.8: Figure continued from previous page. Representative vertical velocity profiles of a) High Velocity Body (HVB), and c) Intermediate-Valued Velocity Layer (IVVL). Gray shaded region is range of young Atlantic crustal velocities. Magenta curve is sonic log velocities at IODP Hole U1309D, 10 meter running average. b) Residual Bouguer gravity anomaly (topography, intracrustal interface, and lithospheric cooling corrections made) with surface projection of the lateral extent of the HVB. Solid outline indicates boundary of HVB based on the profiles, dashed outline indicates interpolation between profiles and is guided by gravity contours. Depth to HVB varies slightly within the region. Hole U1309D and location of A4 velocity profile in (a), are noted by magenta 'o' and orange '+' respectively. Thin black contours show seafloor depth at 500 m contour interval. d) Bathymetry with surface projection of the lateral extent of the IVVL. Grayshade increases with depth from shallowest contour (1000 m) with a 250 m contour interval. Colored '+'s show locations of profiles in (c). Projections in (b) and (d) are based on locations in models with 1D velocity structure characteristic of these regimes.

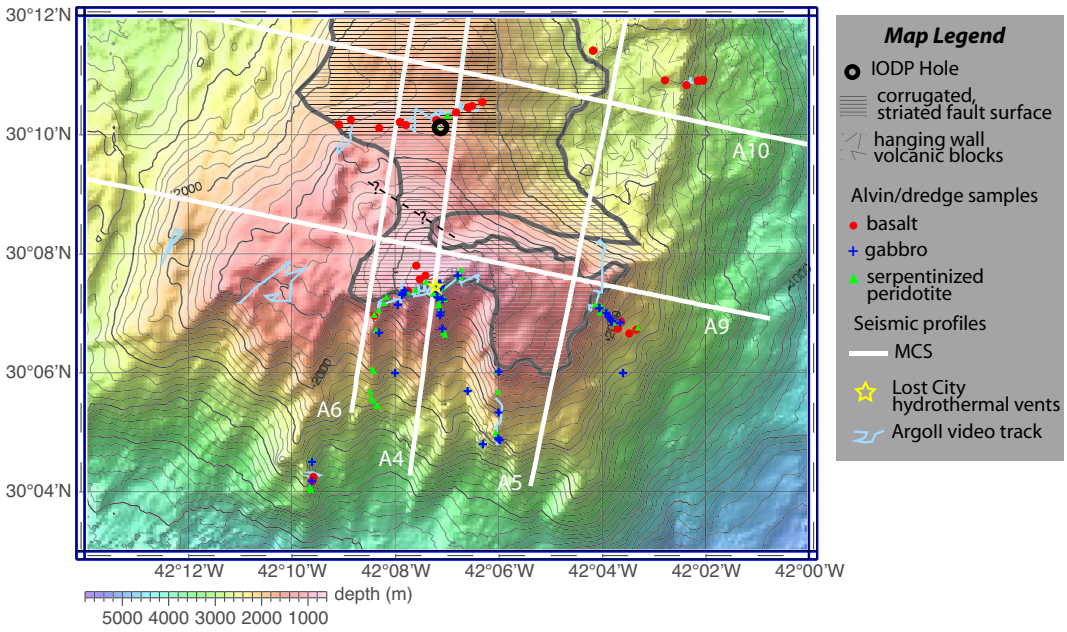

Figure 2.9: Map view of Atlantis Massif showing extent of corrugations, IODP Hole 1309D, sample lithology, and MCS lines. Dashed black line represents subsurface location of possible boundary between Central Dome and Southern Ridge as described in section 4.5. Modified from *Blackman et al.* (2011).

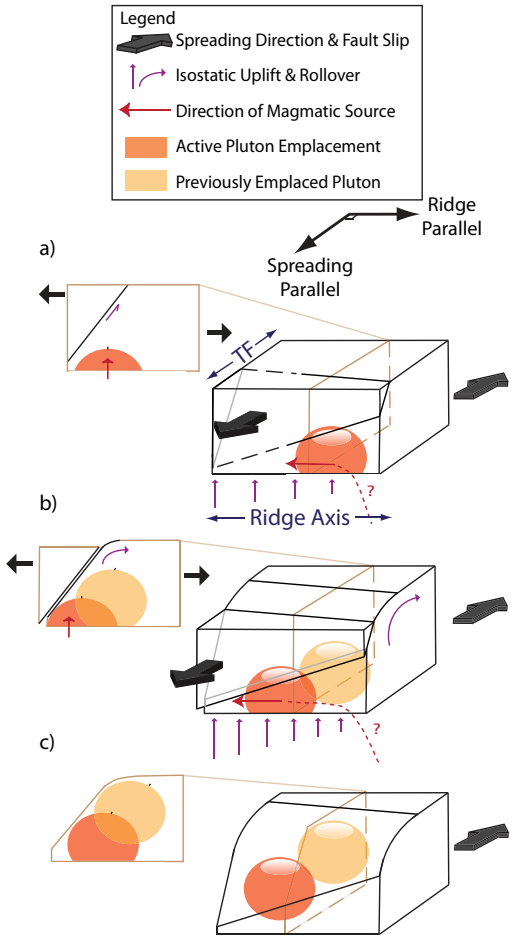

Figure 2.10: Block diagrams and cross-sections illustrating the emplacement history of the plutonic core of Atlantis Massif. a) Magmatic injection initiates at the north end of the current extent of Atlantis Massif. Strain localizes at the margin of the resultant pluton forming a detachment fault in the north. b) As the first area of injection is rafted off axis by spreading, the injection source and detachment fault propagate to the south. Isostatic forces are greater in the south due to the southeast dip of the detachment fault. c) The final geometry of the plutonic core seen at present day Atlantis Massif.

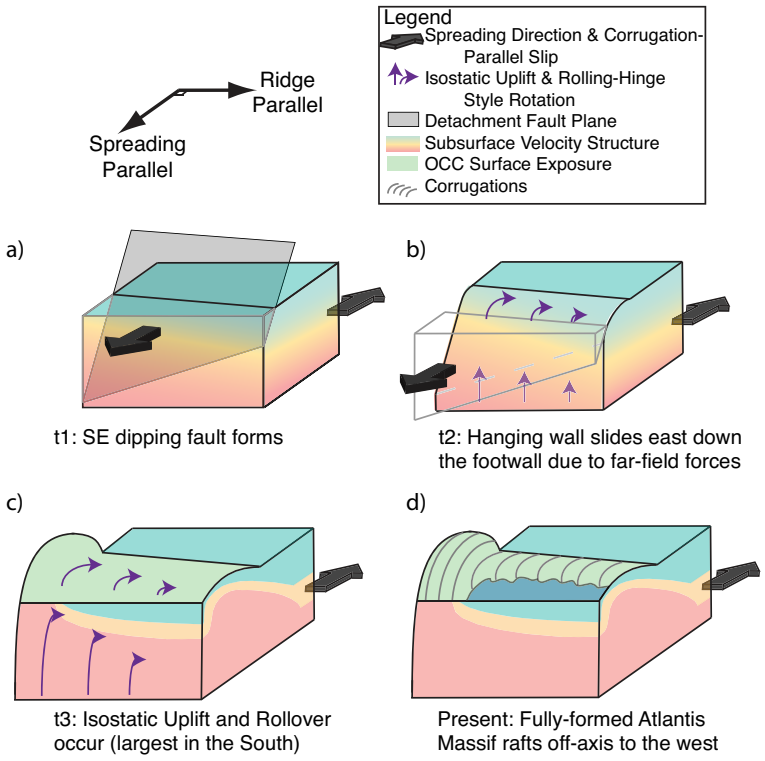

Figure 2.11: Sketch of faulting and uplift model. a) At time t1: a southeast dipping detachment fault forms, creating a wedge-shaped hanging wall. b) At time t2: the hanging wall slips down the footwall causing footwall uplift and a gradient in isostatic forces due to the uneven unloading of the footwall. c) At time t3: Uplift of the footwall is greater in the south than in the north. d) Present: present morphology of Atlantis Massif.

Chapter 3

Three-Dimensional Inversion of Downward Continued Multi-Channel Seismic Refraction Data at Atlantis Massif Oceanic Core Complex, 30°N Mid-Atlantic Ridge

3.1 Introduction

At Atlantis Massif Oceanic Core Complex (OCC) travel time tomography of downward continued multi-channel seismic (MCS) refraction p-wave first arrivals can provide dense, high-resolution coverage of the upper ∼1.5 km of the oceanic lithosphere. Individual 2D seismic velocity profiles are obtained by inverting first arrival travel times for a given seismic line independent of influence from nearby or crossing profiles (Henig et al., 2012). While this technique results in the best-fitting individual seismic profiles with the lowest travel time residuals, 1D velocity-depth profiles of the line-crossings may be discrepant (figure 1) and the effects of

surrounding structure and out of plane ray paths are ignored. In this case, the rays are restricted to travel through a 2D plane in x and z.

Interpretation of the 2D seismic velocity models (Canales et al., 2008; Henig et al., 2012) and comparison of velocity structure to a suite of existing data types, including rock samples from drilling (Blackman et al., 2006) and submersible studies (Blackman et al., 2002), indicates that Atlantis Massif consists of a gabbroic core in the central and southeast regions, surrounded in the south and southwest by a thick sheath of serpentinized peridotite. Extrusive volcanic hanging wall material sits atop the northeastern two-thirds of the massif (figure 2) and also likely on the outward-facing slope marking the transition into a layer-cake crustal structure (Henig et al., 2012).

In this study, we perform a 3D tomographic inversion of the five OCC MCS lines discussed above in order to reconcile line crossings and to allow for the influence of seismic rays that are not constricted to a 2D plane to guide the models. Significant deviations from the 2D models are not expected as additional influence from intersecting lines derives mainly from perpendicular rays in narrow regions.

3.2 Geographic Locations of Seismic Lines

Atlantis Massif OCC, at 30°N on the Mid-Atlantic Ridge (MAR), is surveyed by three ridge-subparallel and two ridge-perpendicular MCS lines that intersect on the Southern Ridge and Central Dome of the massif (figure 2). Because Atlantis Massif is large and widespread coverage of the area was the goal of the seismic data acquisition survey, the seismic lines are spaced several kilometers apart. This spacing is not close enough for an ideal 3D seismic survey where the scale of expected structure is greater than the profile spacing, but nonetheless structure at the line crossings and within several hundred meters perpendicular to and out of plane for each line can be assessed from a 3D inversion.

3.3 Methods

Because the 2D inversions (Henig et al., 2012) are completed in a local reference frame for each line, where the x-direction is defined along the length of the line and the y-direction is set to zero, it is necessary to convert all of the lines into a global coordinate system before performing a 3D inversion. To accomplish this, first the origin for the global coordinate system was chosen as the latitude and longitude of IODP Drill Hole U1309D (Blackman et al., 2006), and assigned global (x_g,y_g) coordinates of (0,0). Using latitude and longitude of the local origin of each line, the global origin for each line was determined (table 1). The azimuth of each line was calculated from the first and last shot of the line using the Matlab azimuth function (table 1). Shot positions and receiver positions from each line were then converted from the local system into the global coordinate system by applying a translation from the origin and a rotation, using rotation matrix R, by the calculated azimuth value.

$$R = \begin{bmatrix} cos(az) & sin(az) & 0 \\ -sin(az) & cos(az) & 0 \\ 0 & 0 & 1 \end{bmatrix}$$

Table 3.1: Parameters for Converting from Local to Global Coordinate System

Line	$X_{origin,global}$ (km)	$Y_{origin,global}$ (km)	Azimuth (degrees)
A4	0.9941	4.7278	82.729
A5	5.9935	4.7165	78.436
A6	-0.6796	4.7204	81.218
A9	3.5727	-4.5586	168.483
A10	3.0803	1.2432	-11.998

To create the 3D starting model, the preferred 2D models of Henig et al. (2012) were hung from the seafloor bathymetry in the global coordinate system. Structure between the profiles was interpolated between each set of two models, transitioning smoothly from one model to the adjacent model. Grid spacing was

set to 100 m by 100 m in the x- and y-directions and 50 m in the z-direction to reduce computation time (original 2D models are 50 m by 25 m in x and z, respectively). The same travel time picks and uncertainties were employed in the 3D inversion as were used for the individual 2D inversions of each line (Henig et al., 2012). Uncertainties range between 10-80 ms for a total of ∼220,000 picks.

Similar to the 2D inversion, the 3D inversion proceeded according to the method of Van Avendonk et al. (2004). Travel time residuals are minimized in a least squares sense until an overall model misfit parameter χ^2 is approximately 1. A value of 1 indicates that the models fit the data within the assigned uncertainties. Since the starting model was created by hanging 2D models of $\chi^2 \approx 1$ from the seafloor, the starting 3D model had a low initial misfit of 9.93.

3.4 Results and Discussion

3.4.1 3D Velocity Structure

Results of the velocity structure from the 3D inversion (figure 3) are quite similar to the individual models from the 2D inversion (figure 4) presented by Henig et al. (2012). The majority of deviations from the 2D models do not exceed 500 m/s, as illustrated in the difference plots (figure 5). As the 2D models were subtracted from the 3D models, positive anomalies represent faster 3D structure while negative indicates slower 3D structure compared to the preferred 2D models. The final χ^2 of the preferred 3D model is 1.00.

All new 3D models show a slight variation in structure from the 2D versions. In the upper ∼1.5 km, anomalies alternate between positive and negative on a 2-3 km scale in all profiles except A9, the across-axis southern profile. These particular anomalies are small; at most a few hundred m/s. This alternation most likely results from trade-off in fitting the far and near offset travel times of adjacent rays and is not due to actual variations in geologic structure.

In addition, a small difference in overall velocity structure does not bear much geologic significance in terms of distinguishing rock types. Many studies of seismic velocity structure of young oceanic crust formed at various rates of

spreading indicate uncertainties on the order of a few hundred meters per second (compilations cited in White et al., 1992). These uncertainties do not affect the lithologic interpretation of crustal type and are expected due to regular sources of error and the non-unique nature of seismic studies, as well as variable degrees of fracturing, alteration, pore space, and other variability in physical properties of the rocks themselves. More recent studies at axial slow spreading centers confirm this uncertainty range on the order of a few hundred meters per second for young shallow crust (Hussenoeder et al., 2002; Arnulf et al., 2011, 2012).

All of the 3D seismic velocity models further support the lithologic interpretations of Henig et al. (2012). In general, high velocity areas usually increase in velocity in the new models, while low velocity regions decrease. There are few exceptions to this rule, which are noted in the discussion of each individual profile. While the anomalies are insufficient to change the interpretation of rock type, they are useful for confirming the robustness of the 2D models.

3.4.2 Along-Axis Profiles

Explanation of the velocity structure of the new along-axis 3D seismic profiles will proceed from west to east, representing the oldest to youngest lithosphere. From breakaway to termination (Tucholke et al., 1998; Canales et al., 2004) the expectation is for outwardly-rotated upper crustal layers (Smith et al., 2006; 2008) in the west to transition to a mafic core in the center of the massif (Henig et al., 2012). Toward the east there is a rider-block composed of volcanic hanging wall (Canales et al., 2004; Henig et al., 2012) overlying the footwall.

Seismic line A6, the westernmost profile, has a slower overall velocity structure compared to the 2D model (figure 3a, 5a). This decrease in velocity supports the previously interpreted upper crustal lithology. On the southern end of the coverage, a slight increase in velocity occurs in the intermediate-valued velocity layer (IVVL) but does not exceed the prescribed IVVL velocities (Henig et al., 2012) and further distinguishes serpentinite from upper crustal velocities. The low velocity South Wall region has a slight decrease in values on line A6.

The travel time residual values for the 2D seismic velocity model for line A6

presented in Henig et al., 2012 (figure 5a of that paper) are consistently positive at near-offset arrivals, indicating shallow structure that is too fast for the data. It was suggested by these authors that there existed a shallow velocity top layer that was difficult for the model to resolve. With the 3D inversion, a decrease in velocity in the uppermost ∼100-200 m along the Central Dome portion of line A6 indicates that this low velocity veneer does, indeed, exist. Likewise, the highest velocities in all massif profiles, occurring at the base of line A6, is reduced in the 3D model. The decrease in velocities at the seafloor as well as at the base of coverage are compensated for by a slight increase in velocities at intermediate coverage depths where the high velocity body (HVB) is noticeable (figure 3a).

Similar to the westernmost line, the 3-D tomographic result for central line A4 (figure 3b) also slightly decreases in velocity directly beneath the seafloor according to the difference plot (figure 5b). This represents a possible deepening of the HVB from what was initially proposed. However, a thin low velocity layer is not clearly visible in the velocity model of A4 as it is for A6. This discrepancy could be caused by the lithospheric age difference between the two lines leading to additional fracturing and alteration to the west (line A6) or because of lithologic differences (preferred). Figure 5b shows a positive anomaly below the negative velocity anomaly representing a slower top layer, further increasing the velocity structure of the HVB.

Also in direct comparison to line A6, the southernmost portion of line A4 exhibits a decrease in seismic velocities in the 3D model. This is interpreted as confirmation of the IVVL and is consistent with serpentinite that outcrops on the face of the South Wall.

Three-dimensional seismic profile A5 (figure 3c), sampling the eastern Southern Ridge and the ridge of volcanic material considered to be hanging wall, also has deviations from the 2D model (figure 5c) that further support the lithologic interpretations of Henig et al. (2012). There is an overall decrease (with the exception of one location) in already low hanging wall velocities, which are in good agreement with velocities of extrusive volcanic crustal layer 2A (Arnulf et al., 2011; 2012; Henig et al., 2012).

In the eastern Southern Ridge, velocities in the location of the interpreted HVB slow slightly, while the velocities directly beneath the seafloor around x = -8.5 to -10.5 (perhaps a klippe, figure 5c) have a slight increase. This causes a subtle homogenization of the eastern Southern Ridge and could cast doubt on the interpretation of a klippe. No basalts have been sampled directly from this area, but they do exist in nearby dredges (Blackman et al., 2002).

3.4.3 Across-Axis Profiles

The most distinctive feature of line A9 (figure 3e) is a slight decrease in seismic velocity of the 3D model throughout the entirety of the ray coverage (figure 5e). The only place showing an increase in velocity is in the location corresponding to the HVB of Henig et al. (2012). This may indicate that the portions of the Southern Ridge interpreted by Henig et al. (2012) as serpentinized peridotite and the western transition to upper crustal layers may actually be more serpentinized or more fractured than initially thought.

The 3D difference plot for Line A10 shows a distinct negative velocity anomaly at approximately x = -2.5 km (figure 5d). The 3D model (figure 3d) is able to resolve a lower velocity (5-5.5 km/s) in this region, slightly reducing the velocities outcropping directly at the seafloor. Nevertheless, this velocity range is still unusually high and consistent with a gabbroic interpretation. The reduction in velocity described above divides two slightly positive velocity anomalies that indicate an increase in velocity of the core of the massif.

3.4.4 1D Profiles

Figure 6 shows the new 1D velocity profiles taken from the locations of line crossings plotted with the velocity-depth curves at line crossings of the 2D profiles. In certain instances the new line crossing is nearly evenly spaced between the 2D line crossing profiles (figure 6a, b, f), but in others it is much more similar to one of the crossing profiles or the other meaning there was little deviation from the structure of that line (figure 6c, d, e). As a generalization, the profiles are more

evenly distributed in areas of higher subsurface velocity.

3.4.5 Lithology and Structure

The 3D models confirm the interpretations of Henig et al. (2012). The Atlantis Massif is composed of a plutonic (gabbroic) core within the Central Dome and the eastern Southern Ridge. To the south, the Southern Ridge and the South Wall are composed primarily of serpentinized peridotite (of IVVL composition), which surrounds the HVB. To the west, toward the breakaway, there is a transition from the anomalous lithosphere of the OCC to more typical upper crustal layers of very low velocities. To the northeast, volcanic terrain interpreted as a remnant piece of the hanging wall sits atop the Central Dome.

3.5 Conclusion

Three-dimensional tomography provides a means for reconciling the velocity structure at the crossing locations of seismic profiles. Here we use the same first arrival travel time picks, uncertainties, and inversion mechanism used by Henig et al. (2012) to obtain 2D inversions. The sparse spacing of the profiles in this particular survey geometry and the expected structure do not allow for interpretation of structure more than a few hundred meters from any profile.

Deviations of the new models from the original 2D models are small. Most anomalies are less than 500 m/s, which does not change the overall lithologic interpretation. Positive velocity anomalies in key parts of the models confirm regions of high velocity (high velocity body(ies)), while negative anomalies correspond to regions of lower velocity packages (IVVL and extrusive volcanic rocks).

References

Arnulf, A., S. Singh, A. Harding, G. Kent, and W. Crawford (2011), Strong seismic heterogeneity in layer 2a near hydrothermal vents at the mid-atlantic ridge, *Geophysical Research Letters*, *38*(13), L13,320, doi:10.1029/2011GL047753.

Arnulf, A. F., A. J. Harding, S. C. Singh, G. M. Kent, and W. Crawford (2012), Fine-scale velocity structure of upper oceanic crust from full waveform inversion of downward continued seismic reflection data at the Lucky Strike Volcano, Mid-Atlantic Ridge, *Geophysical Research Letters*, *39*(8), L08303, doi: 10.1029/2012GL051064.

Blackman, D. K., J. A. Karson, D. S. Kelley, J. R. Cann, G. L. Früh-Green, J. S. Gee, S. D. Hurt, B. E. John, J. Morgan, S. L. Nooner, D. K. Ross, T. J. Schroeder, and E. A. Williams (2002), Geology of the atlantis massif (mid-atlantic ridge, 30 n): Implications for the evolution of an ultramafic oceanic core complex, *Marine Geophysical Researches*, *23*(5), 443–469, doi: 10.1023/B:MARI.0000018232.14085.75.

Blackman, D., B. Ildefonse, B. John, Y. Ohara, D. Miller, and C. MacLeod (2006), Expedition 304/305 scientists, in *Proceedings of the Integrated Ocean Drilling Program*, vol. 304/305, doi:10.2204/iodp.sp.304305.2005.

Canales, J., B. Tucholke, and J. Collins (2004), Seismic reflection imaging of an oceanic detachment fault: Atlantis megamullion (mid-atlantic ridge, 30°10'n), *Earth and Planetary Science Letters*, *222*(2), 543–560, doi: 10.1016/j.epsl.2004.02.023.

Canales, J., B. Tucholke, M. Xu, J. Collins, and D. DuBois (2008), Seismic evidence for large-scale compositional heterogeneity of oceanic core complexes, *Geochemistry Geophysics Geosystems*, *9*(8), Q08,002, doi:10.1029/2008GC002009.

Henig, A., D. Blackman, A. Harding, J. Canales, and G. Kent (2012), Downward continued multichannel seismic refraction analysis of atlantis massif oceanic core complex, 30°n, mid-atlantic ridge, *Geochemistry Geophysics Geosystems*, *13*(null), Q0AG07, doi:10.1029/2012GC004059.

Hussenoeder, S., G. Kent, and R. Detrick (2002), Upper crustal seismic structure of the slow spreading mid-atlantic ridge, 35°n: Constraints on volcanic emplacement processes, *J. geophys. Res*, *107*(B8), 2156, doi:10.1029/2001JB001691.

Smith, D., J. Cann, and J. Escartín (2006), Widespread active detachment faulting and core complex formation near 13°n on the mid-atlantic ridge, *Nature Letters*, *442*, 440–443, doi:10.1038/nature04950.

Smith, D., J. Escartín, H. Schouten, and J. Cann (2008), Fault rotation and core complex formation: Significant processes in seafloor formation at slow-spreading mid-ocean ridges (mid-atlantic ridge, 13-15°n), *Geochemistry, Geophysics, Geosystems*, *9*(3), Q03,003, doi:10.1029/2007GC001699.

Tucholke, B., J. Lin, and M. Kleinrock (1998), Megamullions and mullion structure defining oceanic metamorphic core complexes on the mid-atlantic ridge, *Journal of Geophysical Research*, *103*(B5), 9857–9866, doi:10.1029/98JB00167.

Van Avendonk, H., D. Shillington, W. Holbrook, and M. Hornbach (2004), Inferring crustal structure in the aleutian island arc from a sparse wide-angle seismic data set, *Geochemistry, Geophysics, Geosystems*, *5*, Q08,008, doi: 10.1029/2003GC000664.

White, R., D. McKenzie, and R. O'Nions (1992), Oceanic crustal thickness from seismic measurements and rare earth element inversions, *Journal of Geophysical Research*, *97*(B13), 19,683–19,715, doi:10.1029/92JB01749.

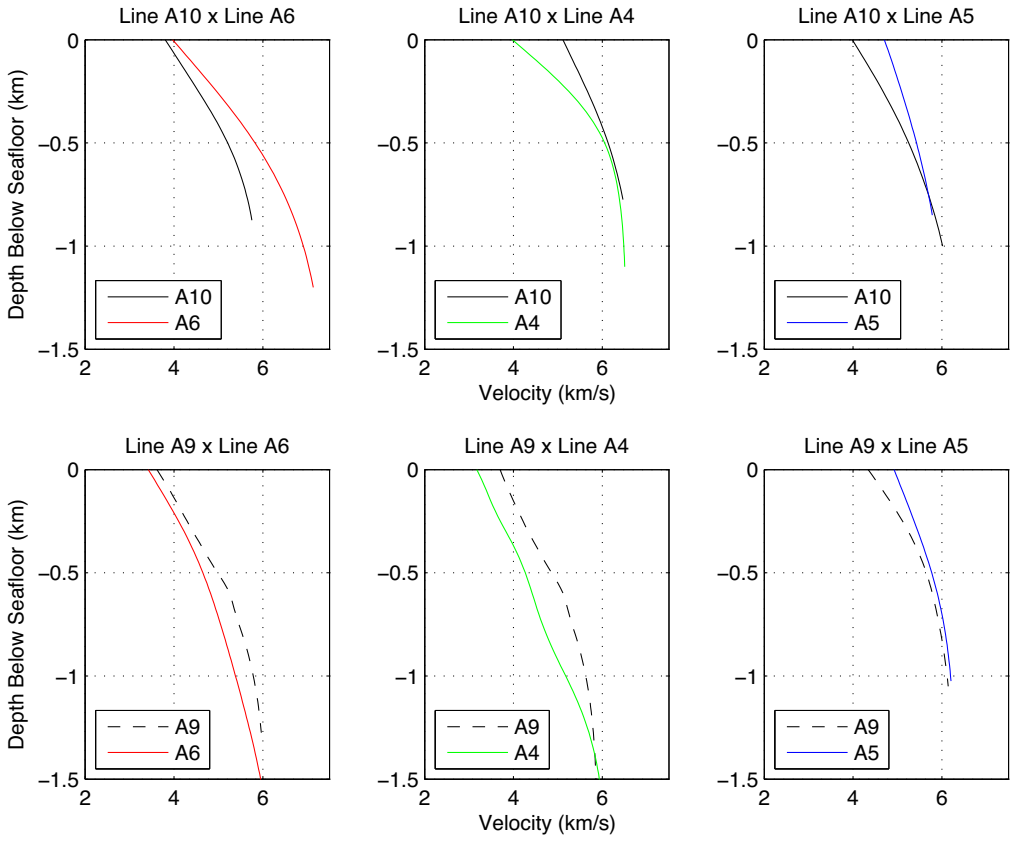

Figure 3.1: One-dimensional velocity profiles in the locations of seismic profile intersections of the 2D inversions. Each panel represents one line crossing, with each 1D profile taken from each line at the place of intersection. Red line A6; Green line A4; Blue line A5; Black line A10; Dashed Black line A9.

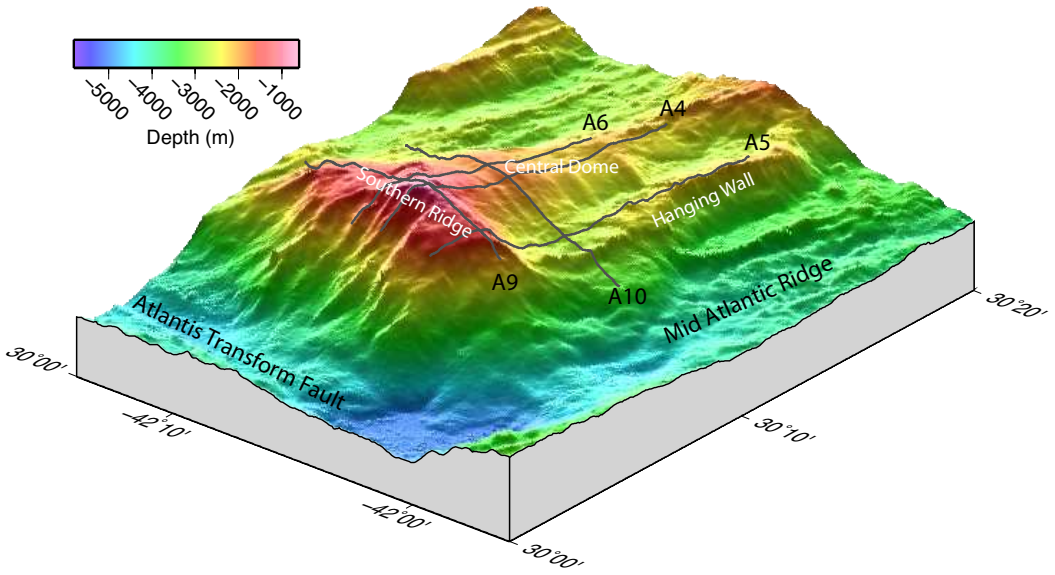

Figure 3.2: Map of Atlantis Massif showing the five seismic profiles and the main morphologic components of the OCC: the Central Dome, the Southern Ridge, the Hanging Wall.

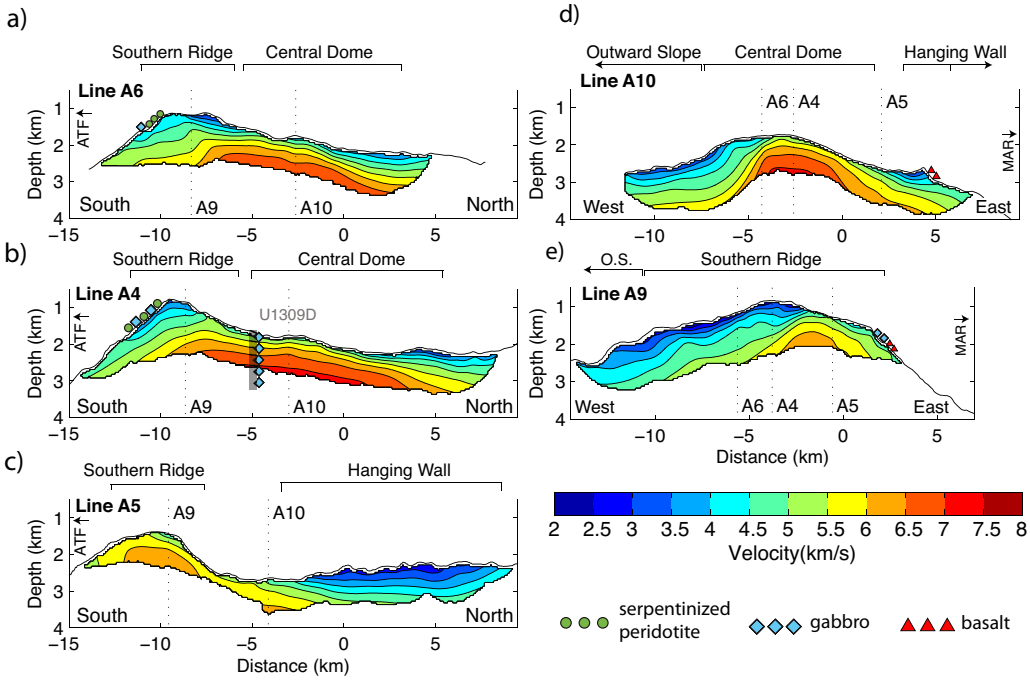

Figure 3.3: Velocity models for each individual line taken as a slice from the 3D model. a-c) Along-axis profiles; d-e) across-axis profiles. Locations of crossing profiles are shown by labeled black dashed vertical lines. Dominant lithologies determined from previous studies shown by green circles (serpentinite), blue diamonds (gabbro), and red triangles (basalt). Location of Integrated Ocean Drilling Program Hole U1309D projected onto b) line A4. O.S. Outward Slope; ATF Atlantis Transform Fault; MAR Mid Atlantic Ridge.

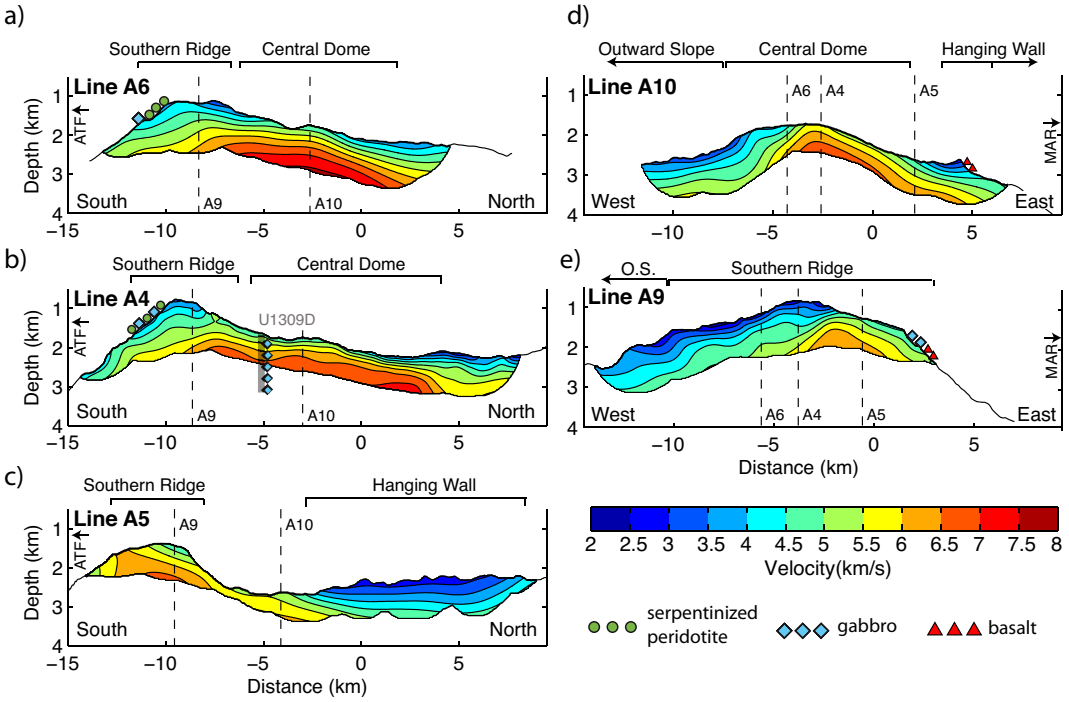

Figure 3.4: Velocity models from individual-line two-dimensional inversions. a-c) Along-axis profiles; d-e) across-axis profiles. All lines, symbols, and abbreviations are consistent with figure 3.

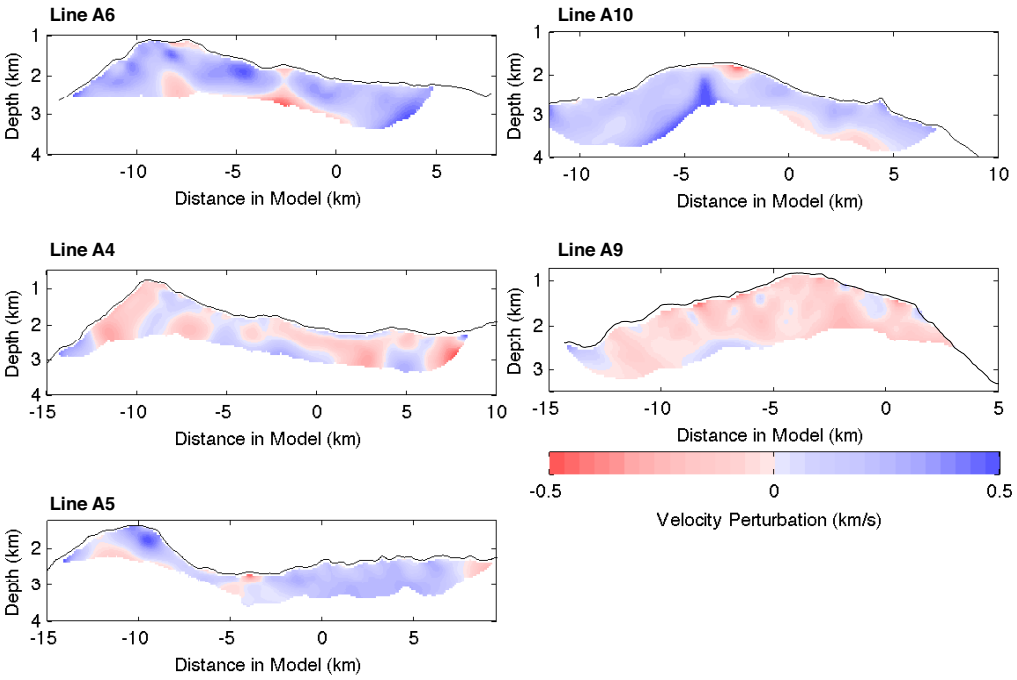

Figure 3.5: Difference plots of velocity models where the 2D models have been subtracted from the 3D models. Positive anomalies represent faster 3D structure, while negative anomalies represent slower 3D structure when compared to the 2D models.

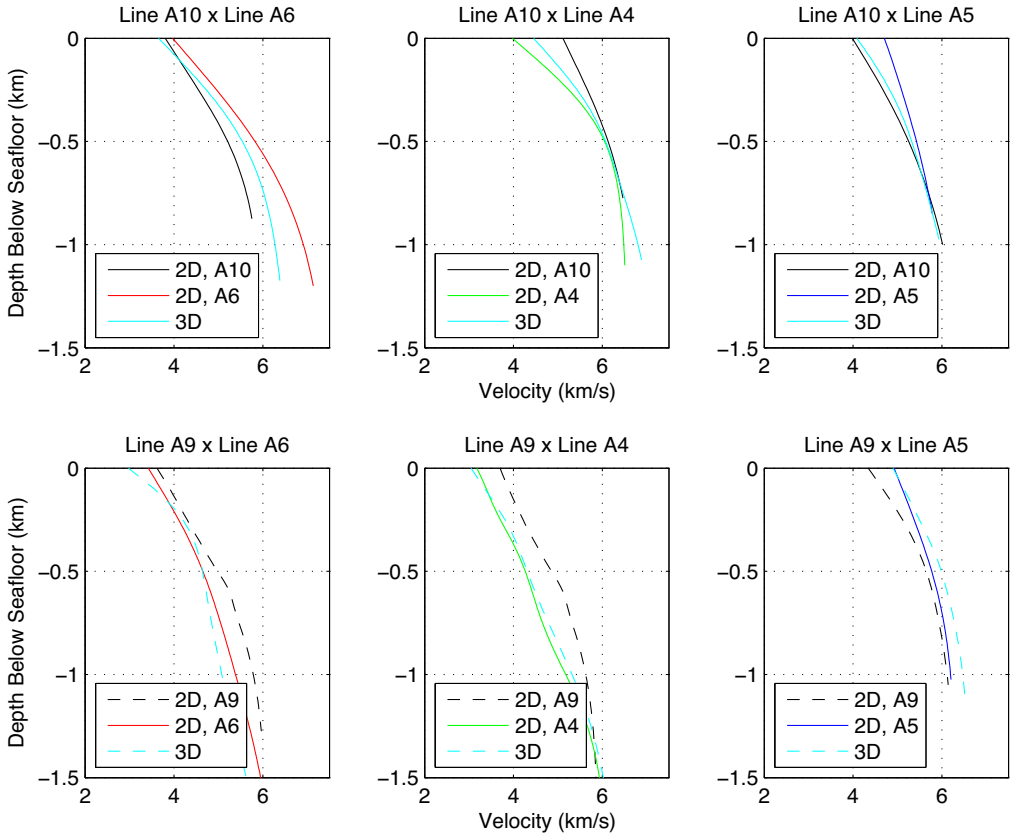

Figure 3.6: Same as figure 1, with the addition of 1D profiles taken from the 3D inversion models at the location of line crossings. Solid Cyan represents profiles extracted from the 3D inversion of line A10. Dashed Cyan represents profiles taken from the 3D inversion of line A9. The following represent profiles from the 2D inversion: Red line A6; Green line A4; Blue line A5; Black line A10; Dashed Black line A9.

Chapter 4

Structure of Propagating Central Lau Spreading Center from MultiChannel Seismic Data

The propagating Central Lau Spreading Center (CLSC), in the Lau Backarc Basin, is the latest in a succession of attempts to initiate a viable spreading system in the north and center regions of the basin. Densely spaced Multi-Channel Seismic refraction and reflection data enable improved determination of the along- and across-axis shallow crustal structure of the southern ∼140 km of the CLSC, down to a depth of ∼1-2 km. We employ the Synthetic Ocean Bottom Experiment (SOBE) downward continuation technique to increase the number of usable first arrival picks, improving vertical resolution in the shallow crust. These data are used to study: 1) the along axis crustal properties associated with the CLSC southward propagating ridge tip, and 2) the across axis changes in structure associated with aging and juxtaposition of two different crusts across pseudofaults. Our new tomographic models show a dramatic change in the thickness of layer 2 as the tip of the propagator is approached. Based on shot gather analysis and tomography, crustal layer 2A (high velocity gradient region, >6 s^{-1}, with low absolute velocities, $\sim$ 3 km/s) maintains a relatively constant thickness of ∼350-500 m along ∼120 km of the CLSC north of the propagating rift, showing little local variation in structure associated with the previously observed segmentation of the

underlying axial magma chamber (AMC). Layer 2A transitions to a thickness of $>$ 600 m starting about 15 km north of the bathymetrically defined ridge tip. Our results suggest a change in the accretionary mechanism toward the propagating tip as diffuse diking likely becomes the norm, building a thickened layer 2A and layer 2A/2B transition zone, characterized by interspersed dikes and lavas. Layer 2B ($>$ 4-5 km/s, with a low velocity gradient) is imaged with a thickness of at least 500 m for the majority of the CLSC, but has reduced velocities or starts deeper near the propagator. The across-axis velocity structure of the ridge flanks, while indicating a thickening of layer 2A and deepening of the 2A/2B transition zone from north to south, is different on- and off-axis, with the off-axis crust similar in velocity structure to the Valu Fa Ridge in the south. We note that the new axial crust is distinctive from the crust into which is it spreading, however there is no sharp lateral velocity contrast. This is attributed to an alteration or rejuvenation of the original crust, which has been extended, intruded, repaved, and in the case of the northern along-axis regions, newly-formed.

4.1 Introduction

4.1.1 Background

It has long been debated whether the seafloor spreading occurring in backarc basins is fundamentally similar to that taking place at mid-oceanic ridges (MORs) or if different processes, such as diffuse deformation and magmatism (*Lawver et al.*, 1976; *Lawver and Hawkins*, 1978; *Hamburger and Isacks*, 1988), are occurring. Studies of magnetic anomalies (*Taylor et al.*, 1996), bathymetry and ridge morphologies (e.g. *Wiedicke and Habler*, 1993), and crustal structure (*Jacobs et al.*, 2007) indicate that similar spreading mechanisms are indeed occurring at both MORs and backarc spreading centers that are sufficiently far from the subduction zone. Despite moderate differences in crustal thicknesses, a three-layer model has been adopted as canonical for oceanic crust at MORs, with the exception of ultra-slow and some slow spreading locations, based upon ophiolite studies. This consists of upper crustal layers composed of pillow basalts ($\sim$ 500 m thick) and sheeted

dikes (∼1500 m thick), respectively, and lower crust with gabbroic composition (*Penrose*, 1972).

In addition to the interpreted rock type, layers of oceanic crust are defined and distinguishable by their characteristic seismic velocities. Historical compilations of seismic studies (e.g. *White et al.*, 1992) and more recent studies (*Hussenoeder et al.*, 1996; *Grevemeyer and Weigel*, 1996, 1997; *Nedimović et al.*, 2008; *Newman et al.*, 2011; *Arnulf et al.*, 2012) at young axial crust characterize the top of layer 2A by velocities around 2.5 km/s and the top of layer 2B by velocities $<$ 5 km/s with a very low 2B intra-layer gradient (*Vera et al.*, 1990; *Harding et al.*, 1993; *Carlson*, 1998). The ten to hundreds of meters thick transition that separates these two upper crustal layers has a very high gradient. The origin of this transitional boundary is debated (*Harding et al.*, 1993; *Christeson et al.*, 2007). Layer 3, which forms the bulk of the oceanic crust, also has low velocity gradients. The base of layer 3 is associated with a transition to velocities exceeding 7 km/s.

A natural aging process takes place in the upper oceanic crust and seismic velocities increase rapidly in layer 2A during the first 5 Myr after formation (*Carlson*, 1998). *Carlson* (1998) shows from seismic compilations that seismic layer 2A, which starts out with velocities $<$ 3 km/s, can increase to $>$ 5 km/s by 5 Myr, and that by 10 Myr no velocities $<$ 3 km/s remain. This velocity change is likely due to an infilling of pore space and cracks due to precipitation associated with hydrothermal circulation (*Houtz and Ewing*, 1976; *Vera et al.*, 1990), which causes a reduction in porosity and an increase to crustal velocity (*Wilkens et al.*, 1991) in only a few million years.

On occasion, spreading centers will die out or be overtaken by adjacent propagating spreading segments. These propagating spreading centers are a relatively common feature at MORs (e.g. *Hey*, 1977; *Hey et al.*, 1980), but the structure of the crust formed at the apex of these features is not well known. Scars in the seafloor, termed pseudofaults (*Hey*, 1977), are formed from wakes created as the propagator cuts through older crust, and indicate the history of ridge propagation. Across the pseudofaults, crust formed at the new spreading center is juxtaposed next to crust formed at the dying spreading center, into which the ridge is prop-

agating. The implication is that a strong velocity gradient could exist across the pseudofaults, if the crust on either side is of significantly different age or composition.

This study makes use of several Multichannel seismic (MCS) profiles to determine the crustal structure and aging properties of crust formed at the Central Lau Spreading Center (CLSC), a spreading center within the Lau Backarc Basin with the same magmatic compositions (*Pearce et al.*, 1994) and bathymetric signatures (*Wiedicke and Habler*, 1993), among other properties, as an intermediate-fast spreading MOR segment. The goal is to define the crustal structure associated with this propagating spreading segment and to provide an interpretation of the accretionary history.

4.1.2 Geologic Setting

The Lau Backarc Spreading Center is located in the Lau Backarc Basin, the fan-shaped basin formed from rifting behind the volcanic arc associated with the Tonga-Kermadec subduction zone. It is a 700 km long spreading center segmented into three main regions with variable spreading rates between ∼40 km/Myr in the south to ∼100 km/Myr in the north. These segments are the Central Lau Spreading Center (CLSC) between 18°S and 19°20′S, the Eastern Lau Spreading Center/Valu Fa Ridge (ELSC/VFR) between 19°20′S and 22°45′S, and the Intermediate Lau Spreading Center (ILSC), which is a short relay basin between the CLSC and ELSC. Figure 4.1 shows these features and the geometry of the Lau Backarc Basin and the spreading systems.

Crustal stretching and magmatic intrusion initiated the opening of the Lau backarc basin at about 6 Ma (*Parson et al.*, 1990; *Hawkins et al.*, 1994; *Hawkins*, 1995). The basin has two main subsequent stages of extension leading to seafloor spreading, the first occurring between ∼ 4-2 Ma due to the southward propagation of what is now the ELSC (*Taylor et al.*, 1996). A rotation of 15-25° (*Taylor et al.*, 1996) occurred in the ELSC around 2 Ma, resulting in the central and northern segmentation and offset of the previously continuous axis. The CLSC was initiated and began propagating southward, eventually overtaking the northern

portion of the ELSC. The CLSC continues to propagate southward today at the expense of the nELSC, although its rate is debated (*Wiedicke and Habler*, 1993; *Zellmer and Taylor*, 2001). The ELSC crust that is currently being cut into by the CLSC is about 1.7 Ma (*Parson and Hawkins*, 1994). A 70 km, left-stepping non-transform offset separates the CLSC and the ELSC, wherein two evenly spaced basins accommodate extension between the two spreading segments (*Wiedicke and Habler*, 1993). The eastern basin is referred to as the ILSC as it is more developed, containing recent volcanism, compared to its western counterpart (*Parson et al.*, 1990).

The distance between the spreading center and the active volcanic arc decreases along the ridge from north to south and, as such, the spreading center experiences varying degrees of arc influence (e.g. *Martinez and Taylor*, 2002; *Jacobs et al.*, 2007; *Escrig et al.*, 2009; *Dunn and Martinez*, 2011) related to factors such as subduction-associated mantle hydration and entrainment, mantle temperature, and subduction rate (*Langmuir et al.*, 2006; *Martinez et al.*, 2006). The ridge morphology, lithospheric structure, and magma chemistry changes along the length of the ridge as a result of the subduction influence, sometimes continuously and sometimes relatively abruptly. The variability in accretionary properties due to the above factors causes crustal structure to vary along the strike of the Lau spreading centers (*Jacobs et al.*, 2007).

In the north, the CLSC is 160-185 km from the arc and has no island-arc influence because the spreading center lies far enough west of the mantle region affected by subduction (*Pearce et al.*, 1994; *Martinez and Taylor*, 2002; *Dunn and Martinez*, 2011). Indeed, the morphology of the ridge is shallow with an axial high (*Martinez and Taylor*, 2002), there is a strong axial magma chamber (AMC) reflector (*Jacobs et al.*, 2007), and the lava compositions are similar to mid-ocean ridge basalts (MORB) (*Hawkins et al.*, 1994; *Hawkins*, 1995; *Pearce et al.*, 1994). The ELSC however, which is composed of the northern and central ELSC (n-ELSC, c-ELSC) segments and the VFR segment, with a minimum distance of 40 km from the arc, has a trend in morphology that is anti-correlated with that expected based on spreading rate. The high, triangular geometry of the slow-spreading (39

mm/yr) VFR in the south and the broader, deeper axial morphology of the faster spreading (<97 mm/yr) c- and n-ELSC segments to the north (*Martinez et al.*, 2006), are attributed to the southward increase in proximity of the subduction zone and to depletion of the mantle wedge that feeds the spreading center (*Martinez and Taylor*, 2002). The transition from n-ELSC to c-ELSC is abrupt, marked by the transition from axial valley to axial high, the appearance of an AMC and a distinct change in magma chemistry.

Wiedicke and Habler (1993) provide a detailed morphologic analysis of the CLSC, its spreading-process-based segmentation, and the lateral extent of CLSC-formed crust based on GLORIA side-scan (*Parson et al.*, 1990) and Sea Beam multibeam bathymetry available to them at the time. Five regions are defined from south to north along the CLSC, and are shown in Figure 4.2a, as follows: 1) a narrow rift graben/tectonic ridge tip, 2) a leaky rift graben/initial volcanic tip, 3) a rift graben with an initial volcanic ridge/neovolcanic tip, 4) a transition zone characterized by a widening and deepening of the rift and a 30° bend of the volcanic ridge, and 5) a full-rate spreading ridge/full rate tip. *Parson and Hawkins* (1994) and *Zellmer and Taylor* (2001) identify the crust being cut into by the CLSC as having formed during magnetic chron 2 (at least 1.7 Ma) and being composed of andesitic basalts, more akin to the composition of the current VFR crust than to that of the current nELSC crust.

Improved bathymetry, side scan, and magnetic data (Figure 4.2) allow for a more accurate identification of new crust formed at the CLSC and thus the determination of preferred pseudofault locations that are used in this study. The side scan shows that the reflective seafloor is not symmetric about the current spreading axis north of the full rate tip as thought by *Wiedicke and Habler* (1993), but is actually far broader to the west than it is to the east (Figure 4.2b). The same asymmetry exists in the magnetic data as well (Figure 4.2c). These patterns indicate that relatively young, unsedimented seafloor forms preferentially to the west of the CLSC and corresponds with a series of basins striking NNE-SSW to N-S, which are labeled in Figure 4.2a as the western basins.

This study expands on the previous study of *Jacobs et al.* (2007), which

created 1D average velocity profiles of the upper crust at discrete locations along the entire length of the Lau Backarc Spreading Center to assess crustal structure as a function of subduction influence. That study employed supergathers formed from a vertical stack of 24-48 successive CMP gathers and took advantage of the consequent improved signal-to-noise to pick secondary refraction arrivals. It was, however, limited to regions of subdued seafloor topography and subdued seafloor scattering and could not be applied to across-axis lines. Here we focus only on structure of the CLSC but develop continuous 2D velocity profiles from both along and across axis data by relying on downward continuation to enable us to pick refractions as first arrivals at all offsets (*Harding et al.*, 2007; *Arnulf et al.*, 2011; *Henig et al.*, 2012). This study updates the history of spreading at the CLSC by combining new seismic results with existing geophysical measurements, including magnetics, side-scan, and more complete bathymetry not available to *Wiedicke and Habler* (1993). Using the well-supported assumption that the CLSC spreads via the same processes as a MOR, we assess velocity variability along axis into the trace of the propagating tip with the hope of learning about crustal structure and accretionary mechanisms at a propagating ridge, and across axis to assess aging properties within young crust and across pseudofaults.

4.2 Data Acquisition

The entire length of the Lau Backarc Spreading Center between 18°S and 22°45′S was surveyed for multichannel seismic data aboard the R/V Maurice Ewing cruise EW9914 in 1999. A total of 61 lines were collected both along and across the 700 km long axis from the Central Lau Spreading Center to the Valu Fa Ridge. The bathymetry of *Taylor et al.* (1996) was used to guide the survey along the ridge axes. This study focuses on seven of the 16 lines collected at the CLSC. Four of these are across-axis near the southward propagating ridge tip, while three overlapping along-axis lines survey a continuous 140 km section of the CLSC.

A 10-airgun seismic source array with total capacity of 50 l (3048 in^3) was towed at a nominal depth of 8 m and fired at a mean shot spacing of 37.5 m during

the survey. Waveform data were recorded on a 6 km streamer towed behind the ship at a depth of 10 m. Receivers were spaced every 12.5 m with a total of 480 channels, resulting in 80-fold common midpoint gathers. Shot and streamer position were determined using ship-board GPS, digital compass and depth birds, and a tail-buoy GPS.

4.3 Methods

4.3.1 SOBE Downward Continuation and Additional Processing

To enhance our models in the upper few hundred meters, we make use of the Synthetic Ocean Bottom Experiment (SOBE) downward continuation technique (*Harding et al.*, 2007; *Arnulf et al.*, 2011; *Henig et al.*, 2012) to uncover the near-offset, shallow-turning refracted arrival within the data gathers. The current version of SOBE employs a flexible Kirchhoff redatuming algorithm (*Shtivelman and Canning*, 1988) to reposition both shots and receivers to a variable depth datum a fixed distance above the seafloor. As a result of downward continuation, the water wave is collapsed to a point at zero offset and triplications caused by high gradients are mostly unwrapped.

This method combines and improves upon the detailed shallow coverage of a typical ocean bottom seismometer (OBS) study with the dense and evenly spaced coverage of an MCS survey. SOBE is most useful in areas of deep seafloor and low subsurface velocities. In regions with these attributes, such as MORs, the water bottom reflection will obscure the majority of the upper crustal refraction except at large streamer offsets. The CLSC is thus an excellent candidate for employment of SOBE based on these criteria.

The additional near-offset refractions made available for picking by SOBE correspond to crustal rays turning at shallow depths (∼300-400 m) and provide structural constraint in the upper portions of our models. The detail of this structure can be further improved by full waveform inversion (*Pratt*, 1999; *Shipp and*

Singh, 2002) used in combination with SOBE (*Arnulf et al.*, 2012). Improving upper crustal detail increases confidence in deeper crustal structure as well, because of the implicit layer stripping involved in resolving deeper structure.

Besides downward continuation, little data processing was required. Signal to noise ratios (SNR) are generally high, and post-downward-continuation refraction arrivals are clear, coherent, and continuous. Prior to applying SOBE, amplitude scaling was applied to the traces and consistently noisy traces were replaced by interpolation from adjacent traces in order to provide the downward continuation algorithm with more uniform amplitude data across all traces and reduce processing artifacts. Prior to downward continuation, a fourth-order Butterworth filter was employed with a bandpass of 5-20 Hz to diminish noise and unusable frequencies, while a 20 Hz low pass filter was applied prior to the common receiver location extrapolation to avoid spatial aliasing. A water velocity of 1.5 km/s was assumed for all stages of SOBE.

4.3.2 Picking of Travel Times

First refracted arrival travel time picks were made for all usable traces from every fifth shot gather along all seven lines studied. All visible first breaks were picked except for near-offset traces 451-480, which were potentially influenced by the shape or incomplete collapse of the water wave.

Data quality was very good with high SNR so low pick uncertainties were assigned, averaging between 10-14 ms depending on the line. Pick coverage for all lines is broadly and evenly distributed, and represented in Figure 4.3 by the number of traces picked for each shot. Picks were made using a cross-correlation function and then visually inspected and adjusted if necessary.

4.3.3 Tomographic Inversion

First refracted arrival picks from seven lines were inverted for tomographic P-wave velocity structure using the least squares approach of *Van Avendonk et al.* (2004). In this method, models are iteratively updated while gradually reducing

the weighted misfit, χ^2, between predicted and observed travel times. In the end, we attempt to achieve an overall model misfit of $\chi^2 = 1$, indicating that the model fits the data within the prescribed pick uncertainties.

For a given model, the χ^2 value is strategically reduced by a small amount throughout a series of iterations, to satisfy the linearity assumption within each inversion. The current model is updated according to the requested χ^2 and smoothing parameters, rays are traced through the new model, and statistics are evaluated. The χ^2 and smoothing parameters are then adjusted and the process repeated. The ratio of horizontal to vertical smoothing length is held relatively high throughout the inversions based on a priori assumptions of relatively laterally homogeneous crustal structure. The sequence of changes in parameters varies for each line allowing an optimal fit for each set of data.

Our goal is to obtain the most geologically plausible model while fitting the data to within the uncertainties. Our uncertainties are very low, even so χ^2 values lower than 1 are obtained for some models while still improving the travel time residuals and without introducing noticeable artifacts into the model. Indeed, reducing the uncertainties, in an attempt to optimize fit for a χ^2 of 1 still results in misfits that continue to decrease as χ^2 passes through 1 to lower values around 0.6. This reduction in χ^2 corresponds to a reduction in root mean square (RMS) travel time residuals of $\sim$2 ms. Clearly, pick uncertainties are very low and the models fit the data better than the assigned uncertainties depict.

4.3.4 Locating Axial Magma Chamber

Due to the 6 km streamer length used for this survey, the deepest turning energy recorded by the streamer is from above the top of the AMC. In order to determine the depth of the AMC and thus the base of layer 2B, the AMC reflection may be picked from standard or downward continued shot gathers. In the case of these data however, the AMC proved very difficult to pick and in many cases no arrivals were discernable in the individual shot gathers.

As an alternative, we employed AMC picks from the zero-offset stacked reflection sections to serve as a guide for the top of the AMC in our inversions.

Based on the current results for refractions only and the 1D results of *Jacobs et al.* (2007), who used the curvature of the AMC reflection to constrain velocities within the lower part of layer 2B, it is reasonable to assume that the velocity gradient is low within layer 2B. The principal uncertainty is the depth of the AMC which can be determined from the zero offset times. To create an initial AMC model, the AMC picks were converted to depth by using the average velocity structure of *Jacobs et al.* (2007), interpolated and extended to the length of the model space, and inserted into the model as an interface. We extended the layer 2B velocity from the base of the refraction coverage to the top of the AMC to complete the model.

An additional 1-2 inversion iterations were performed using the AMC reflection picks to smooth the AMC interface and the crustal refraction picks to adjust the velocity structure of the upper crust. In this way, we obtain full tomographic velocity models from the seafloor to the top of the AMC to be compared with stacked reflection sections. The majority of our analysis, however, is based only on the shallower portions of the models where there is refracted ray coverage (Figures 4.4 and 4.5).

4.4 Results

Our preferred 2D tomographic models are shown in Figures 4.4 and 4.5. Velocities are generally typical of young oceanic crust (*Harding et al.*, 1993). Due to the finite streamer length and the subsurface velocity structure, ray coverage for these models only extends through the upper $<$ 1-2 km of structure. The locations of the along-axis profiles are shown in the inset map in Figure 4.4. There is a southwestward kink in the spreading center and seismic profile at 18°16′S, and a southeastward kink again at ∼18°52′S. The profile extends to the initial volcanic tip of *Wiedicke and Habler* (1993), but stops a few kilometers north of the bathymetrically defined ridge tip. Likewise, the across-axis profile geometry is shown in context of the along-axis profiles in the inset map of Figure 4.5. The across-axis profiles cross the axis at nearly right angles. Line 10 crosses the axis

at approximately the location of the full rate spreading tip, while line 14 crosses just a few kilometers south of the neovolcanic tip (*Wiedicke and Habler*, 1993).

4.4.1 Along Axis Models

A nearly continuous 140 km of axial crust is sampled along profiles 7a, 7b, and 7c, north of the bathymetric depression representing the tip of the propagating ridge. Lines 7a and 7b in the north have a quite homogeneous character along axis (Figure 4.4). Layer 2A, defined in this study as the relatively high velocity gradient region with low absolute velocities, has a thickness between 350-500 meters for the majority of the profiles and is underlain by the layer 2A/2B transition. Layer 2B, defined here by velocities >4-5 km/s and a low velocity gradient, underlies the transition zone.

A segmentation of the along-axis profiles, based on velocity structure, is apparent from the models. The region between 18°09′S and 18°43′S (x = 10-80 km in model space) has relatively constant layer 2A thickness and fast layer 2B velocities. Latitudes 18°43′S to 19°06′S (x = 80-124 km) have slightly thicker layer 2A and lower layer 2B velocities. The southern region encompassing latitudes 19°07′S to 19°15′S (x = 125-141 km) has the most distinct structure, with a significantly thickened layer 2A.

Average vertical velocity profiles for various structural regions along the length of the line 7a-c segments illustrate the above observations, and are shown in Figure 4.6 as the average, minimum, and maximum values for each region. The constant thickness of layer 2A and its modest but abrupt thickening at ∼84 km in model space (Figure 4.4), can be easily observed from these profiles (red profile in Figure 4.6). The change of velocity gradient in the transition zone is also noticeable, as is the nearly constant velocity gradient layer 2B. Line 7a has a higher velocity layer 2B than line 7b with velocities > 5 km/s in the bottom ∼200-400 m of ray coverage.

Line 7c, covering the southern 30 km of the axis and imaging across the neovolcanic tip of the propagator, has a distinctively different structure from the rest of the along axis line (Figure 4.6, green profiles). About 15 km from the prop-

agating tip, layer 2A thickens to ∼600 m, the 2A/2B transition gradient relaxes, and layer 2B deepens and decreases in velocities (Figure 4.4).

These observations of change in crustal structure along line 7c are correlatated to changes in the stacked reflection section. As shown in Figure 4.7, the reflector representing the boundary of layer 2A (green reflector in center panel) truncates as the layer 2A gradient relaxes in the tomographic model, about 11 km north of the propagating tip. The AMC reflector (red reflector in central panel of Figure 4.7) also dies out about 18 km north of the tectonic propagator tip just ahead of the thickening in layer 2A.

Travel time residuals for these along axis profiles are generally low, with mean travel time residuals of 10 ms for lines 7a and 7b and 12 ms for line 7c (Figure 4.3a). One noticeable characteristic stands out from the otherwise random pattern: the nearest offset residuals are all positive. This indicates that the rays are arriving too early and thus the model is too fast in the structure directly subsurface. As noted by *Henig et al.* (2012), the inversion method employed has some difficulty resolving the low velocity uppermost layers when they are underlain by high velocity gradients such as in the layer 2A/2B transition zone.

4.4.2 Across Axis Models

The across axis preferred models are shown from north to south in Figure 4.5. The across axis data were generally more difficult to pick for travel times and had overall higher travel time residuals (Figure 4.3b) than the along axis models, due to the short length, more heterogeneous structure, and rougher topography compared to the along axis profiles. The average assigned pick errors were slightly higher for these lines, allowing for χ^2 to still converge to 1 despite the higher travel time residuals. The particularly short line lengths of profiles 12a and 12b meant it was possible only to downward continue the data in shot gather space. Thus, the picks are only at relatively far offset (3-6 km) compared to the other lines in this study (Figure 4.3b).

From north to south, the structure transitions from a layered structure, albeit with some heterogeneities (line 10), to a thickened section of low velocities

typical of layer 2A (line 14). The western two-thirds of the northernmost line 10 have the typical structure of crustal layers 2A and 2B, as defined above, with the high gradient transition zone between. However, the eastern third of the line (>4 km in model space) has velocities indicative of a thickened layer 2A structure and a more relaxed layer 2A/2B transition zone (Figure 4.8a). Indeed, east of the axial high, the velocity structure is similar to that seen along-axis at the southern end of line 7c. Within the ∼7 km wide axial high on line 10, are two areas (x = -2 km and x = 0.5 km in model space) where higher velocities shoal moderately, 2A thins, and the transition zone gradient increases, compared to the surrounding structure (Figure 4.5).

Lines 12a and 12b are closely-spaced profiles located on conjugate sides of the ridge with 12a about 3 km south of 12b. These profiles show the thickening of layer 2A: with the exception of the structure within 1.5-2 km on either side of the axis, layer 2A is about 500 m thick (Figure 4.8b, line 12b off-axis values). Directly at the axis, layer 2A is ∼400 m thick (Figure 4.8b, line 12b on-axis values). The 2A/2B transition also thickens and relaxes off-axis. These two lines still show an axial ridge in cross-section, similar to line 10.

The southernmost across-axis line, profile 14, intersects along-axis profile 7c near the propagating tip. The axial region on this line forms a depression in the topography, unlike the more northern profiles. The velocity structure is quite homogeneous along the length of this profile, showing minimal differences between the axial and flank portions of the line (Figure 4.8c). Figure 4.8c shows the velocity probability density for almost the entirety of line 14. Layer 2A along profile 14 is ∼500-600 m thick. The remainder of the ray coverage contains velocities corresponding to the 2A/2B transition. Layer 2B is not imaged by this model.

4.5 Discussion

4.5.1 Upper Crustal Structure Along Axis

As outlined above, the axial crustal structure of the northern 120 km of the along axis lines is quite homogenous and consistent with the upper portion

of a three-layer oceanic crustal/ophiolite model (*Penrose*, 1972). The majority of the along-axis line at the intermediate to fast spreading CLSC consists of layer 2A thicknesses that are comparable to or slightly thicker than those from previous studies of axial layer 2A. Typical axial layer 2A thicknesses at the fast spreading East Pacific Rise (EPR) are approximately 200-300 m (*Harding et al.*, 1993; *Detrick et al.*, 1993; *Kent et al.*, 1994; *Carbotte et al.*, 1997; *Hooft et al.*, 1997) and at the intermediate spreading Juan de Fuca Ridge are ∼250-350 m (*Canales et al.*, 2005). Approaching the propagating tip of the CLSC, however, the on-axis layer 2A thicknesses of ∼ 500-600 m are more similar to the off-axis 2A thicknesses at these other spreading systems.

These prior studies are from mid-segments at their respective spreading systems and are thus most likely undergoing relatively robust and steady-state spreading compared to segment ends or overlapping spreading centers (OSCs). Mid-segment crustal accretion most likely occurs by focused, symmetric diking that splits previous dikes and vertical isostatic compensation that preserves the individual crustal layers (Figure 4.9a) (*Cann*, 1974). Non-transform discontinuity OSCs and spreading segment ends, on the other hand, represent a part of the ridge segment where magmatism is thought to wane (*Macdonald et al.*, 1988). Layer 2A exhibits greater thickness variability at OSCs (*Bazin et al.*, 2001) than along EPR mid-segments (*Kent et al.*, 1994; *Carbotte et al.*, 1997) or along lines 7a and 7b in this study. Studies show OSC migration causes thickening of 2A at the southern (*Bazin et al.*, 1998) and northern (*Christeson et al.*, 1997) EPR and at the Valu Fa Ridge (*Day et al.*, 2001) in the Lau Basin. Line 7c, at the segment end, likewise has greater thickness reaching values comparable to layer 2A thicknesses at OSCs. Thus, the propagating tip at the CLSC is likely under similar conditions to OSCs and ridge segment ends.

Various mechanisms may be taking place in regions such as propagating ridges and OSCs that may cause a thickening of layer 2A. Propagation of a spreading center could cause a high degree of fracturing within the crust surrounding the propagating tip, as observed at Hess Deep (*Karson et al.*, 2002). This would reduce layer 2A velocities or cause layer 2A to appear thickened if the fracturing

persists to levels deeper than a few hundred meters subsurface. Thus, fracturing associated with propagation and extensional forces is a possible factor affecting the thickness or apparent thickness of layer 2A near the propagating tip. However, another interpretation for the thickening of layer 2A is diffuse diking leading to the gradual building of the extrusive pile (*Cann*, 1974; *Kidd*, 1977; *Hooft et al.*, 1996). This hypothesis is supported by submersible measurements of the thickness of extrusive outcrops at areas of complicated accretionary mechanisms, such as at Hess Deep (*Rivizzigno and Karson*, 1999; *Karson et al.*, 2002). These outcrops may have formed in an area of low magma supply such as a spreading center segment end (*Lonsdale*, 1985; *Macdonald et al.*, 1988) or been affected by ridge propagation (e.g. *Francheteau et al.*, 1990), and may thus be analogous to the crustal structure at line 7c of the CLSC.

4.5.2 Magmatic Implications for Accretion near the Propagating Tip

The change in upper crustal structure as the propagating tip is approached (Figures 4.4 and 4.6) suggests that a different crustal formation method is taking place in this region. Some combination of extension and accretion is occurring at the propagator that causes a thickened layer 2A, a relaxed gradient in the layer 2A/2B transition zone, and a deepening and velocity reduction in layer 2B. These crustal properties and formation mechanism are distinct from the crust north of the neovolcanic axial tip which has a structure similar to the mid-segment of an intermediate to fast spreading ridge (Figure 4.9a).

Cann (1974), *Kidd* (1977), and *Hooft et al.* (1996) describe an accretionary mechanism that accounts for ophiolite observations of an extended transition between pillow lavas and sheeted dikes and an imbalance in dike chilling directions within the sheeted dike complex. In the models, diking concentrated exactly at the axis would always split the previous dike and create a clean contact between the two layers. Conversely, diking that occurs randomly within the area of injection causes an intermixing of dikes with the more porous pillow lavas (*Karson et al.*, 2002) as dikes are buried by subsequent lava flows (Figure 4.9b). This leads to a

thickened layer 2A as lavas spread out from the point of eruption and cover other flows. This accretionary mechanism is especially associated with a lower velocity gradient within the 2A/2B transition zone causing an overall thickened vertical velocity transition region, because dikes and pillows are intermingled within this range rather than it consisting of purely higher-velocity dikes.

This mechanism is proposed by *Cann* (1974), *Kidd* (1977), and *Hooft et al.* (1996) as an across-axis phenomena, but can also occur along axis where magma supply becomes limited. Indeed, *Karson et al.* (2002) find at Hess Deep that dike swarms that penetrate the overlying volcanic layer are more persistent in the along axis direction. This is likely occurring at the CLSC propagating tip where the tomographic models and reflection sections both agree that the AMC has died out (Figure 4.7) and is likely no longer steadily feeding a neovolcanic zone. Periodic, lateral (non-vertical) diking (e.g. *Karson et al.*, 2002) probably acts to build a thick layer 2A and transition zone south of the AMC reflector until the bathymetrically defined propagating ridge tip is reached. The cross-cutting dikes also likely cause intense fracturing of pre-existing material, reducing 2A and transition zone velocities (*Karson et al.*, 2002). The thickened and reduced-velocity-gradient transition zone causes a lack of definition in the base of layer 2A, which in turn does not provide enough of a velocity gradient to produce a visible 2A reflector, as observed in the line 7c reflection section where the layer 2A reflector dies out (Figure 4.7). As the propagating tip is approached, it is unlcear how much of the crust right at the propagator is new and not simply a slight modification of the preexisting crust. It is obvious that rift propagation modifies the crust at least slightly, but perhaps does not form new crust completely. Part of the uncertainty arises from the fact that the crust that is being propagated into is originally very slow with low gradients.

This mechanism of diffuse emplacement of dikes and vertical build-up of pillow flows most likely transitions into a regime of more focused dike injection and uniform crustal accretion as the neovolcanic zone, tracking behind the propagating rift tip, is established. At the CLSC propagator, the initiation of 2A thickening is located vertically above the tip of the AMC reflector before it dies out. This

suggests that where an AMC exists, typical oceanic upper crustal structure is constructed with a few hundred meter thick layer 2A underlain by a high-velocity-gradient transition zone, and then by layer 2B.

4.5.3 Correlation of Layer 2A with Axial Magma Chamber Depth

Along the majority of the axis (lines 7a and 7b), the upper crustal layer 2A is relatively constant thickness (Figure 4.4), although a subtle segmentation is noticeable at approximately 18°44′S where layer 2A thickens slightly. In addition to this, the zero-offset stacked reflection sections, overlain on the tomographic models (Figure 4.10), show a discontinuous AMC reflector that varies in depth by a few hundred meters along this ∼100 km long section of seismic profile. The layer 2A structure along axis and the discontinuous nature of the AMC suggests that the CLSC can be subdivided into two major segments with the division occurring somewhat north of the bend in the ridge and close to the full rate ridge tip (FRT) defined by *Wiedicke and Habler* (1993).

At 18°45′S to 18°48′S (x = 84-90 km in model space, Figures 4.4 and 4.10), there is a small (∼100 m) thickening of 2A in the tomographic model that does not directly correspond with a deepening of the AMC. The AMC at this location actually shoals (Figures 4.4 and 4.10) as layer 2A remains thickened. The FRT of the propagating system as defined by *Wiedicke and Habler* (1993) is near this location as shown in Figures 4.4 and 4.10. It is possible that the slight deviation in upper crustal structure is associated with the transition to less than full rate spreading. Also in this location, the character of the seismic data changes such that an additional few hundred meters of structure are imaged at the base of our coverage. This can be determined as the location where layer 2B begins to decrease in velocity leading to a large velocity gradient, thus allowing rays to turn deeper within the structure. These properties are correlated with the reappearance of an AMC reflector after a short hiatus.

4.5.4 Across-Axis Upper Crustal Structure

Aging of Crust

Observable expressions of aging generally take place within layer 2A very rapidly after the newly formed crust moves away from the axis. *Carlson* (1998) notes that seismic velocity increase associated with aging of the upper crust takes place within the first 10 Myr, after which velocities remain relatively unchanged. Crustal velocities at ages less than 1 Ma are typically below 3 km/s, increasing to a range between 2-5 km/s within the first 5 Ma. Based on these values, it is implied that the average velocity for crust of a given age increases from its starting velocity value by 0.33 km/s per Ma. In addition to seismic velocity increase, overall thickening of layer 2A can occur immediately off-axis due to off-axis volcanism and lateral magma transport to the flanks of the ridge (*Perfit et al.*, 1994; *Canales et al.*, 2012). At the CLSC, four across-axis seismic profiles provide the potential for aging analysis of: 1) crust formed at the CLSC propagator, and 2) crust formed at the CLSC that is juxtaposed across the traces of the pseudofaults next to older crust formed at the ELSC.

A modest thickening of layer 2A velocities is observed directly adjacent to the ridge as the crust moves off axis along lines 10, 12a, and 12b (Figure 4.5). The thickening, illustrated by the line 12b 1D profiles of Figure 4.8b, indicates a robust accretionary mechanism with sufficient magma to supply some off-axis lateral dikes that build the crust outside the axis or large enough lava flows that overflow the edges of the axis depositing extrusives on the flanks. Vertical velocity profiles for both on- and off-axis regions show a more than doubly thickened layer 2A between the two regions of line 12b. Line 14 however, crossing the axis near the tip of the propagator, comprises laterally homogeneous crustal structure directly at the axis and on the flanks (Figure 4.8c). Figure 4.8c illustrates the velocity probability density distribution for nearly all of line 14, which shows a very similar velocity structure to the average velocity of the northern Valu Fa Ridge (dashed gray line; *Jacobs et al.* (2007)). This provides further evidence that the southernmost portion of the propagator functions under a different accretionary mechanism than the majority of the axis.

Aside from crustal thickening with age, an increase in layer 2A velocity is expected and would indicate normal aging processes such as hydrothermal infilling of fractures (*Harding et al.*, 1989; *Vera et al.*, 1990). This type of aging, shown diagrammatically in Figure 4.11b, is not observed in our profiles. One explanation is that the maximum age differential along our across-axis profiles is not sufficient to resolve such aging processes. Even if the oldest crust observed along the across-axis profiles is too young to distinguish age-related changes in seismic velocity, the velocity differences between CLSC-formed crust and the older ELSC-formed crust into which the CLSC propagated ought to be observably distinct across the trace of the pseudofaults, as illustrated by the cartoon in Figure 4.11c.

Based on magnetic chrons determined by *Parson and Hawkins* (1994), the ELSC crust adjacent to the western pseudofault is of age ∼1.7 Ma or older, representing a relative increase in velocity of ∼0.6 km/s from its initial value. The average crustal age-velocity relationship of *Carlson* (2004) would predict a layer 2A seismic velocity of 3.4-3.5 km/s for crust of this age. Layer 2A velocities at the CLSC axis in this study are < 3 km/s. Therefore, a horizontal gradient would be expected in the models as very young CLSC crustal layer 2A (< 3 km/s) transitions to ∼1.7 Ma ELSC crustal layer 2A (∼3.5 km/s) across a zone representative of the pseudofault between the two crustal types (Figure 4.11c). As observed in the across-axis models (Figure 4.5) with pseudofault traces represented by vertical solid black lines (*Wiedicke and Habler*, 1993) and dashed black (redfined for this study), neither this type of lateral gradient, horizontal juxtaposition of two different seismic velocities, nor shoaling of higher velocities are distinguishable in the data.

Nedimović et al. (2008) conducted a study at the intermediate-spreading-rate Juan de Fuca Ridge (JdF) that reveals an effect of sedimentation of the ridge flank on the age-velocity relationship. Augmenting the dataset of *Carlson* (1998, 2004) with data entirely from intermediate spreading rates, his study shows that velocities increase more rapidly with increased sediment cover. Ridge flanks with little or no sedimentation increase very little in velocity in the first 5 Ma: ∼0.1 km/s per Ma. *Nedimović et al.* (2008) fit the age-velocity data with a linear

regression curve, showing that the increase in velocity with age, especially at young ages, is more gradual than initially assessed by *Carlson* (2004). As shown by high reflectivity in the seafloor backscatter plot (Figure 4.2b), the locations of the across-axis profiles are in areas of very low sedimentation. Based on the above aging-velocity relationship for low sediment cover, the velocities at ∼1.7 Ma are actually expected to be around 2.7-2.8 km/s, similar to the velocities of the newest crust.

There may be additional factors, besides sedimentation, that affect the age-velocity relationship. The ∼ 1.7 Ma ELSC crust that is being cut into has a more felsic composition, similar to the present VFR, than the crust analyzed in the age-velocity studies. Velocities of rocks with felsic compositions may evolve differently with aging than their mafic counterparts, and may have initially lower velocities to begin with, affecting their absolute velocity values (*Jacobs et al.*, 2007). The above are explanations for why our results do not show the lateral change in the velocity structure expected between newly formed crust and sedimented crust of age ∼1.7 Ma.

Finally, these across-axis lines have the potential to confirm the distinct accretionary mechanism associated with a propagating tip and discussed above. The thickening of layer 2A and the relaxation of the 2A/2B transition zone visible in along-axis profile 7c is taken as the signature of the diffuse diking and interspersed dike and extrusive accretionary mechanism associated with the initiation of propagation (Figure 4.9b). Thus, this distinct seismic velocity structure should exist everywhere along the inner side of the pseudofault wakes as they are spread away from the axis. Therefore, an even more distinct transition should exist between the two crusts on either side of the pseudofault (Figure 4.11d). Similar to the previously discussed aging properties, this signature of the earliest propagating accretionary mechanism is not visible in the models.

Crustal Structure in the Context of Ridge Jumps

The unusual structure of line 10 (Figure 4.5) may represent three different crustal types within a ∼25 km wide across-axis section. The three regimes are

defined as follows: x = -10 to -4.5 km (type 10A); -4.5 to 4 km (type 10B); and x = 4 to 13 km (type 10C) (Figures 4.5 and 4.12). We interpret crustal type 10A as crust formed at an abandoned propagator, crustal type 10B as crust formed and currently forming at the (propagating) CLSC, and crustal type 10C as relict basin material. We suggest a complicated history of abandoned propagators and southeastward stepping propagating spreading systems based on a synthesis of this seismic velocity structure with magnetics and sidescan data, as well as on interpretation of the seafloor morphology.

Both crustal regimes 10A and 10B have velocities characteristic of layer 2B (> 4-5 km/s) reaching shallow levels (∼400 m subsurface). Based on our along-axis results, this seismic structure suggests that they were formed at a spreading location with an AMC. Crust 10A, present in a linear basin whose morphology is reminiscent of a spreading axis, exhibits the thinnest layer 2A at approximately x = -7.5 km (line 10, Figure 4.5), which thickens to each side in the characteristic fashion of crustal thickening off-axis. This suggests that this location in crust 10A is a location of former spreading, which is now abandoned.

A series of *en echelon* basins with strikes parallel to the CLSC step away from the current axis to the northwest, between latitudes 17°40′S and 18°55′S. These are noted on Figure 4.2a as the western basins. The linear morphology of these basins suggests that they may have once been the location of active axis propagation and were progressively abandoned as the spreading center jumped southeastward until it reached its present location at the CLSC. If this is the case, crust 10A was likely formed at the spreading center when the axis of spreading was one basin west of where it is today. As that spreading center was abandoned, spreading localized at the present CLSC where crust 10B was beginning to be created, and is currently robustly being formed. This is supported by backscatter observations, showing that these western basins and the CLSC are unsedimented (Figure 4.2b), and by magnetic data that show they are made of young crust with normal polarity magnetization (Figure 4.2c).

Crust 10C, on the other hand, has a velocity structure more akin to that of line 14, which we have interpreted as older crust that has been tectonically

extended and possibly has some surficial lava flows originating from the north where magmatism is more robust. Evidence that this crust 10C is older comes from the magnetic data, which indicate a minimum age of 1.7 Ma (Figure 4.2c). Backscatter reveals low levels of sedimentation (Figure 4.2b), suggesting that some recent thin flows cover parts of the surface of the basin, probably as overflow from the present CLSC. Thus, 10C crust was probably initially rifted as 10A (or crust at even earlier spreading ridges) was forming at a prior locus of spreading to the northwest of the present axis. Subsequently, rifting and repaving have continued within 10C crust as the current CLSC forms crust 10B. This history leads to a structure for line 10 where the western two-thirds of the line is/was created by magmatic accretion, while the eastern third is older crust altered primarily by extension with some surface magmatism.

Also in favor of this juxtaposed crustal types argument, are the base-of-layer 2A reflections from the stacked MCS sections of the across-axis lines (line 10 shown in Figure 4.12). Due to the nature of the tomographic inversion and the *a priori* assumption of lateral continuity, changes in crustal layering are smoothed horizontally in the final models. Therefore, abrupt vertical offsets in crustal layering are unlikely to be obtained in the refraction tomographic results. On the other hand, stacked reflection sections show a break and vertical displacement of the layer 2A reflector across the traces of our newly defined pseudofaults (Figure 4.5, dashed black lines, and Figure 4.12) indicating crustal differences and/or faulting. As discussed in the previous section, vertical velocity profiles taken on- and off-axis along profiles 10 and 12b, also reveal distinct crustal types (Figure 4.8a,b). Thus, while we see no abrupt horizontal gradient in the tomography (e.g. Figure 4.11), the vertical velocity profiles and 2A reflections reveal a fundamental difference between crust formed on the outside and inside of our preferred pseudofaults, along lines 12a and 12b, and to the east on line 10.

Crust 10C is further distinguishable from its western counterparts as it has no layer 2A reflector (Figure 4.12). This is consistent with a thickened layer 2A and a diffuse layer 2A/2B transition zone with a low velocity gradient.

The bathymetry of the area reveals a north-south fabric (strike $\sim 178°$,

Parson et al., 1990) in the seafloor to the west of the CLSC propagating tip (*Zellmer and Taylor*, 2001). The orientation of the propagator is NNE-SSW along the flanks of the western basins (north of latitude 18°52′S), until it encounters this N-S fabric where it bends to align. It is undetermined whether this alignment with the north-south fabric will cause a successful take-over by the present CLSC, or if it will, in turn, be abandoned in favor of a more eastern locus of spreading similar to its predecessors.

Parson et al. (1990) suggest that an arc-ward ridge migration may be necessary in order to keep the ridge within a threshold distance of subduction-induced convection leading to mantle upwelling. While the CLSC does not have signatures of subduction influence, it is still possible that spreading in a backarc must maintain a certain proximity to the arc to continue operating. We suspect that the southeastward jumps of the spreading segments to form the western basins, as well as the left-stepping *en echelon* extensional segments in the Lau Extensional Transform Zone (LETZ of *Taylor et al.* (1994, 1996)) are thusly oriented due to far-field extensional forces between the Niuafo'ou microplate and the Australian plate (*Zellmer and Taylor*, 2001).

4.6 Conclusion

The CLSC is a useful location for studying the crustal structure and accretionary mechanisms associated with a propagating rift. Results from along axis seismic profiles indicate that structure consisting of relatively constant thickness layer 2A with a high gradient underlying layer 2A/2B transition zone persists until approximately 15 km from the tectonic tip of the propagator. Within these last 15 km, in association with the truncation of the AMC and layer 2A reflectors, crustal layer 2A thickens to 600 m and the 2A/2B transition zone relaxes and thickens to the base of ray coverage. This change in structure is likely due to a transition in accretionary mechanism from focused, central diking to more random emplacement of dikes and the intermixing of dikes with extrusive lavas. We propose that as the neovolcanic tip of the propagator passes through a region, a more organized

accretionary mechanism takes over.

Analysis of available across-axis profiles provides little insight into the effects of pseudofaults passing through the structure, normal crustal aging due to hydrothermal infilling of cracks and pore spaces, or the preservation of structure associated with the diffuse-diking accretionary mechanism in the crust adjacent to the pseudofaults. Additional studies are warranted in this area to further investigate these across-axis properties. Full waveform inversion may clarify the structure and bring out some of the expected features, but further seismic analysis is currently limited by the lengths of the existing across-axis profiles.

Acknowledgments

Chapter 4, in part, is currently being prepared for submission of the material. Henig, A. S., A. J. Harding. The dissertation author was the primary investigator and author of this paper.

References

Arnulf, A., S. Singh, A. Harding, G. Kent, and W. Crawford (2011), Strong seismic heterogeneity in layer 2a near hydrothermal vents at the mid-atlantic ridge, *Geophysical Research Letters*, *38*(13), L13,320, doi:10.1029/2011GL047753.

Arnulf, A., A. Harding, S. Singh, G. Kent, and W. Crawford (2012), Fine-scale velocity structure of upper oceanic crust from full waveform inversion of downward continued seismic reflection data at the lucky strike volcano, mid-atlantic ridge, *Geophysical Research Letters*, *39*(8), L08,303, doi:10.1029/2012GL051064.

Bazin, S., H. Van Avendonk, A. Harding, J. Orcutt, J. Canales, R. Detrick, and MELT Group (1998), Crustal structure of the flanks of the east pacific rise: Implications for overlapping spreading centers, *Geophysical research letters*, *25*(12), 2213–2216.

Bazin, S., A. J. Harding, G. M. Kent, J. A. Orcutt, C. H. Tong, J. W. Pye, S. C. Singh, P. J. Barton, M. C. Sinha, R. S. White, R. W. Hobbs, and H. J. A. Van Avendonk. (2001), Three-dimensional shallow crustal emplacement at the 9°03' n overlapping spreading center on the east pacific rise: Correlations between magnetization and tomographic images, *Journal of geophysical research*, *106*(B8), 16–101.

Canales, J., R. Detrick, S. Carbotte, G. Kent, J. Diebold, A. Harding, J. Babcock, M. Nedimovic, and E. Van Ark (2005), Upper crustal structure and axial topography at intermediate spreading ridges: Seismic constraints from the southern juan de fuca ridge, *J. Geophys. Res*, *110*, B12,104, doi:10.1029/2005JB003630.

Canales, J., H. Carton, J. Mutter, A. Harding, S. Carbotte, and M. Nedimovic (2012), Recent advances in multichannel seismic imaging for academic research in deep oceanic environments, doi:10.5670/oceanog.2012.09.

Cann, J. (1974), A model for oceanic crustal structure developed, *Geophysical Journal of the Royal Astronomical Society*, *39*(1), 169–187, doi:10.1111/j.1365-246X.1974.tb05446.x.

Carbotte, S., J. Mutter, and L. Xu (1997), Contribution of volcanism and tectonism to axial and flank morphology of the southern east pacific rise, 17° 10'–17°40' s, from a study of layer 2a geometry, *Journal of geophysical research*, *102*(B5), 10,165–10.

Carlson, R. (1998), Seismic velocities in the uppermost oceanic crust: Age dependence and the fate of layer 2a, *Journal of geophysical research*, *103*(B4), 7069–7077.

Carlson, R. (2004), Seismic properties of layer 2a at 11 ma: Results of a vertical seismic profile at ocean drilling program site 1243, *Geophysical research letters*, *31*(17), L17,601, doi:10.1029/2004GL020598.

Christeson, G., P. Shaw, and J. Garmany (1997), Shear and compressional wave structure of the east pacific rise, 9°–10° n, *Journal of geophysical research*, *102*(B4), 7821–7835.

Christeson, G., K. McIntosh, and J. Karson (2007), Inconsistent correlation of seismic layer 2a and lava layer thickness in oceanic crust, *Nature*, *445*(7126), 418–421, doi:10.1038/nature05517.

Day, A., C. Peirce, and M. Sinha (2001), Three-dimensional crustal structure and magma chamber geometry at the intermediate-spreading, back-arc valu fa ridge, lau basin?results of a wide-angle seismic tomographic inversion, *Geophysical Journal International*, *146*(1), 31–52.

Detrick, R., A. Harding, G. Kent, J. Orcutt, J. Mutter, and P. Buhl (1993), Seismic structure of the southern east pacific rise, *Science*, *259*, 499–503, doi: 10.1126/science.259.5094.499.

Dunn, R., and F. Martinez (2011), Contrasting crustal production and rapid mantle transitions beneath back-arc ridges, *Nature*, *469*(7329), 198–202, doi: 10.1038/nature09690.

Escrig, S., A. Bézos, S. Goldstein, C. Langmuir, and P. Michael (2009), Mantle source variations beneath the eastern lau spreading center and the nature of subduction components in the lau basin–tonga arc system, *Geochemistry Geophysics Geosystems*, *10*(4), Q04,014, doi:10.1029/2008GC002281.

Francheteau, J., R. Armijo, J. Cheminee, R. Hekinian, P. Lonsdale, and N. Blum (1990), 1 ma east pacific rise oceanic crust and uppermost mantle exposed by rifting in hess deep (equatorial pacific ocean), *Earth and Planetary Science Letters*, *101*(2), 281–295.

Grevemeyer, I., and W. Weigel (1996), Seismic velocities of the uppermost igneous crust versus age, *Geophysical Journal International*, *124*(2), 631–635.

Grevemeyer, I., and W. Weigel (1997), Increase of seismic velocities in upper oceanic crust: The "superfast" spreading east pacific rise at 14°14's, *Geophysical research letters*, *24*(3), 217–220.

Hamburger, M., and B. Isacks (1988), Diffuse back-arc deformation in the southwestern pacific, *Nature*, *332*(6165), 599–604, doi:10.1038/332599a0.

Harding, A., J. Orcutt, M. Kappus, E. Vera, J. Mutter, P. Buhl, R. Detrick, and T. Brocher (1989), Structure of young oceanic crust at 13°n on the east pacific rise from expanding spread profiles, *Journal of Geophysical Research*, *94*(B9), 12,163–12.

Harding, A., G. Kent, and J. Orcutt (1993), A multichannel seismic investigation of upper crustal structure at 9°n on the east pacific rise: Implications for crustal accretion, *Journal of Geophysical Research*, *98*(B8), 13,925–13, doi: 10.1029/93JB00886.

Harding, A., G. Kent, D. Blackman, S. Singh, and J. Canales (2007), A new method for mcs refraction data analysis of the uppermost section at a mid-atlantic ridge core complex, in *Eos, Trans. Am. Geophys. Union*, vol. 88, pp. S12A–03 (Abstract).

Hawkins, J. (1995), Evolution of the lau basin: Insights from odp leg 135, *Geophysical Monograph Series*, *88*, 125–173, doi:10.1029/GM088p0125.

Hawkins, J., L. Parson, and J. Allan (1994), Introduction to the scientific results of leg 135: Lau basin-tonga ridge drilling transect, *135*, 3–5.

Henig, A., D. Blackman, A. Harding, J. Canales, and G. Kent (2012), Downward continued multichannel seismic refraction analysis of atlantis massif oceanic core complex, 30°n, mid-atlantic ridge, *Geochemistry Geophysics Geosystems*, *13*(null), Q0AG07, doi:10.1029/2012GC004059.

Hey, R. (1977), A new class of "pseudofaults" and their bearing on plate tectonics: a propagating rift model, *Earth and Planetary Science Letters*, *37*(2), 321–325.

Hey, R., F. Duennebier, and W. Morgan (1980), Propagating rifts on mid-docean ridges, *Journal of Geophysical Research*, *85*(B7), 3647–3658, doi: 10.1029/JB085iB07p03647.

Hooft, E., H. Schouten, and R. Detrick (1996), Constraining crustal emplacement processes from the variation in seismic layer 2a thickness at the east pacific rise, *Earth and planetary science letters*, *142*(3), 289–309.

Hooft, E., R. Detrick, and G. Kent (1997), Seismic structure and indicators of magma budget along the southern east pacific rise, *Journal of Geophysical Research*, *102*(B12), 27,319–27.

Houtz, R., and J. Ewing (1976), Upper crustal structure as a function of plate age, *Journal of Geophysical Research*, *81*(14), 2490–2498.

Hussenoeder, S., M. Tivey, H. Schouten, and R. Searle (1996), Near-bottom magnetic survey of the mid-atlantic ridge axis, 24°–24° 40' n: Implications for crustal

accretion at slow spreading ridges, *Journal of geophysical research*, *101*(B10), 22,051–22.

Jacobs, A., A. Harding, and G. Kent (2007), Axial crustal structure of the lau back-arc basin from velocity modeling of multichannel seismic data, *Earth and Planetary Science Letters*, *259*(3), 239–255, doi:10.1016/j.epsl.2007.04.021.

Karson, J., E. M. Klein, S. D. Hurst, C. E. Lee, P. A. Rivizzigno, D. Curewitz, A. R. Morris, D. J. Miller, R. G. Varga, G. L. Christeson, B. Cushman, J. M. O?Neill, J. G. Brophy, K. M. Gillis, M. A. Stewart, and A. L. Sutton (2002), Structure of uppermost fast-spread oceanic crust exposed at the hess deep rift: Implications for subaxial processes at the east pacific rise, *Geochemistry Geophysics Geosystems*, *3*(1), 1002, doi:10.1029/2001GC000155.

Kent, G., A. Harding, J. Orcutt, R. Detrick, J. Mutter, and P. Buhl (1994), Uniform accretion of oceanic crust south of the garrett transform at 14°15' s on the east pacific rise, *Journal of geophysical research*, *99*(B5), 9097–9116, doi: 10.1029/93JB02872.

Kidd, R. (1977), A model for the process of formation of the upper oceanic crust, *Geophysical Journal of the Royal Astronomical Society*, *50*(1), 149–183, doi: 10.1111/j.1365-246X.1977.tb01328.x.

Langmuir, C., A. Bézos, S. Escrig, and S. Parman (2006), Chemical systematics and hydrous melting of the mantle in back-arc basins, *GEOPHYSICAL MONOGRAPH-AMERICAN GEOPHYSICAL UNION*, *166*, 87.

Lawver, L., and J. Hawkins (1978), Diffuse magnetic anomalies in marginal basins: Their possible tectonic and petrologic significance, *Tectonophysics*, *45*(4), 323–339, doi:10.1016/0040-1951(78)90167-1.

Lawver, L., J. Hawkins, and J. Sclater (1976), Magnetic anomalies and crustal dilation in the lau basin, *Earth and planetary science letters*, *33*, 27–35.

Lonsdale, P. (1985), Nontransform offsets of the pacific-cocos plate boundary and their traces on the rise flank, *Geological Society of America Bulletin*, *96*(3), 313–327.

Macdonald, K., P. Fox, L. Perram, M. Eisen, R. Haymon, S. Miller, S. Carbotte, M. Cormier, and A. Shor (1988), A new view of the mid-ocean ridge from the behaviour of ridge-axis discontinuities, *Nature*, *335*(6187), 217–225.

Martinez, F., and B. Taylor (2002), Mantle wedge control on back-arc crustal accretion, *Nature*, *416*(6879), 417–420.

Martinez, F., B. Taylor, E. Baker, J. Resing, and S. Walker (2006), Opposing trends in crustal thickness and spreading rate along the back-arc eastern lau spreading center: Implications for controls on ridge morphology, faulting, and hydrothermal activity, *Earth and Planetary Science Letters*, *245*(3), 655–672, doi:10.1016/j.epsl.2006.03.049.

Nedimović, M., S. Carbotte, J. Diebold, A. Harding, J. Canales, and G. Kent (2008), Upper crustal evolution across the juan de fuca ridge flanks, *Geochemistry Geophysics Geosystems*, *9*(9), Q09,006.

Newman, K., M. Nedimović, J. Canales, and S. Carbotte (2011), Evolution of seismic layer 2b across the juan de fuca ridge from hydrophone streamer 2-d traveltime tomography, *Geochemistry Geophysics Geosystems*, *12*(5), Q05,009.

Parson, L., and J. Hawkins (1994), Two-stage ridge propagation and the geological history of the lau backarc basin.

Parson, L., J. Pearce, B. Murton, and R. Hodkinson (1990), Role of ridge jumps and ridge propagation in the tectonic evolution of the lau back-arc basin, southwest pacific, *Geology*, *18*(5), 470–473, doi:10.1130/?0091-7613(1990)?018¡0470:RORJAR¿?2.3.CO;2.

Pearce, J., M. Ernewein, S. Bloomer, L. Parson, B. Murton, and L. Johnson (1994), Geochemistry of lau basin volcanic rocks: influence of ridge segmentation and arc proximity, *Geological Society, London, Special Publications*, *81*(1), 53–75, doi:10.1144/GSL.SP.1994.081.01.04.

Penrose, Conference Participants. (1972), Penrose field conference on ophiolites, *Geotimes*, *17*, 24–25.

Perfit, M., D. Fornari, M. Smith, J. Bender, C. Langmuir, and R. Haymon (1994), Small-scale spatial and temporal variations in mid-ocean ridge crest magmatic processes, *Geology*, *22*(4), 375–379, doi:10.1130/0091-7613(1994)?022¡0375:SSSATV¿?2.3.CO;2.

Pratt, R. (1999), Seismic waveform inversion in the frequency domain i theory and verification in a physical scale model, *Geophysics*, *64*, 888–901.

Rivizzigno, P., and J. Karson (1999), Temporal variations in relative thickness of the extrusive and sheeted dike units in epr crust exposed at hess deep rift: Implications for models of upper crustal construction, *Eos Trans. AGU*, *80*, F984.

Shipp, R., and S. Singh (2002), Two-dimensional full wavefield inversion of wide-aperture marine seismic streamer data, *Geophysical Journal International*, *151*(2), 325–344.

Shtivelman, V., and A. Canning (1988), Datum correction by wave-equation extrapolation, *Geophysics*, *53*(10), 1311–1322, doi:10.1190/?1.1442409.

Taylor, B., K. Crook, and J. Sinton (1994), Extensional transform zones and oblique spreading centers, *Journal of Geophysical Research*, *99*(B10), 19,707–19.

Taylor, B., K. Zellmer, F. Martinez, and A. Goodliffe (1996), Sea-floor spreading in the lau back-arc basin, *Earth and Planetary Science Letters*, *144*(1), 35–40, doi:10.1016/0012-821X(96)00148-3.

Van Avendonk, H., D. Shillington, W. Holbrook, and M. Hornbach (2004), Inferring crustal structure in the aleutian island arc from a sparse wide-angle seismic data set, *Geochemistry, Geophysics, Geosystems*, *5*, Q08,008, doi:10.1029/2003GC000664.

Vera, E., J. Mutter, P. Buhl, J. Orcutt, A. Harding, M. Kappus, R. Detrick, and T. Brocher (1990), The structure of 0-to 0.2-my-old oceanic crust at 9°n on the east pacific rise from expanded spread profiles, *Journal of Geophysical Research*, *95*(B10), 15,529–15, doi:10.1029/JB095iB10p15529.

White, R., D. McKenzie, and R. O'Nions (1992), Oceanic crustal thickness from seismic measurements and rare earth element inversions, *Journal of Geophysical Research*, *97*(B13), 19,683–19,715, doi:10.1029/92JB01749.

Wiedicke, M., and W. Habler (1993), Morphotectonic characteristics of a propagating spreading system in the northern lau basin, *Journal of geophysical research*, *98*(B7), 11,783–11, doi:10.1029/93JB00707.

Wilkens, R., G. Fryer, and J. Karsten (1991), Evolution of porosity and seismic structure of upper oceanic crust: Importance of aspect ratios, *Journal of Geophysical Research*, *96*(B11), 17,981–17.

Zellmer, K., and B. Taylor (2001), A three-plate kinematic model for lau basin opening, *Geochem. Geophys. Geosyst*, *2*(5), 1020.

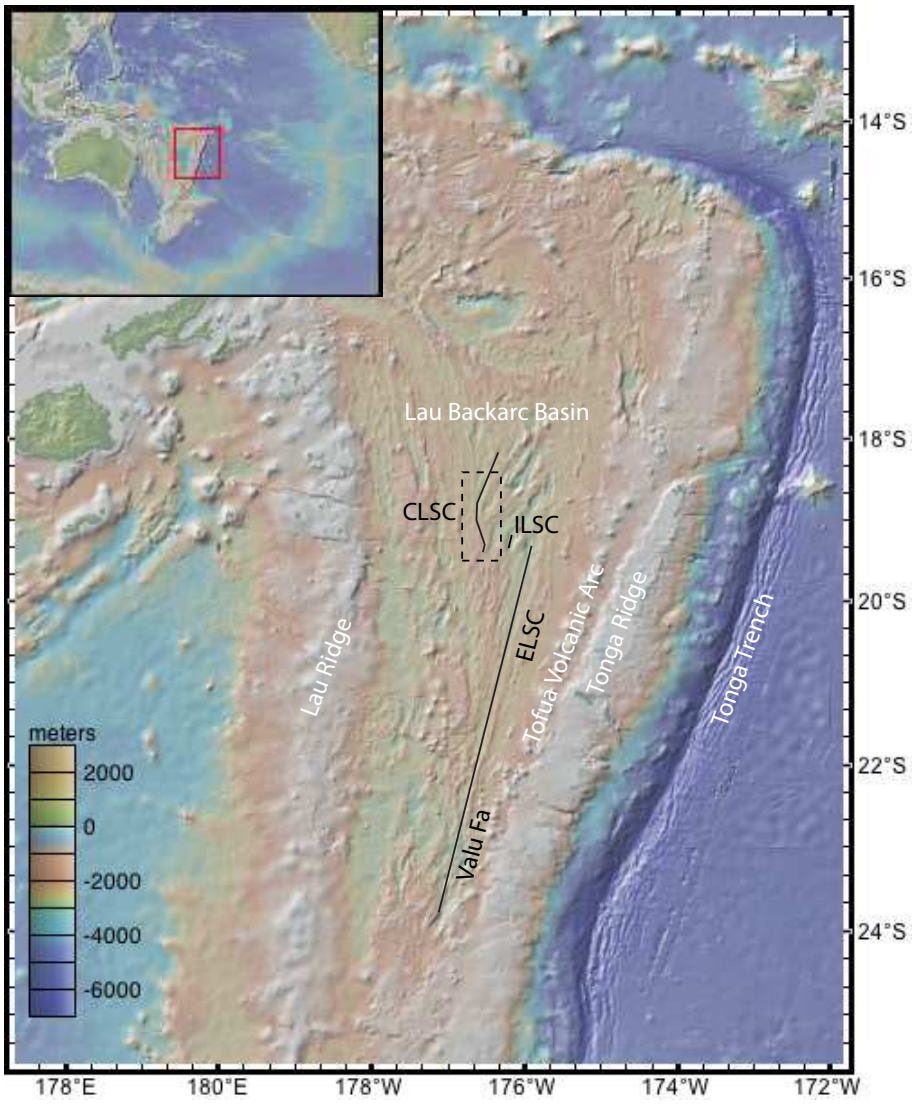

Figure 4.1: Map view of the Lau Backarc Basin and Tonga Trench. Lau Backarc Spreading Centers are illustrated by black lines. Dashed box represents approximate location of study area, shown in greater detail in Figures 4.2, 4.4, and 4.5

.

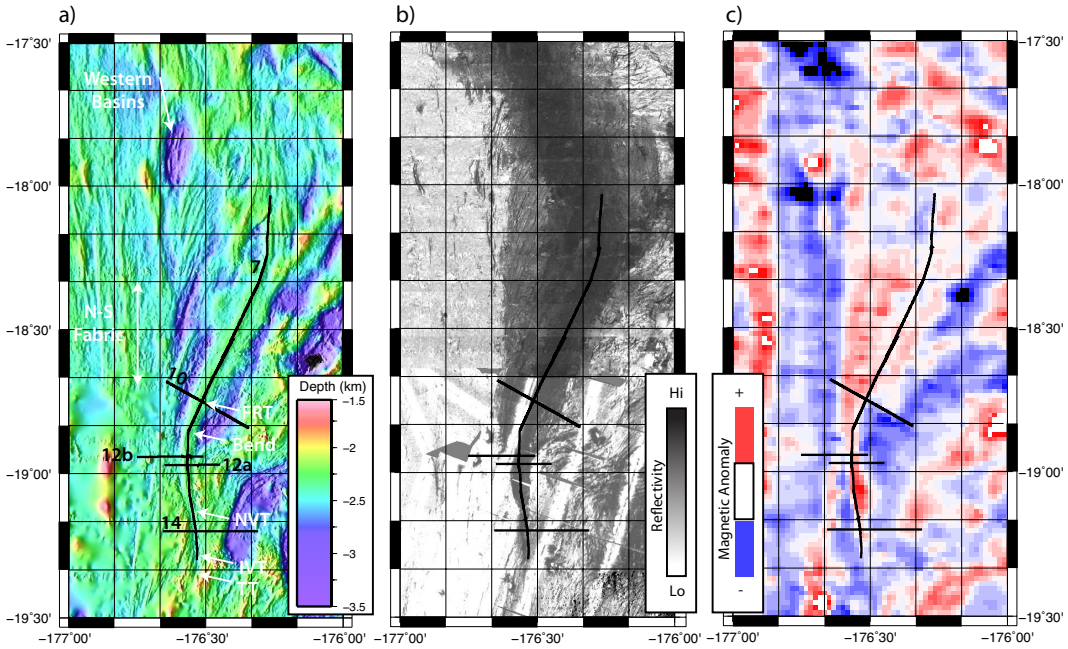

Figure 4.2: Central Lau Spreading Center region a) bathymetry, b) seafloor acoustic reflectivity, and c) magnetic anomalies. Locations of seismic profiles are noted by black lines. FRT - full rate tip; NVT - neovolcanic tip; IVT - initial volcanic tip; TT - tectonic tip. On acoustic reflectivity image (b), darker shades represent higher reflectivity. Positive magnetic anomaly indicated by red and negative anomaly by blue (c).

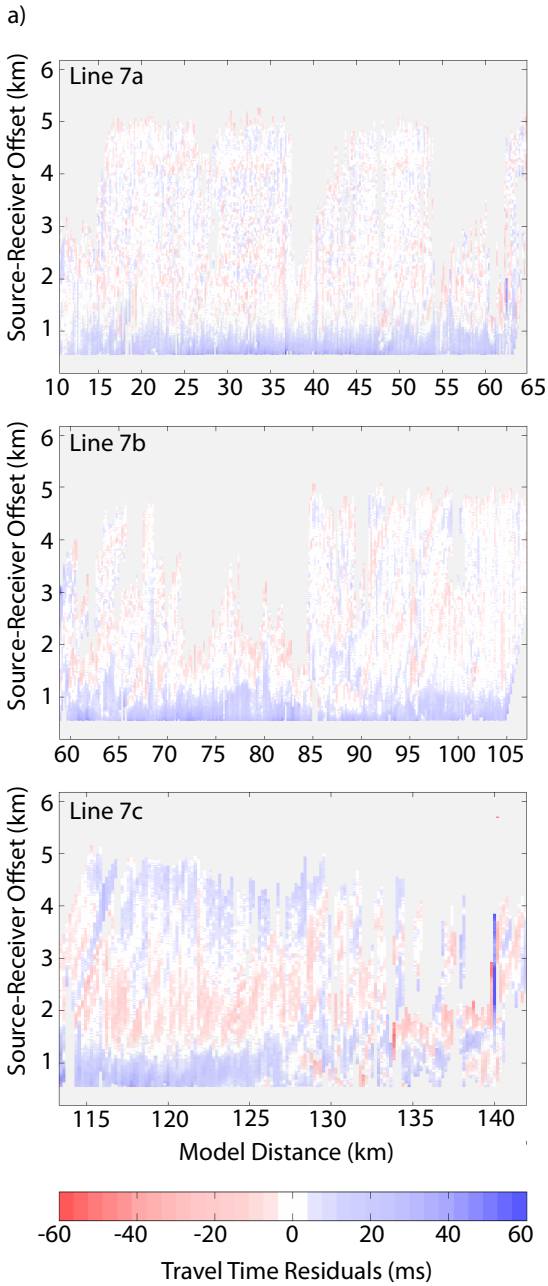

Figure 4.3: Travel time residuals of picks from a) along-axis seismic profiles, and b) across-axis seismic profiles, shown as a function of shot location and offset along streamer. Figure continued on following page.

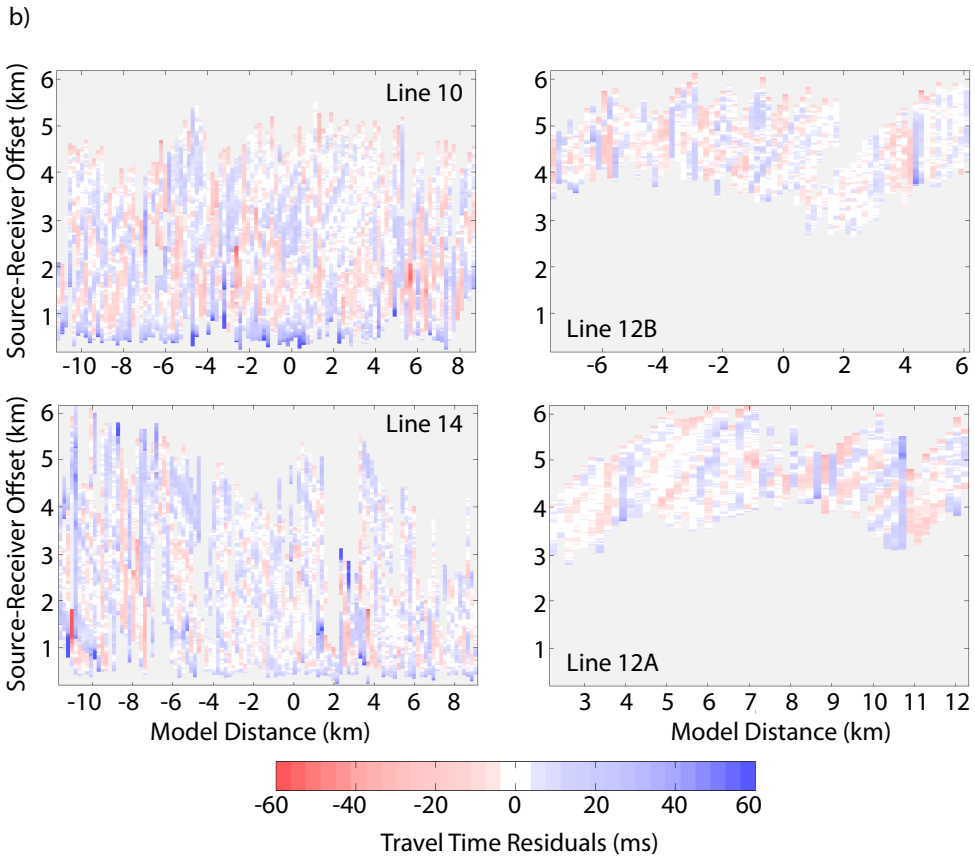

Figure 4.3: Figure continued from previous page. Travel time residuals of picks from a) along-axis seismic profiles, and b) across-axis seismic profiles, shown as a function of shot location and offset along streamer.

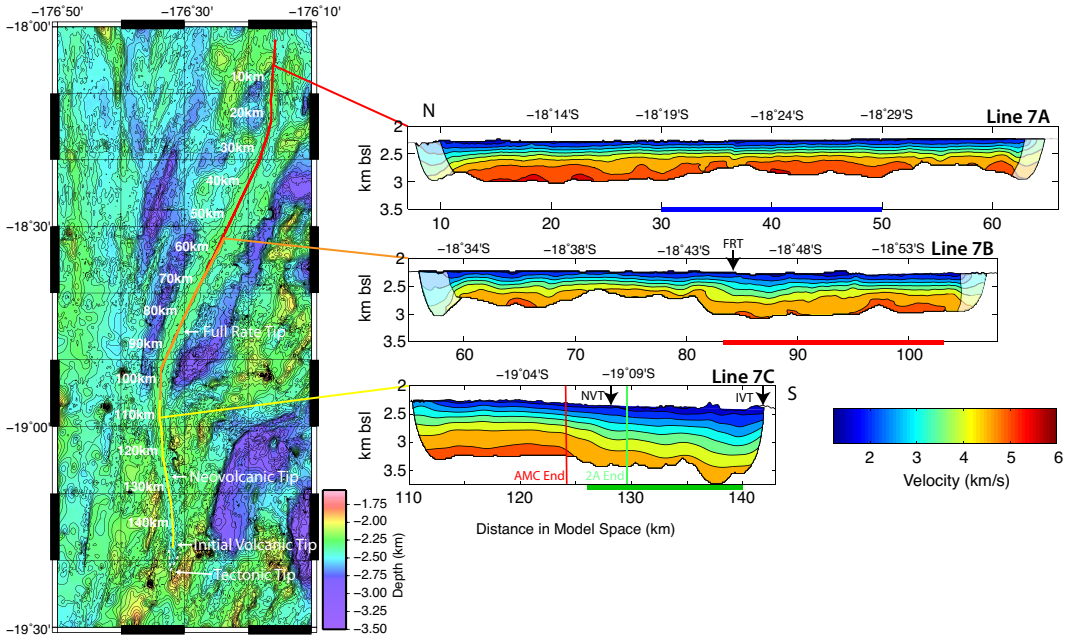

Figure 4.4: Tomographic velocity models of first refracted P-wave arrival from along-axis seismic profiles 7a, 7b, and 7c. Locations of profiles are shown on map at left, and annotated with distance and latitude along the profiles. Locations of the Full Rate Tip (FRT), Neovolcanic Tip (NVT), Initial Volcanic Tip (IVT), and Tectonic Tip of the CLSC propagator are indicated on the map and labeled as black arrows along the profiles. On Line 7c, the location of truncation of the AMC and layer 2A, based on reflection sections (Figure 8), is indicated by vertical red and green lines, respectively. Velocity color scale (1.2-6 km/s) is the same for all plots. Red, blue, and green bars at base of each profile correspond to locations of 1D profiles in Figure 4.6.

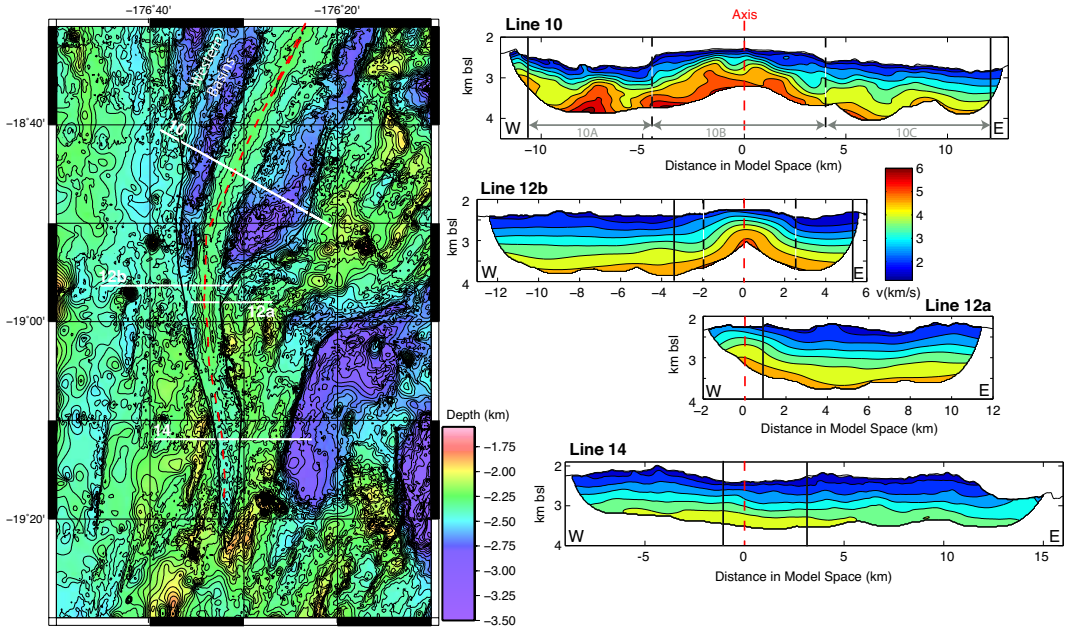

Figure 4.5: Tomographic velocity models of crustal P-wave arrivals from across-axis profiles shown by white lines in the map to the left. Velocity color scale is the same for all plots. A dashed red line indicates the location of the spreading axis in each profile. The black line on the map at left also shows the locations of pseudofaults as interpreted by *Wiedicke and Habler* (1993), while the dashed black line represents newly defined pseudofault locations from this study. The pseudofault crossings are also indicated on each profile by the vertical black and dashed black lines.

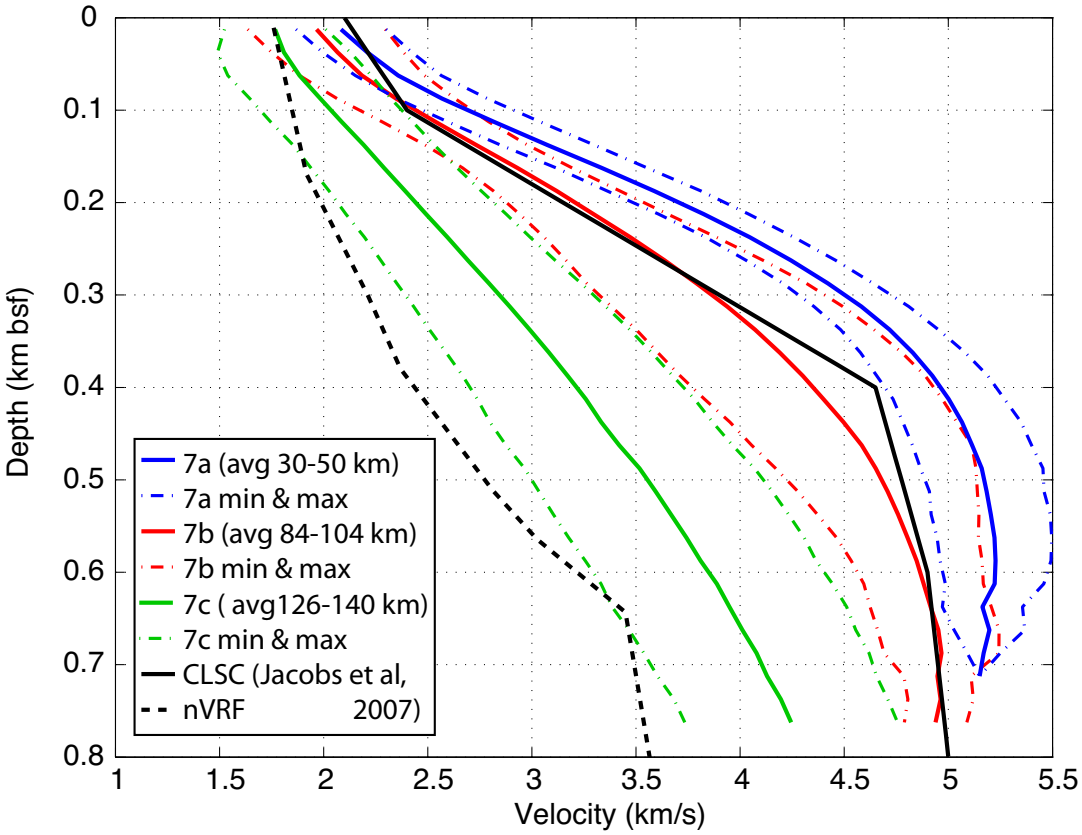

Figure 4.6: 1D vertical velocity profiles from selected regions of the along-axis lines. Averages for individual regions are shown along with the minimum and maximum velocity profile of each region. Location of each subset of profiles is indicated in the legend and in Figure 4 by red, blue, and green colored bars at the base of each profile. For comparison, the average 1D vertical velocity profiles from the CLSC and north Valu Fa Ridge (*Jacobs et al.*, 2007) are shown, respectively, in solid and dashed black.

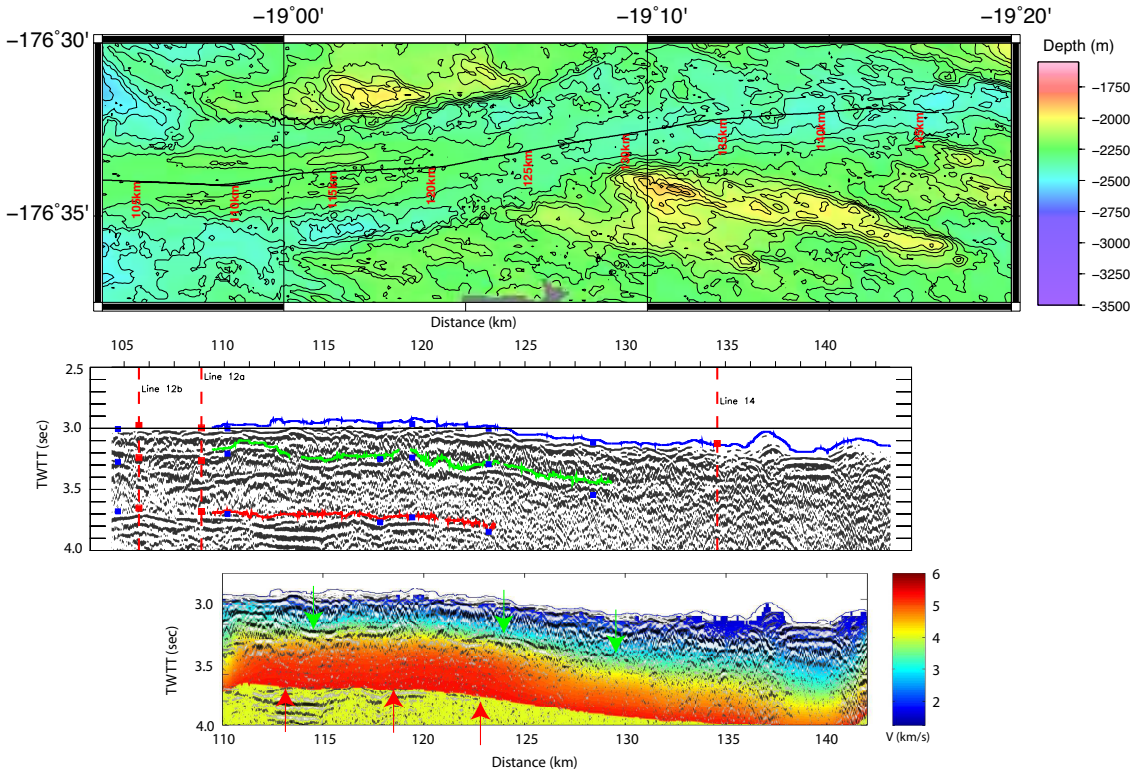

Figure 4.7: Local bathymetry (top panel, contour interval 50 m), zero-offset stacked reflection section (middle), and composite image of zero-offset stacked reflection overlain by the tomography (bottom) represented in two-way travel time. Middle panel shows seafloor reflection (blue line), base of layer 2A reflection (green line), and AMC reflection (red line). Vertical red dashed lines show the locations of profile 12a, 12b, and 14 crossings. Blue squares on middle panel indicate nodes used by *Jacobs et al.* (2007) to compute vertical velocity profiles.

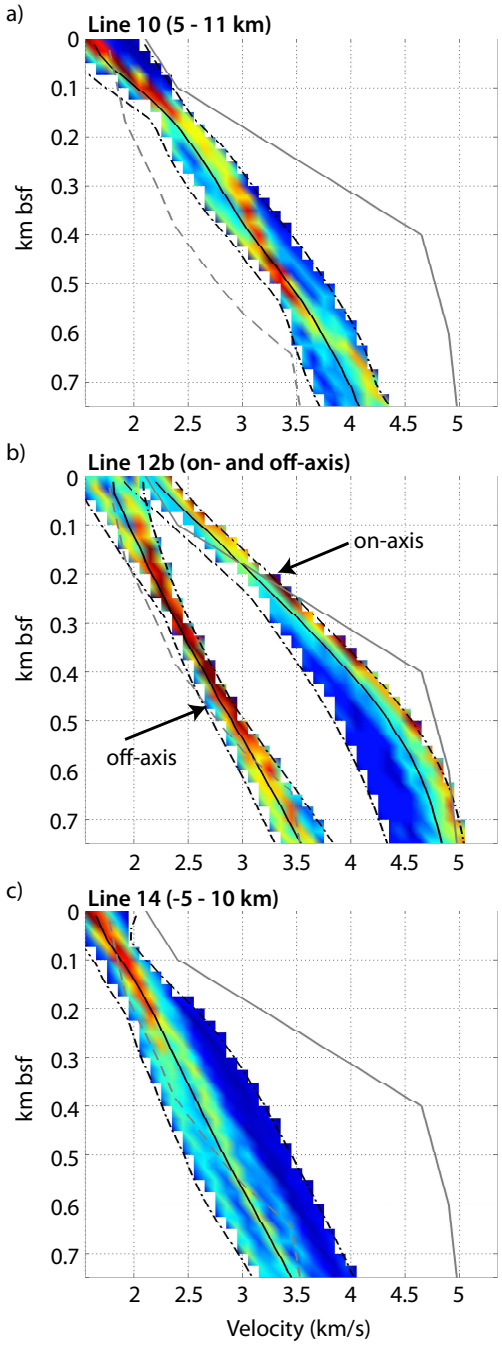

Figure 4.8: 1D vertical velocity profiles of the across-axis lines a) 10, b) 12b, and c) 14, represented by the velocity probability distribution for the regions listed. Red indicates high probability, blue indicates low probability. Solid and dashed black profiles are the average velocity structure of the CLSC and northern Valu Fa Ridge from *Jacobs et al.* (2007).

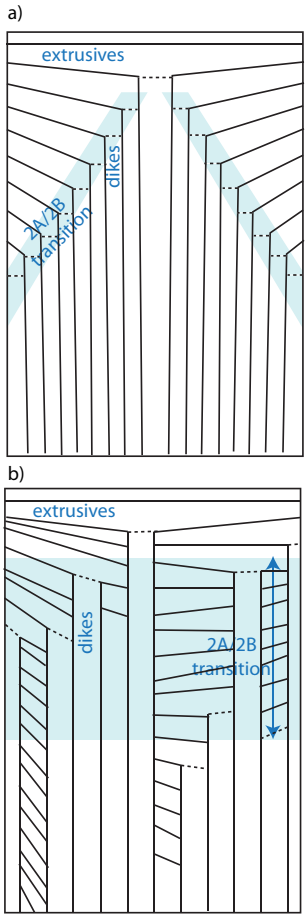

Figure 4.9: Cartoon of two styles of accretionary mechanisms for formation of the upper crust (after *Cann* (1974)). a) Focused diking at the axis splits previously formed dikes causing a sharp 2A/2B transition zone between the extrusives and dikes, which isostatically deepens off-axis as subsequent flows bury previous ones. b) Random emplacement of dikes causes thickening of seismic layer 2A and a relaxation of the gradient across the 2A/2B transition zone. Blue shaded regions represent layer 2A/2B transition zone.

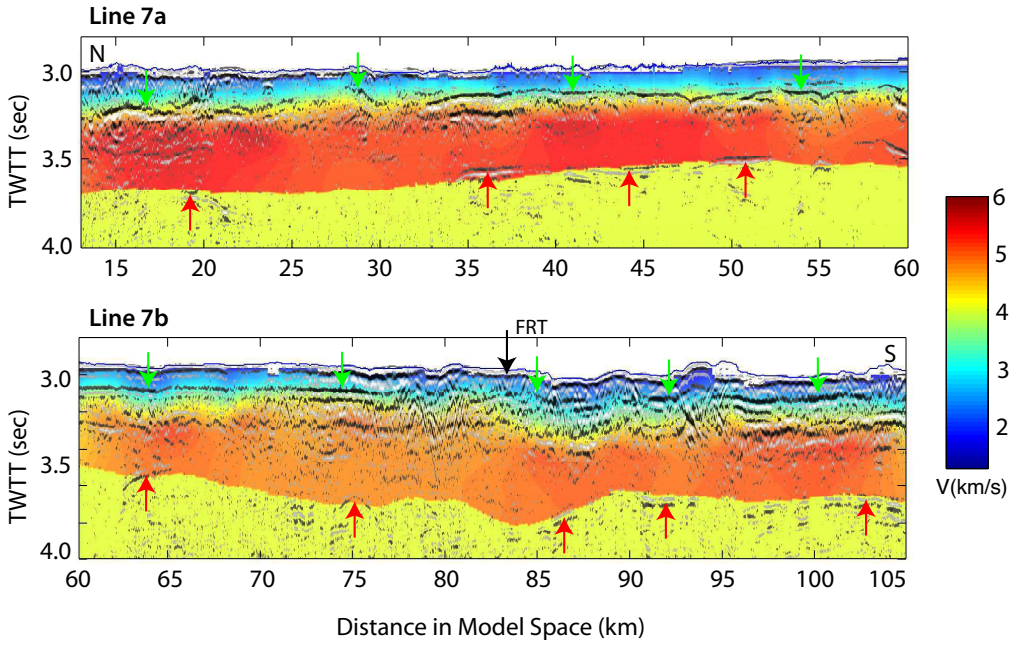

Figure 4.10: Composite images of the zero-offset stacked reflection sections overlain by the tomography for profiles 7a (top) and 7b (bottom) shown in two-way travel time. Red and green arrows are used as guides to follow the AMC and layer 2A reflectors, respectively. FRT Full rate tip of propagator.

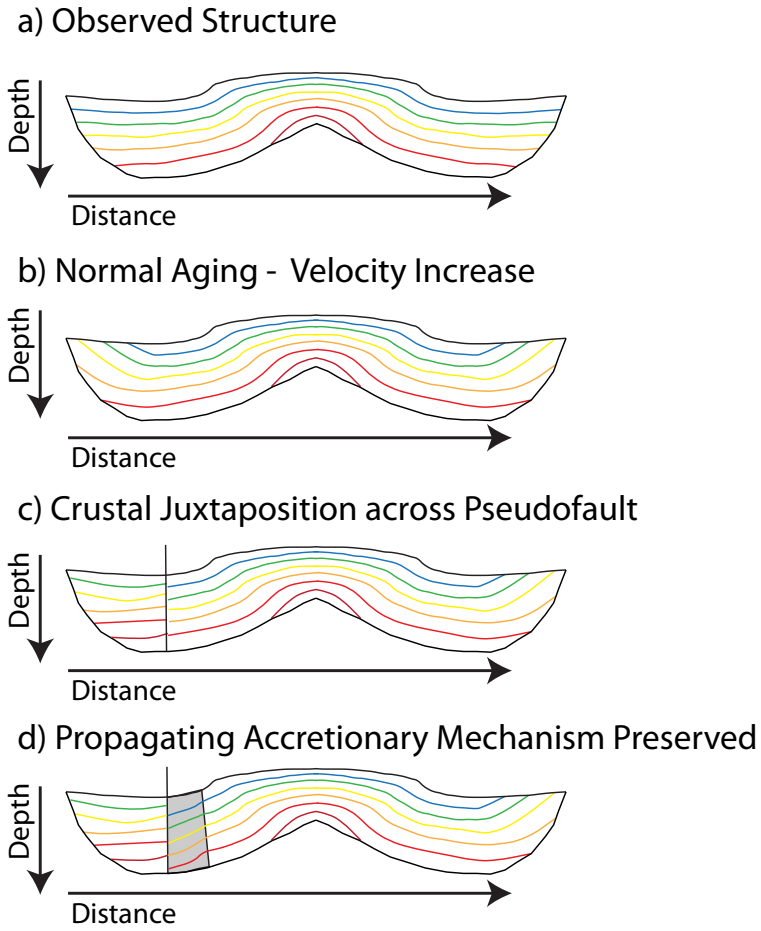

Figure 4.11: Across-axis cartoons illustrating expected crustal velocity structure for various aging and propagator scenarios. Colored lines represent P-wave velocity contours from low (blue) to higher (red) values. Individual sections represent a) actual structure observed, b) an off-axis velocity increase associated with normal aging, c) the juxtaposition of two crusts with different velocity structures across the pseudofaults, and d) a thickened layer 2A and transition zone associated with random, diffuse diking being preserved on the inside of the pseudofaults.